



National Library
of Canada

Bibliothèque nationale
du Canada

Canadian Theses Service

Service des thèses canadiennes

Ottawa, Canada
K1A 0N4

NOTICE

The quality of this microform is heavily dependent upon the quality of the original thesis submitted for microfilming. Every effort has been made to ensure the highest quality of reproduction possible.

If pages are missing, contact the university which granted the degree.

Some pages may have indistinct print especially if the original pages were typed with a poor typewriter ribbon or if the university sent us an inferior photocopy.

Reproduction in full or in part of this microform is governed by the Canadian Copyright Act, R.S.C. 1970, c. C-30, and subsequent amendments.

AVIS

La qualité de cette microforme dépend grandement de la qualité de la thèse soumise au microfilmage. Nous avons tout fait pour assurer une qualité supérieure de reproduction.

S'il manque des pages, veuillez communiquer avec l'université qui a conféré le grade.

La qualité d'impression de certaines pages peut laisser à désirer, surtout si les pages originales ont été dactylographiées à l'aide d'un ruban usé ou si l'université nous a fait parvenir une photocopie de qualité inférieure.

La reproduction, même partielle, de cette microforme est soumise à la Loi canadienne sur le droit d'auteur, SRC 1970, c. C-30, et ses amendements subséquents.

**EXPERIMENTAL AND THEORETICAL STUDIES ON
CONCENTRATED COLUMNAR VORTICES**

Vladimir Kozel

**A Thesis
in
The Department
of
Mechanical Engineering**

**Presented in Partial Fulfilment of the Requirements for
the Degree of Doctor of Philosophy at Concordia
University
Montreal, Quebec, Canada**

September 1991

© Vladimir Kozel, 1991



National Library
of Canada

Bibliothèque nationale
du Canada

Canadian Theses Service Service des thèses canadiennes

Ottawa, Canada
K1A 0N4

The author has granted an irrevocable non-exclusive licence allowing the National Library of Canada to reproduce, loan, distribute or sell copies of his/her thesis by any means and in any form or format, making this thesis available to interested persons.

The author retains ownership of the copyright in his/her thesis. Neither the thesis nor substantial extracts from it may be printed or otherwise reproduced without his/her permission.

L'auteur a accordé une licence irrévocable et non exclusive permettant à la Bibliothèque nationale du Canada de reproduire, prêter, distribuer ou vendre des copies de sa thèse de quelque manière et sous quelque forme que ce soit pour mettre des exemplaires de cette thèse à la disposition des personnes intéressées.

L'auteur conserve la propriété du droit d'auteur qui protège sa thèse. Ni la thèse ni des extraits substantiels de celle-ci ne doivent être imprimés ou autrement reproduits sans son autorisation.

ISBN 0-315-68748-7

Canada

Abstract

Experimental and Theoretical Studies on Concentrated Columnar Vortices

*Vladimir I. Kozel, Ph.D.
Concordia University, 1991*

Experimental and theoretical studies on concentrated columnar vortices are presented. A new model for concentrated vortices is proposed and validated by comparing it with past and present observations. The new approach produces a simple mathematical expression for the liquid free-surface and the pressure thus enabling one to further explore the vortex phenomena. Extensive experimental investigations with the aim to characterize the flowfield in agitator tanks were performed. The main dimensionless groups were established and relationships between the main physical and geometrical parameters were attained. The acquired relationships allowed the prediction of the functional dependence between radius of a core, the vortex strength, with the Reynold's number, and other geometric properties in a cylindrical container with a rotating bottom. The new formula was also implemented in the modelling of the main parameters in vortex chamber flows and the prediction of fine sediment particles concentration and demonstrated the validity and the simplicity of the novel vortex model. The Los Alamos numerical algorithm SOLA-VOF (2-dimensional scheme) was extended to fully 3-dimensional flow field with the presence of an interface and a moving solid boundary in cylindrical coordinates. The numerical results revealed a toroidal flow structure in the radial-axial plane. The obtained simulations for the free-surface profile were

confirmed with those observed. The experimental fact, with respect to the wavy behavior of the core under prevailing conditions, was shown to exist in the approximate solution of the governing equations of motion. This tool will enable one to obtain a solution manifold thus aid in the understanding of early flow transformations towards turbulence.

Acknowledgements

The author expresses a deep appreciation to his supervisor, Professor Georgios H. Vatistas for his guidance and valuable advice throughout the course of the research work.

Sincere thanks go to Professor Sui Lin, for his valuable comments and suggestions. The assistance of Mr. Jian Wang and Mr. Billy Sotirakos during the experimental phase of the investigations is greatly appreciated.

The support provided by the Mechanical Engineering Department at Concordia University as well as the Scholarship by National Science and Engineering Research Council (NSERC) is acknowledged.

The author express his deepest appreciation to his parents, Isaac and Vera Kozel for their advise and moral support.

The present work was partially supported by NSERC Grant No. A6340

Table of Contents

	<i>Page</i>
Table of contents	vi
List of figures	viii
List of tables	x
Nomenclature	xi
<i>Chapter 1. Introduction</i>	1
1.1 A historical survey and previous work	1
1.2 The problem and contributions	6
<i>Chapter 2. Vortex Models</i>	12
2.1 Theoretical analysis	14
2.2 A new model for concentrated vortices	24
<i>Chapter 3. The Experimental Analysis</i>	32
3.1 Experimental apparatus	34
3.2 Dimensional analysis	36
3.3 The core size and the vortex strength	45
3.4 Wave activity in the core	66
<i>Chapter 4. Applications of the New Vortex Model</i>	72
4.1 Vortex chamber	72
4.2 Concentration of a fine sediment particle	80
<i>Chapter 5. Numerical Simulation</i>	84
5.1 Governing equations	86

5.2	Truncated error analysis	93
5.3	Fractional volume function	99
5.4	Boundary conditions	102
5.5	Computational procedure	109
5.6	Numerical results	114
	 <i>Chapter 6. Conclusions</i>	 130
	<i>References</i>	132
	<i>Appendix A</i>	138
	<i>Appendix B</i>	145
	<i>Appendix C</i>	148

List of Figures

<i>Figure</i>	<i>Page</i>
1.1 Vorticity of a typical columnar vortex	8
2.1 The vector properties in cylindrical coordinate system	16
2.2 Comparison of the Rankine's pressure distribution with some experimental results	19
2.3 Velocity and vorticity distributions	27
2.4 Comparison of the tangential velocity distributions	28
2.5 Comparison of the pressure distributions	30
3.1 Schematics of apparatus	35
3.2 Characteristic dimensions	37
3.3 Relationship between two dimensionless groups	40
3.4 The free surface profile - experimental points for a disk and bar as a rotating boundary	41
3.5 A radius of a core is constant as Re varies	47
3.6 The linear dependence between the radii of a core and the cylindrical container	57
3.7 Relationship between the vortex strength and Re	58
3.8 Oscillatory behavior of a vortex core	67
3.9 Variation of equilibrium states ($z = 0, t = 0$)	69
3.10 Comparison of varicose core behavior	71
4.1 Schematics of a vortex chamber	74
4.2 The exit core size as a function of geometric parameter, β	77
4.3 Dimensionless pressure drop v.s. geometric parameter, β	78
4.4 Dimensionless pressure drop v.s. exit core size	78
4.5 Swirl angle as a function of geometric parameter, β and the aspect	

	ratio, R_e/R_0	79
4.6	Concentration of a fine sediment particle	83
5.1	General mesh arrangement	92
5.2	Free-slip boundary conditions	102
5.3	Non-slip boundary conditions	103
5.4	Azimuthal boundary conditions	106
5.5	Pressure interpolation on a free surface interface	112
5.6	Comparison of numerically obtained free surface profile with experimental results	115
5.7	The history of evolution of the secondary flow field	117
5.8	The equilibrium states	128

List of Tables

<i>Table</i>	<i>Page</i>
1.1 Typical dimensions and magnitudes of vortices	7
2.2 Values of β as a function of \bar{r}	22
2.2 Comparison of empirical formulas	31

Nomenclature

A_{in}	inlet area of the vortex chamber
A_t	cross-sectional area of the vortex chamber ($A_t = \pi R_t^2$)
C	sediment concentration
F	fractional volume function
g	gravitational acceleration
H_o	original free surface level
h	free surface level
\vec{q}	total velocity vector
q	magnitude of the total velocity vector
q_{in}	volumetric flowrate of the flow entering the chamber
R_e	radius at the throat of the vortex chamber
r, θ, z	Radial, tangential and axial coordinates respectively
R_d	radius of the disk/bar
R_o	radius of the vortex core
R_t	radius of the cylindrical container and vortex chamber
P	static pressure
P_h, P_∞	static pressure at the vortex center and at $r = \infty$ respectively
t	time
V_r, V_θ, V_z	velocity components in radial, tangential and axial directions respectively
u, v, w	velocity components in radial, tangential and axial directions respectively
\bar{z}	dimensionless free surface level
z_h, z_c, z_∞	elevation of the free surface from a datum at the vortex center, the core and at $r = \infty$ respectively

Greek Symbols

α	upstream-differencing constant
Γ_{∞}	vortex strength
ΔP	pressure change, pressure increment
Δt	time increment
$\Delta x, \Delta y, \Delta z$	radial, axial, azimuthal increments
δ	boundary layer thickness
∇	vector differential operator
ϵ	small scalar parameter, particle diffusion coefficient
μ	dynamic viscosity
λ	arbitrary constant
ρ	density
ν	kinematic viscosity
θ	swirl-angle
Ω	vorticity
ω	angular velocity, over/under-relaxation factor

Subscripts

If otherwise specified the subscripts represent the following:

a	ambient conditions
b	properties at the boundary
F	properties at the adjacent full cell
i, j, k	mesh-point indexes
in	properties at the inlet
out	properties at the outlet

h	properties at the center of the vortex
o	initial conditions
p	properties of the particle
s	properties on the free surface
t	properties at the wall of the cylindrical container
∞	properties far from the vortex center

Superscripts

n, n+1	previous and updated value of the variable
-, ~	dimensionless properties

1. Introduction

1.1 A Historical Survey and Previous Work

When the word vortex is mentioned the vivid pictures of Jupiter and Pluto (from voyager II spacecraft), satellite pictures of a terrestrial hurricane, the bath tub vortex, or the spiral shape of galaxies in the heavens come to mind. Moreover, in fluid dynamics, vortex motion is considered to be one of the most important basic mechanisms which controls the transport of mass, momentum and energy. As a result, the study of vortices received considerable attention throughout the years of technological evolution. Several naturally occurring phenomena such as dust-devils, tornadoes, waterspouts, hurricanes and the processes in many industrial equipment (vortex separators, cyclone combustors and furnaces, vortex tubes, driers etc.) are dominated by concentrated vortices.

The mystery and destructive power associated with the naturally occurring vortices have always fascinated and terrified humans from the dawn of civilization. The legends and fairy tales about naturally induced vortices were the results of superstitious beliefs in unknown supernatural forces at that time. The terror of mariners due to the tidal vortex *Charybdis* is vivid in one of the books of the Odessey. At the same time, the vortex was useful in its practical application; perhaps, the first written indication regarding the use by humans of vortex phenomena comes from Homer who

described with clarity the virtues of swirling motion for cloth cleaning in the river washing-cisterns. In his sixth book of the Odessey, he writes:

" In due course they (princess Nausicaa and her ladies) reached the noble river with its never-failing pools, in which there was enough clear water bubbling up and swirling by to clean the dirtiest clothes. " [Homer, The Odessey, book VI, § 10, 8th century BC., translated by E. V. Rieu, Penguin Book Ltd., 1946, p.104]

The resemblance of today's washing machine principle of operation with the processes taking place in a river's washing-cisterns during, or prior to the Homeric era is indeed worth noting.

In the times of the famous Greek Philosophers, Socrates, Plato, Aristotle and others whose writings had an enormous influence on contemporary western civilization, the mythologic and anthropomorphic explanations of natural laws were replaced with philosophical and mechanically based arguments. The Platonian ideological materialism, however, did not contain the contents of the *vortex theory* to explain the epicyclic motion of celestial bodies and the atomic structure of matter. Perhaps, the strong beliefs in divine (heavenly) creation and in immaterial spirits were still remarkably overwhelming at that time. Although Aristotle, one of Plato's most prominent disciples, is known for his spectacular work on the philosophy of cosmology, a substantial portion of his book on meteorology, *Meteorologica*, is devoted to atmospheric vortices.

Later, during the period of the Renaissance, Leonardo da Vinci described dust-devils and the formation of eddies behind projectiles of various shapes and sudden expansion with clarity. He is, probably, the first one who described and sketched the velocity distribution in a vortex.

René Descartes whose remarkable contribution, his vortex theory of the Universe, was probably the first to replaced the crystalline sphere of ancient astronomy with a combination of fluid vortices. He based his reasoning on the Copernican hypothesis that implicitly rejects the Aristotelian cosmology and that the Universe (including stars, planets and the space which is filled with some form of matter, the *ether*) is swirling around some fixed point generating a vortex which was later recognized as a swirl of Galaxies (Rouse at al (1957)).

The vortex theory to explain the planetary motion, however, has been gradually discarded as this particular branch of science excelled to a more logistic and systematic theory of mechanics devoted mainly by Sir Isaak Newton, in his famous *Principia*. Only in the mid-nineteen century, when scientists were concerned with a microscopic structure of matter and hydrodynamic flow fields under the influence of vortex motion, did the vortex theory gain considerable attention once again. In fact, Helmholtz in 1858 had introduced a new branch of analytical hydrodynamics which in his publication of that year was interpreted as *the theory of vortex motion*. Helmholtz's perfect fluid model of vortex motion (irrotational vortex model) was later adapted by Kelvin to his theory of properties of atoms and molecules. In the same time period, Rankine applies his hypothesis of elasticity of gases and vapors to Molecular Vortices.

Kelvin's analytical model of a vortex structure was the most thorough and probably still is as far as the inviscid flow is concerned. The model demonstrates a profound oscillatory behavior of the vortex core with respect to three spatial components of a principal coordinate system (Kelvin's (1880)). A contradicting argument then appeared as the modelling of a fluid vortex was simulated with an atomic micro-structure - the latter instabilities of the core appeared to be irrelevant to an atomic theory which lead to the conclusion that the vortex motion can only appear in a class of fluid motion. Although the theory was unsuccessful in terms of an atomic structure of matter, his findings concerning vortical fluid dynamics are invaluable. The main flow characteristics of *Kelvin's equilibria* are now used by Vatistas et al (1991) to study flow transition from laminar to turbulent flow conditions.

The complexities associated with concentrated vortices have prevented the development of a universal theoretical vortex model. For this reason, several closed-form solutions concerning specialized cases of the general problem were previously presented. The decay of an initially potential vortex through the action of viscosity has been derived by Oseen (1911) and Hamel (1916). The latter solution is known as the Oseen vortex (it is also called Lamb vortex). A steady flow solution was obtained by Burgers (1948) by balancing the outward momentum diffusion of the decaying ideal vortex using an inward radial convection of the angular momentum, Lught (1983). The time development of Burgers' vortex was derived by Rott (1958). Sullivan's (1959) two-cell vortex model produced axial flow reversal near the axis of rotation whereas Burgers' solution pertains to specific flow situation. The tangential velocity and static pressure distributions agree with the observations and

have been used in the past to study wave phenomena developed in vortex cores, (Prichard (1970), Leibovich (1984), and Vatistas (1990)), flow characteristics in vortex chambers, (Escudier (1980)), and concentrations in combined vortices (Vatistas (1989)).

New information concerning the influence of strong vortices on the main flowfield has also been generated through research regarding industrial applications. In some cases, concentrated columnar vortices are found to be parasitic. Such examples include intakes of liquid pumps (Knauss (1966)), draft tubes of water turbines (Falvey (1971)), draining of reservoirs (Binnie (1948) and Abramson (1966)) and wing tips (Newman B. G. (1959)) are parasitic. In others cases, such as the vortex separator (Ter Linden (1953)), the vortex combustor (Tanasawa and Nakamura (1971)), the vortex tubes (Ranque (1933) and Hilsch (1947)), the nuclear rocket (Kerrebrook (1958) and Ragsdale (1988)), the concentrated vortex is intentionally generated to enhance the effectiveness of the equipment. Relevant knowledge has also been contributed by geophysicists since phenomena such as high Rossby number geophysical vortices (dust-devils, tornadoes, waterspouts, fire whirls), see Morton (1966), belong to the same vortex category. Several monographs have been written on the general subject matter. Important among these are the publications Greenspan (1968), Lewellen(1971), Lught (1983) and Gupta et al (1984).

1.2 The Problem and Contributions

Vortex motion can be generated in a liquid, gas, plasma or in an assembly of solid bodies. Their sizes vary from approximately a few angstroms in quantized vortices of superfluid helium to thousands of km in planetary vortices (for rough dimensions see Table 1.1). Vortices can be categorized as unconfined which are enlarged bodies of fluid and confined which are generated within a bounded domain. Both types can be further classified as columnar or disklike. Vortices whose ratio of core diameter to axis is very small are of the former type while those of considerably large ratio are of the latter. Concentrated columnar vortices can be interpreted as another sub-category and are characterized by local vorticity extrema, fig. 1.1. Their vorticity is concentrated in a small tubular region near the center, decaying rapidly outward in the radial direction. In the past, analysis of concentrated, mechanically produced or high Rossby number naturally occurring vortices relied mainly on the utilization of semi-empirical models, one due to Rankine and the other due to Burgers.

Rankine's model combines a solid body rotation of the fluid inside the core surrounded by an irrotational vortex. In the rotational region the fluid is assumed to possess a constant vorticity while outside the core it is zero. Extensive descriptions of the fundamental properties of Kelvin's model can be found in many texts (Lamb (1945), Batchelor (1967), Robertson(1965)). Although Rankine's combined vortex is close to the real fluid motion it admits a sharp velocity transition at the core, which is not physically possible.

Table 1.1 Typical Dimensions and Magnitudes of Vortices.

Vortex motion and shapes	Diameter (based on vortex core)	Velocity	Rossby No.	Disklike or Columnar
Quantized vortices (superfluid helium)	10^{-8} cm	–	–	columnar
Bathtub vortex	1 cm	0.1 m/sec	10^5	both
Vortex chambers	2 cm	30 m/sec	10^7	both*
Dust devils	3 m	10 m/sec	$3 (10^4)$	columnar
Tornadoes	50 m	150 m/sec	$3 (10^4)$	columnar
Hurricanes	500 km	50 m/sec	1	disklike
Ocean circulation	3000 km	1.5 m/sec	$5 (10^{-3})$	disklike

* Depends on the aspect ratio (diameter/length) and contraction ratio of the chamber (core diameter/exit diameter), see Lught (1983)

The action of viscosity at the junction of the two velocity distributions is expected to smooth out the velocity's sharp apex. As a result the values of the azimuthal velocity component near the point of transition are lower than those predicted by the simulation. In order to account for the latter discrepancy modified versions of Rankine's model have also been used to interpret the observations, see for example Reydon and Gauvin (1981). These assume quasi-forced and quasi-free vortices inside and outside the core respectively.

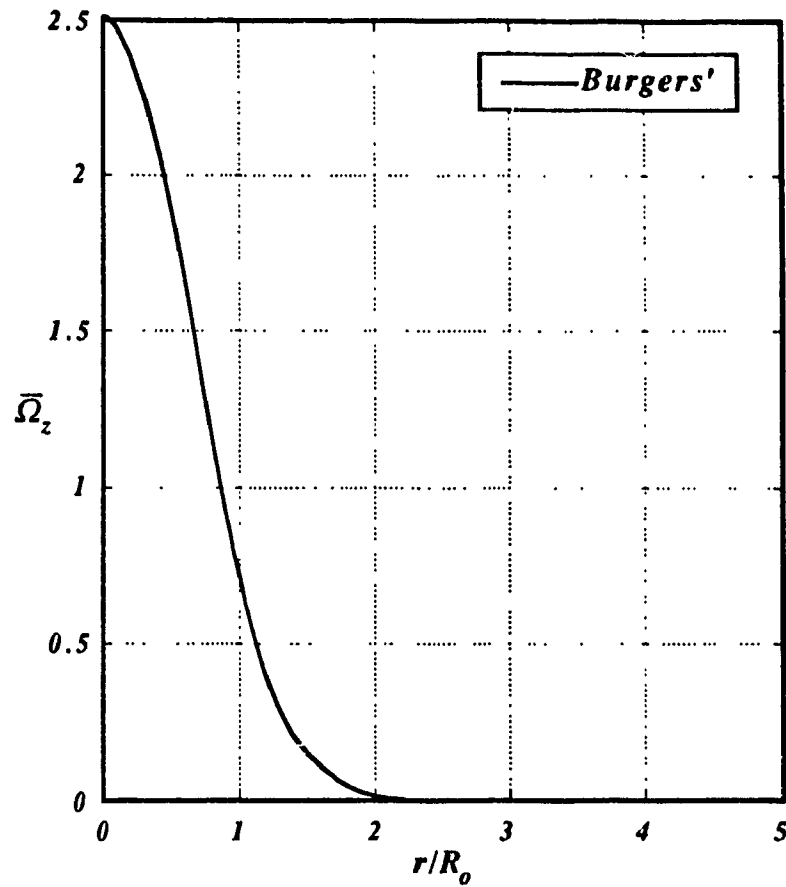


Fig. 1.1 Vorticity of a typical concentrated vortex.

Burgers' model was the most popular of the two since it was more realistic, and provided a swirl velocity distribution with continuous derivatives. However, the integration of centrifugal acceleration to obtain the pressure distribution resulted in exponential integrals which made any further theoretical treatment practically impossible. Bennett (1988) presented an alternate formula for the azimuthal velocity component which although simpler than the previous formulations, refuted the basic requirement that the maximum velocity must occur at a dimensionless radius equal to one. Here, a new, simpler and non-contradictory vortex model is proposed. The

simplicity of the novel formula for the tangential velocity component allows one to derive a closed form solution for the static pressure which fits well the observed values. The vortex models of Rankine and Basina et al (1974) are found to be the asymptotic conditions of the present azimuthal velocity distributions. Based on the equations of motion the empirical model produces radial and axial velocity components which are bounded over an infinite domain. Furthermore, it now gives the opportunity to further analyze phenomena which was practically impossible via the Burgers' model.

The novel approach is utilized to study the main characteristics of concentrated, columnar, liquid vortices produced in a cylindrical, partially filled container using rotating disks and bars as agitators placed at the bottom. There are two reasons as to why such an arrangement was selected. First, such systems are routinely used in laboratories and industries to mix different fluids. Second, turntables have been used extensively to study the fundamental aspects of vortices. Previous work by Vatistas (1989) has shown that the azimuthal velocity component and pressure may also be applicable to a variety of concentrated vortices (i.e. vortex chambers, wing tips vortices, etc.). The difference due to geometry and flow conditions in numerous situations are manifested in the ancillary flow taking place in the radial-azimuthal plane. In the study of every concentrated vortex flow, the core size is one of the unknowns which is either obtained experimentally and/or based on an auxiliary principle. In vortex chambers, the core size was found by Vatistas et al (1986) to be adequately described by an equation obtained using the minimum pressure drop principle. The analysis given earlier by Vatistas (1989) concerning the flow in a stirred cylindrical tank assumed a known core radius. Since a theoretical determination of the core radius for a present

configuration is very difficult, dimensional analysis and extensive experimentation was used to derive such a relationship. The results are used to determine solid particle concentrations in an aqueous concentrated vortex.

A numerical algorithm, previously developed by the Los Alamos research laboratory has been extended to solve the fully 3-dimensional time dependent Navier-Stokes equations for liquids with an interface and a moving boundary. A new method for the application of the boundary conditions at the center-line is presented. The non-conservative form of the governing equations has been found to enhance the numerical stability of the method. The reason for such a behaviour is given. The algorithm has been applied to examine the agitator problem. The numerical investigations produced free-surface profiles that agree with the experimental observations. The computed secondary toroidal vortex structures, taking place in the radial-azimuthal plane and the vortex core wandering the transient spin-up process correspond to the experimental visualizations.

In 1880, Lord Kelvin, in an attempt to explain the quantization of atomic orbits using a vortex (presumably as a fluid mechanics analog), found that several stationary solutions to the problem were consistent with the inviscid equations of motion. In his study, Kelvin assumed that the main flow is perturbed by harmonic disturbances which produce varicose undulations in the vortex core manifold. Until recently, these stable fluid states were known in theoretical fluid mechanics as Kelvin's vortex equilibria. In 1990, Vatistas produced the stationary states under laboratory conditions. The present numerical study clearly shows that different wave number core patterns

which were conjectured by Kelvin and produced by Vattistas (1990) are present in the solutions of the Navier-Stokes equations.

2. Vortex Models

Concentrated vortices influence dramatically the performance of numerous practical devices. Gas-core nuclear rockets, swirl combustion chambers, vortex valves and cyclone separators are typical examples which, from a fluid dynamics point of view, run under the category of confined vortical devices. For design purposes, knowledge of the main parameter behavior is essential. The complexity of the phenomena involved, unfortunately, does not permit a complete analytical flow characterization. The governing equations of motion are comprised from non-linear terms which make an analytical solution not possible, excluding the fact that curvilinear or even recti-linear boundaries may impose even greater difficulties. Since a general treatment of such a complex problem present enormous mathematical difficulties, simplified models, able of describing the main characteristics, have been used in the past.

Consideration is given here to the main effects of vortex flows that are characterized by a dominant centrifugal force-field taking place in the radial-azimuthal plane. The static pressure evolves in such a way as to primarily balance the centrifugal forces ignoring almost completely the other velocity components. The main properties represented by the radial distributions of the azimuthal velocity and the static pressure were found by Vatistas (1989) to be common to most vortical flows of this type and not to depend on the method of their production.

Rankine's combined vortex was commonly used in the past. One of the major disadvantages of employing Rankine's model is the overestimation of the tangential component of velocity in the vicinity of a vortex core. This gave rise to a better model which was introduced by Burgers (1948). Burgers' model provides an estimation of tangential velocity distribution which agrees well with experimental results. However, there are a number of disadvantages which accompany the model. Primarily, it is the radial pressure distribution that requires the use either tables of integration or the application of numerical methods. Furthermore, the radial velocity is not bounded over the infinite domain.

A new empirical formula for the tangential velocity which agrees well with the experimental results is presented here. From the equations of motion, the other velocity components can be derived. The novel approach provides a closed form solution for the static pressure, while the velocities are bounded over the infinite domain.

2.1 Theoretical Analysis

Under the assumption of steady, laminar, incompressible and axisymmetric flow, the governing equations of the vortex flow are represented by:

continuity

$$\frac{1}{\bar{r}} \frac{\partial}{\partial \bar{r}} (\bar{r} \bar{V}_r) + \frac{\partial \bar{V}_z}{\partial \bar{z}} = 0 \quad (2.1)$$

r - momentum

$$S_n \left(\bar{V}_r \frac{\partial \bar{V}_r}{\partial \bar{r}} + \bar{V}_z \frac{\partial \bar{V}_r}{\partial \bar{z}} \right) - \frac{V_\theta^2}{\bar{r}} = - \frac{\partial \bar{P}}{\partial \bar{r}} + S_n \left(\nabla^2 \bar{V}_r - \frac{\bar{V}_r}{\bar{r}^2} \right) \quad (2.2.a)$$

z - momentum

$$S_n \left(\bar{V}_r \frac{\partial \bar{V}_z}{\partial \bar{r}} + \bar{V}_z \frac{\partial \bar{V}_z}{\partial \bar{z}} \right) = - \frac{\partial \bar{P}}{\partial \bar{z}} - \eta + S_n \nabla^2 \bar{V}_z \quad (2.2.b)$$

θ - momentum

$$\frac{\bar{V}_r}{\bar{r}} \frac{\partial}{\partial \bar{r}} (\bar{r} \bar{V}_\theta) + \bar{V}_z \frac{\partial \bar{V}_\theta}{\partial \bar{z}} = \nabla^2 \bar{V}_\theta - \frac{\bar{V}_\theta}{\bar{r}^2} \quad (2.2.c)$$

where,

$$\nabla^2 = \frac{\partial^2}{\partial \bar{r}^2} + \frac{1}{\bar{r}} \frac{\partial}{\partial \bar{r}} + \frac{\partial^2}{\partial \bar{z}^2}$$

$$\bar{r} = r/R_o$$

$$\bar{z} = z/R_o$$

$$\bar{V}_r = \frac{V_r R_o}{v}$$

$$\bar{V}_z = \frac{V_z R_o}{v}$$

$$\bar{V}_\theta = \frac{2\pi V_\theta R_o}{\Gamma_\infty}$$

$$\bar{P} = \left(\frac{2\pi R_o}{\Gamma_\infty} \right)^2 \frac{P - P_h}{\rho}$$

$$S_n = \left(\frac{2\pi V}{\Gamma_\infty} \right)^2$$

$$\eta = g \left(\frac{2\pi R_o}{\Gamma_\infty} \right)^2 R_o$$

Under the assumption that S_n is considerably small and that the axial dependance of the tangential velocity can be neglected the above equations are simplified to:

continuity

$$\frac{1}{\bar{r}} \frac{\partial}{\partial \bar{r}} (\bar{r} \bar{V}_r) + \frac{\partial \bar{V}_z}{\partial \bar{z}} = 0 \quad (2.1)$$

r - momentum

$$\frac{V_\theta^2}{\bar{r}} = \frac{\partial \bar{P}}{\partial \bar{r}} \quad (2.2.a)$$

z - momentum

$$\frac{\partial \bar{P}}{\partial \bar{z}} = -\eta \quad (2.2.b)$$

θ - momentum

$$\frac{\bar{V}_r}{\bar{r}} \frac{d}{d\bar{r}} (\bar{r} \bar{V}_\theta) = \frac{d}{d\bar{r}} \left(\frac{1}{\bar{r}} \frac{d}{d\bar{r}} (\bar{r} \bar{V}_\theta) \right) \quad (2.2.c)$$

The vorticity, known as a vector quantity and the parameter that represents the transverse gradients of the velocity vector is introduced here. The vorticity, $\vec{\Omega}$ may also be expressed as a function of angular velocity of a fluid element, ω . The three orthogonal components of the vorticity vector are:

$$\bar{\Omega}_z = \frac{1}{r} \frac{\partial}{\partial r} (r \bar{V}_\theta)$$

$$\bar{\Omega}_r = \bar{\Omega}_\theta = 0$$

where,

$$\bar{\Omega}_z = \frac{2\pi R_o^2}{r_\infty} \Omega_z$$

The reason of introducing the latter parameter is to quantify the degree of vortex concentration. The geometric representation of the three velocity and vorticity components are given in fig. 2.1:

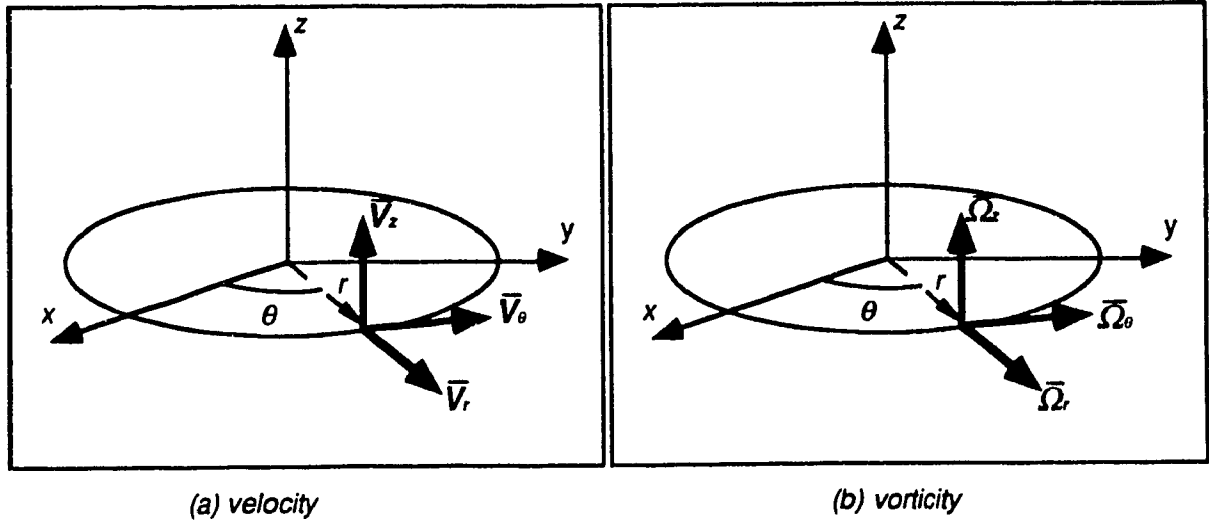


Fig. 2.1 The vector properties in cylindrical coordinate system.

Rankine's model

Rankine's combined vortex was one of the first steps to model concentrated vortices. It combines two distinct modes of rotation; the solid body rotation (or forced vortex) taking place inside the core and the potential flow (or free vortex) existing outside. It is not clear from the literature as to how it was established. The realization that a linear and a hyperbolic variation of the tangential velocity are solutions to eq. (2.2.c) (with the convective terms neglected), combined with past observations might have been the origin of conception. Nevertheless, whatever the reason of its origin, the azimuthal velocity profile for a Rankine's vortex is given by,

$$\bar{V}_\theta = \bar{r} \quad \text{for} \quad 0 \leq \bar{r} \leq 1 \quad (2.3.a)$$

$$\bar{V}_\theta = \frac{1}{\bar{r}} \quad \text{for} \quad 1 \leq \bar{r} \leq \infty \quad (2.3.b)$$

Inside the core, according to azimuthal momentum equation (eq. (2.2.c)), it is required that

$$\bar{V}_r = 0$$

Accordingly, from continuity

$$\bar{V}_z = \text{constant}$$

In the region outside the core, the θ -momentum equation is satisfied automatically, regardless of the radial velocity distribution. Hence, the latter velocity component may be represented by any arbitrary function

$$\bar{V}_r = f_n(\bar{r})$$

provided $\bar{V}_{r(\bar{r}=1)} = 0$. From continuity,

$$\bar{V}_z = -\bar{z} \frac{1}{\bar{r}} \frac{\partial}{\partial \bar{r}} (\bar{r} f_n(\bar{r})) \quad (2.4)$$

The pressure is a function of \bar{r} and \bar{z} . The change of pressure is given by

$$d\bar{P}(\bar{r}, \bar{z}) = \frac{\partial \bar{P}}{\partial \bar{r}} d\bar{r} + \frac{\partial \bar{P}}{\partial \bar{z}} d\bar{z} \quad (2.5)$$

since

$$\frac{\partial M}{\partial \bar{r}} = \frac{\partial N}{\partial \bar{z}} = 0 \quad (2.6)$$

where,

$$M = \frac{\bar{V}_\theta^2}{\bar{r}} \quad \text{and} \quad N = -\eta$$

The pressure must therefore, be an exact differential. Then the determination of static pressure distribution requires the integration of the above equation

$$\bar{P}(\bar{r}, \bar{z}) = -\eta \bar{z} + \int \frac{\bar{V}_\theta^2}{\bar{r}} d\bar{r} + \text{Const.} \quad (2.7)$$

The static pressure distribution for gaseous vortex ($\eta \equiv 0$) and the liquid free-surface profile $\bar{P}(\bar{r}) = 0$ are given by the same equations:

$$\bar{\Delta P} = \frac{\bar{r}^2}{2} \quad \text{for} \quad 0 \leq \bar{r} \leq 1 \quad (2.8.a)$$

$$\bar{\Delta P} = 1 - \frac{1}{2\bar{r}^2} \quad \text{for} \quad 1 \leq \bar{r} \leq \infty \quad (2.8.b)$$

(For detailed derivation of eq's (2.8) refer to *appendix A.*)

Rankine's combined vortex is an empirical model. Yet, it is well suited for preliminary analysis. Although there is great deal of overestimation of the combined tangential velocity in the vicinity of a core radius, the pressure distribution matches reasonably well the experimental results, see fig. 2.2.

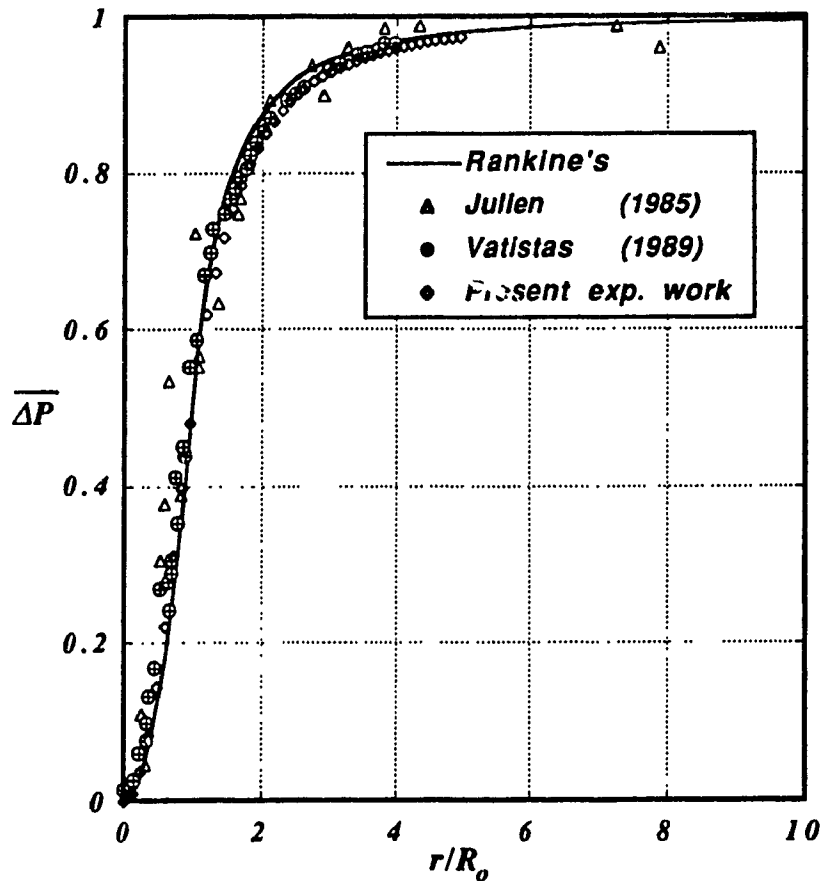


Fig. 2.2. Comparison of the Rankine's pressure distribution with the experiment.

Burgers' model

Rankine's model is a rough approximation of the actual vortex mechanism; its tangential velocity distribution is assumed to change from a force vortex inside the core to an irrotational vortex outside with a discontinuity of the vorticity at the point of transition. This led many to seek a better model.

Burgers (1948) arrived to a vortex model which provides a tangential velocity with continuous derivatives. He assumed a linear distribution of radial velocity which, mathematically, possesses the form:

$$\bar{V}_r = -\lambda \bar{r} \quad (2.9)$$

where λ is a constant. Substituting eq. (2.9) into θ -momentum equation (eq. (2.2.c)) and integrating it twice, leads to:

$$\bar{V}_\theta = -\frac{B_1}{\alpha \bar{r}} e^{-\alpha \bar{r}^2} + \frac{B_2}{\bar{r}} \quad (2.10)$$

where, B_1 and B_2 are integration constants and $\alpha = \lambda/2$. To obtain uniqueness of the above solution, the boundary conditions must be applied; the tangential velocity is equal to zero at the axis of rotation which leads to,

$$B_2 = \frac{B_1}{2\alpha}$$

also, by setting the following condition,

$$\lim_{\bar{r} \rightarrow \infty} \bar{r} \bar{V}_\theta = 1 \quad (2.11)$$

$$B_2 = 1$$

and

$$B_1 = \alpha$$

Hence,

$$\bar{V}_\theta = \frac{2\pi R_0}{\Gamma_\infty} V_\theta = \frac{1}{\bar{r}} (1 - e^{-\alpha \bar{r}^2}) \quad (2.12)$$

From the dimensional radial velocity distribution,

$$V_r = -A r,$$

$A = 2\alpha v/R_0^2$. α is evaluated employing the maximum velocity condition at the core radius. Since the slope at the maxima is zero, eq. (2.12) is to be differentiated with respect to r then equated to zero. The latter allows one to evaluate α from the resulting non-linear algebraic equation:

$$(1 + \alpha) e^{-\alpha} - 1 = 0 \quad (2.13)$$

There are two roots in the interval $[0, \infty)$, one when $\alpha = 0$ and the other when $\alpha = 1.256$. For $\alpha = 0$ the trivial distribution, $\bar{V}_\theta = 0$ is obtained, hence it is excluded.

Correspondingly, the radial and axial velocity components are

$$\bar{V}_r = \frac{V_r R_0}{v} = -2\alpha r \quad (2.14)$$

$$\frac{\bar{V}_z}{\bar{z}} = \frac{V_z R_0}{zv} = 4\alpha \quad (2.15)$$

One major drawback associated with Burgers' model is the approximation of pressure distribution which retains a non-closed form of a solution. The pressure distribution is given by

$$\bar{P}(\bar{r}, \bar{z}) = -\eta \bar{z} + \beta \quad (2.16)$$

where,

$$\beta = \int_r^{\infty} \frac{1}{\bar{r}^3} (1 - e^{-\alpha \bar{r}^2})^2 d\bar{r}$$

Performing the integration yields,

$$\beta = \frac{1}{2\bar{r}^2} (1 - e^{-\alpha \bar{r}^2})^2 + \alpha [Ei(-\alpha \bar{r}^2) - Ei(-2\alpha \bar{r}^2)] \quad (2.17)$$

where

$$Ei(-u) = \int_r^{\infty} \frac{e^{-u}}{u} du$$

Some values of β are tabulated in a table 2.1.

Table 2.1 Values of β as a function of \bar{r}

\bar{r}	β	\bar{r}	β	\bar{r}	β
0.0	0.87059	0.9	0.46073	4.0	0.03125
0.1	0.86281	1.0	0.40713	5.0	0.02000
0.2	0.83983	1.2	0.31545	6.0	0.01389
0.3	0.80344	1.4	0.24477	7.0	0.01020
0.4	0.75614	1.6	0.19215	8.0	0.00781
0.5	0.70062	1.8	0.15341	9.0	0.00617
0.6	0.64100	2.0	0.12475	10.0	0.00500
0.7	0.57936	2.5	0.08000	50.0	0.00020
0.8	0.51860	3.0	0.05555	100.0	0.00005

The pressure distribution and the free surface profile can be then calculated using,

$$\overline{\Delta P} = \frac{z - z_h}{z_\infty - z_h} = \frac{P - P_h}{P_\infty - P_h} = 1 - \frac{\beta}{\alpha \ln 2} \quad (2.18)$$

(for detailed derivation of eq. (2.18) refer to the *appendix A*).

Burgers' model is an attempt to arrive at a simple formulation which provides a more realistic picture of the vortex phenomena when the secondary effects are neglected. The model provides a single equation for the tangential velocity which confirms the observed values. Although the determination of the azimuthal distribution of the velocity does not involve significant complications, the distribution of pressure requires the use of either tables of integration or the application of a numerical method to evaluate the integrals involved.

2.2 A New Model for Concentrated Vortices

Burgers' velocity distribution solved the problems encountered with Rankine's model but has created a mathematical contradiction as well as a difficulty associated with the evaluation of static pressure. The contradiction emanates from the first boundary condition which requires sustaining the condition,

$$\lim_{\bar{r} \rightarrow \infty} \bar{r} \bar{V}_\theta = 1$$

whereas the radial velocity is not bounded in an infinite domain (in the r -direction). The difficulty arises when the pressure distribution is to be obtained or if the calculate the total liquid volume (see chapter 3) is required. Employing Burgers' model, one must integrate the pressure distribution (involving the integrals of an exponential integrals) which is indeed a formidable task.

Recently Bennet (1988) presented the following empirical tangential velocity distribution:

$$\bar{V}_\theta = \frac{2\bar{r}}{1 + 2\bar{r}^2}$$

Although the above equation gives an explicit static pressure distribution, the tangential velocity possesses a maximum for \bar{r} equal to approximately 0.707. This refutes the basic requirement which demands the maximum to occur at $\bar{r} = 1.0$.

Based on previous observations as well as the experimental pressure (free-surface) distributions to be discussed in the next chapter and several

trials with a number of shape functions, we are proposing the following general form of the tangential velocity:

$$\bar{V}_\theta = \frac{\bar{r}}{(1 + \bar{r}^{2n})^{1/n}} \quad (2.19)$$

where a and n are empirical constants. Since the above equation must possess a maximum at $\bar{r} = 1$, a must be equal to 2 or,

$$\bar{V}_\theta = \frac{\bar{r}}{(1 + \bar{r}^{2n})^{1/n}} \quad (2.20)$$

Analogous to Burgers' profile, eq. (2.20) satisfies the conditions:

- (i) at $\bar{r} = 0$, $\bar{V}_\theta = 0$
- (ii) at $\bar{r} \rightarrow \infty$, $\bar{V}_\theta \bar{r} = 1$

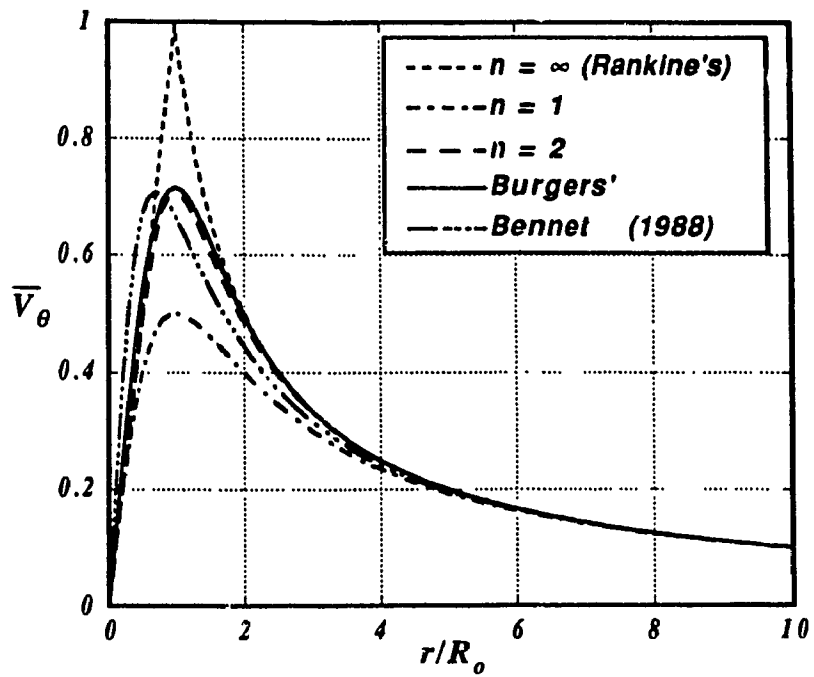
The radial velocity component can be obtained employing the θ -momentum equation, eq. (2.2.c),

$$\bar{V}_r = \frac{2(1 + n)\bar{r}^{2n-1}}{1 + \bar{r}^{2n}} \quad (2.21)$$

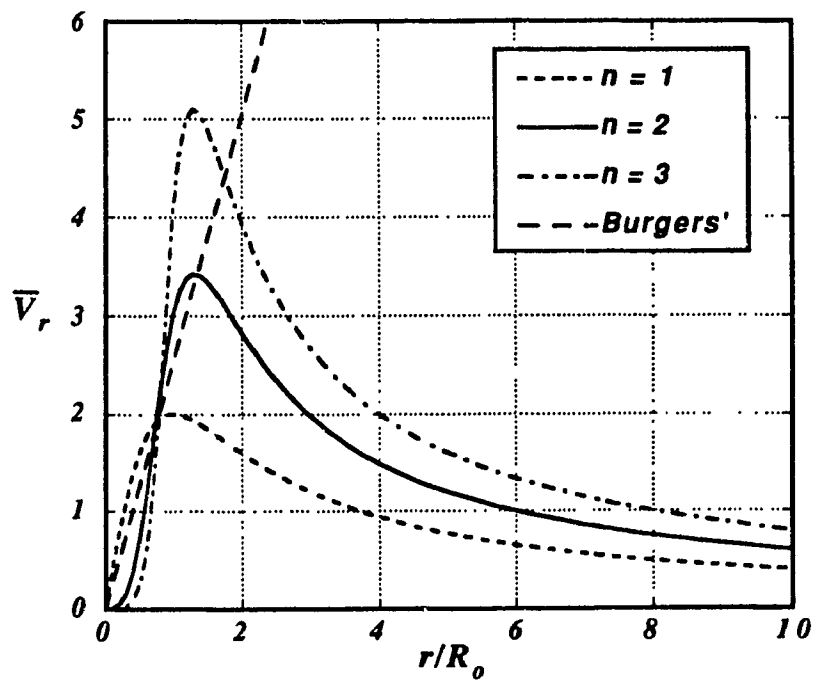
From continuity and eq. (2.21) the following equation for the axial velocity components obtained:

$$\frac{\bar{V}_z}{\bar{z}} = \frac{4n(1 + n)\bar{r}^{2(n-1)}}{(1 + \bar{r}^{2n})^2} \quad (2.22)$$

For $n = 1$ the tangential velocity distribution is the same as the empirical equation attained by Basina et al (1974), fig. 2.3.a. Rankine's distribution is approached as n goes to infinity. Both eq. (2.21) and eq. (2.22) have singularities at the vortex center for $n < 1$; hence, distributions with n less

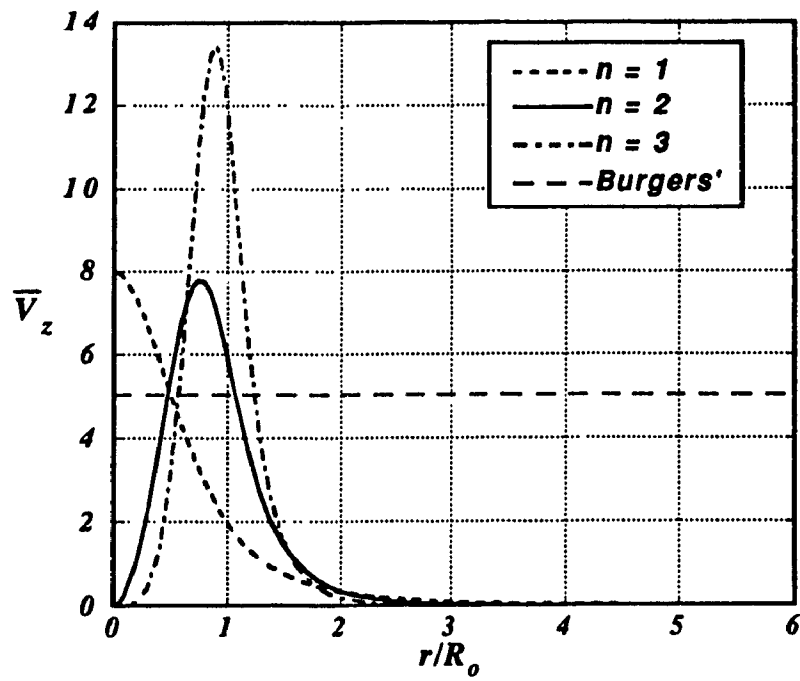


(a) tangential

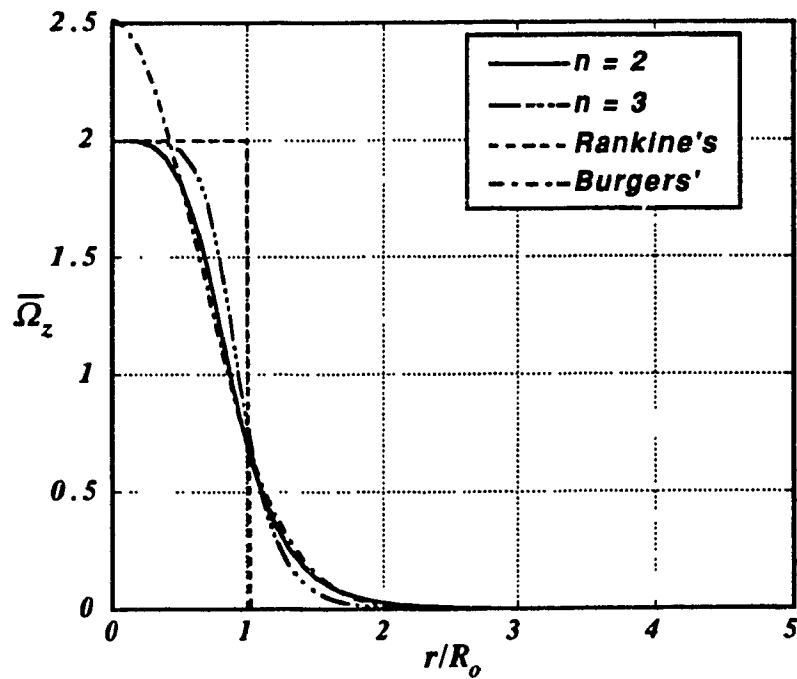


(b) radial

Fig. 2.3.a & b. Velocity and vorticity distributions.



(c) axial



(d) vorticity

Fig. 2.3.c & d. Velocity and vorticity distributions.

than one should not be permitted. The general shape of the radial velocity given by eq. (2.21), see fig. 2.3.b, is also qualitatively closer to the observations of Ross (1964). For any other finite value of n , the values of all velocity components are well behaved. In addition, these values are bounded over the entire domain.

The best fit of eq. (2.20) to the actual tangential velocity component, for n as an integer, is obtained if $n = 2$. Then the tangential velocity is given by,

$$\bar{V}_\theta = \frac{\bar{r}}{\sqrt{(1 + \bar{r}^4)}} \quad (2.23)$$

Comparisons of eq. (3.23) with several experiments are given in fig. 2.4.

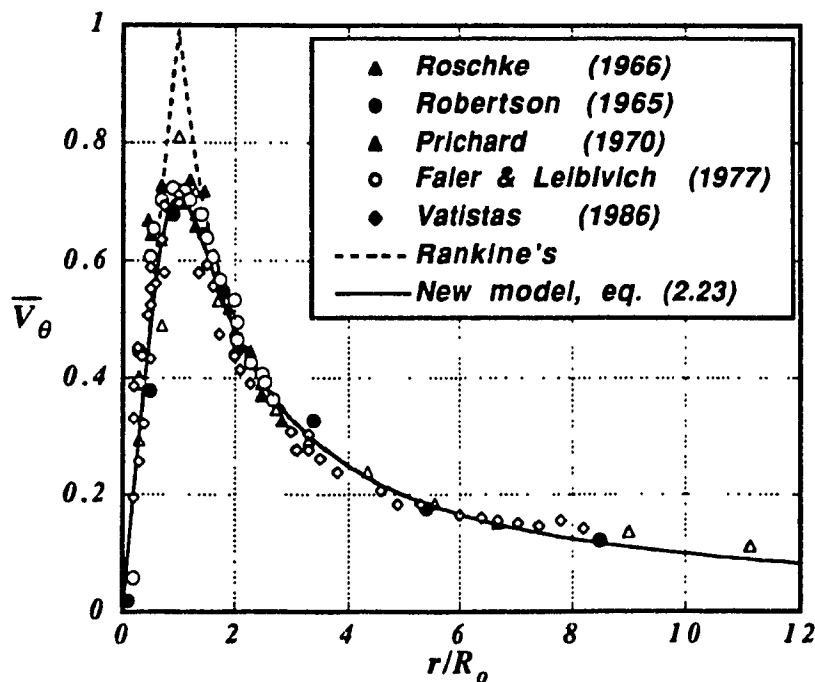


Fig. 2.4. Comparison of the tangential velocity distributions.

One of the advantages of employing the new empirical formula is to obtain a simple closed form solution for static pressure distribution. Thus, the free surface profile and the static pressure distribution can be determined using:

$$\overline{\Delta P} = \frac{z - z_h}{z_\infty - z_h} = \frac{P - P_h}{P_\infty - P_h} = \frac{2}{\pi} \arctan(\bar{r}^2) \quad (2.24)$$

(for detailed derivation of eq. (2.24) refer to *appendix A*). Equation (2.24) agrees well with experimental results taken from several sources, see fig. 2.5, and with the results of the present investigations concerning the free-surface profiles of a vortex in an agitator tank given in fig. 3.4.

A simple vortex model based on an empirical formula of the tangential velocity component was presented. A closed form solution for the static pressure which fits well the observed values was obtained. The model produced radial and axial velocity components which are bounded over the entire domain. Despite the fact that the new model is generally suited for unconfined vortex, it may also be employed to a confined vortex as long as the side-wall boundary effects are minimal. It will be feasible, for instance, when the ratio of the core radius to a confinement characteristic length is considerably less than one.

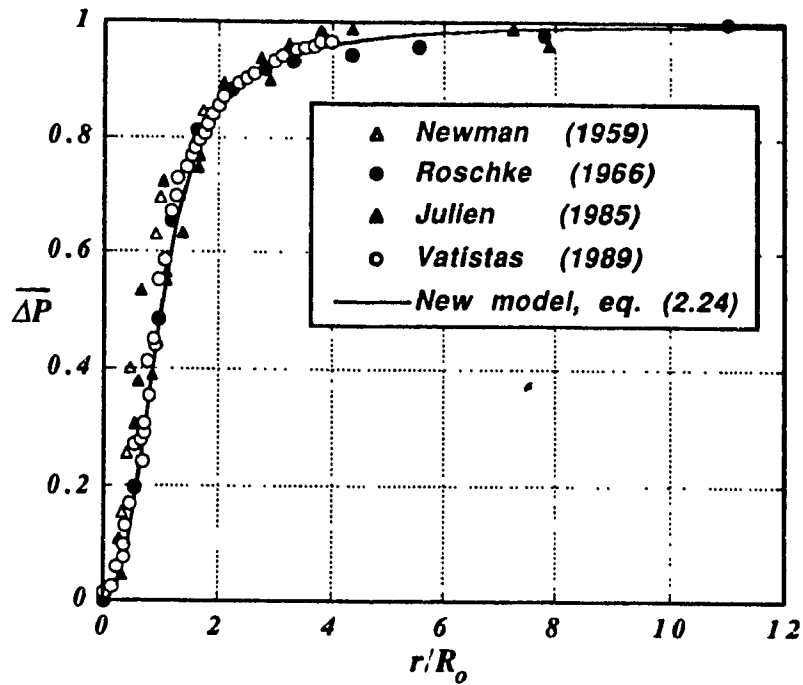


Fig. 2.5. Comparison of the pressure distributions.

A summary of the main flow parameters obtained using various vortex models are illustrated in a table. 2.2.

At first glance one might indeed be surprised to note the strong dependance of the flow taking place in the radial-axial plane to the main flow in the radial-azimuthal plane. It is, however, a well known fact that for concentrated vortices, the flow development in the latter plane is almost indifferent to that taking place in the former plane. One can find in the technical literature a variety of flow situations where the tangential and static pressure distributions exhibit a Rankine-like behavior despite the fact that the secondary flows in the radial-axial plane are substantially different. The experimental work of Escudier et al (1980 and 1982) has shown clearly that the vortex core structure depends on two non-dimensional numbers; the Reynolds and the swirl numbers. For a fixed Reynolds number, increasing

swirl, the development of the axial velocity component in the core changes from a jet-like to a wake-like structure. This process is accompanied by an undetected tangential velocity component shape modification. The experiments of Escudier and his associates were performed on a vortex chamber with an inlet slit covering the entire length of the chamber. If a series of inlet jets were arranged near the bottom plate, around the periphery of the chamber (Vatistas (1984)), then the axial velocity would develop in a completely different manner. Nevertheless, in both cases the tangential velocity component respects the non-dimensional form of Burgers' or the new equation, eq. (2.23).

Table 2.2 Comparison of empirical formulas.

	$\bar{V}_\theta = \frac{2\pi R_0}{\Gamma_\infty} v_\theta$	$\bar{V}_r = \frac{V_r R_0}{v}$	$\frac{\bar{V}_z}{\bar{z}} = \frac{V_z R_0^2}{z v}$	$\bar{P} = \left(\frac{2\pi R_0}{\Gamma_\infty} \right)^2 \frac{P - P_h}{\rho}$	$\bar{\Omega}_z = \frac{2\pi R_0^2}{\Gamma_\infty} \Omega_z$
Rankine's	$0 \leq \bar{r} \leq 1 \quad \bar{r}$	0	const.	$\frac{\bar{r}^2}{2}$	2
	$1 \leq \bar{r} \leq \infty \quad \frac{1}{\bar{r}}$	$f_n = (\bar{r})$	$-\frac{1}{\bar{r}} \frac{\partial}{\partial \bar{r}} (\bar{r} f_n(\bar{r}))$	$1 - \frac{1}{2\bar{r}^2}$	0
Burgers'	$\frac{1}{\bar{r}} (1 - e^{-\alpha \bar{r}^2})$	$-2\alpha \bar{r}$	4α	$1 - \frac{\beta}{\alpha \ln 2}$	$2\alpha e^{-\alpha \bar{r}^2}$
Present work	$\frac{\bar{r}}{\sqrt{1 + \bar{r}^4}}$	$-\frac{6\bar{r}^3}{1 + \bar{r}^4}$	$\frac{24\bar{r}^2}{(1 + \bar{r}^4)^2}$	$\frac{2}{\pi} \tan^{-1} \bar{r}^2$	$\frac{2}{\sqrt{(1 + \bar{r}^2)^3}}$

3. The Experimental Analysis

The objectives of conducting the present experimental work is first to predicate the validity of eq. (2.24) in correlating the shape of the interface. Secondly, to establish appropriate relationships between the core radius and the vortex strenght as a function of the geometrical and physical parameters involved with the agitator problem. Dimensional analysis is applied to reduce the experimental effort and to present the results in terms of the main dimensionless groups.

In the previous chapter all the models assumed a known core which must be provided as part of the boundary conditions. In vortex chambers, the core size was found by Vatistas et al (1986) to be adequately described by an equation obtained using the minimum pressure drop principle. For the rotating agitator problem, there is no available methodology with firm theoretical foundations that will enable one to determine the core radius. However, the behavior of the core as a function of the remaining variables is very important since all the main flow parameters depend directly on it. For this reason extensive experimentation was used here to disclose the unique proprieties of the core.

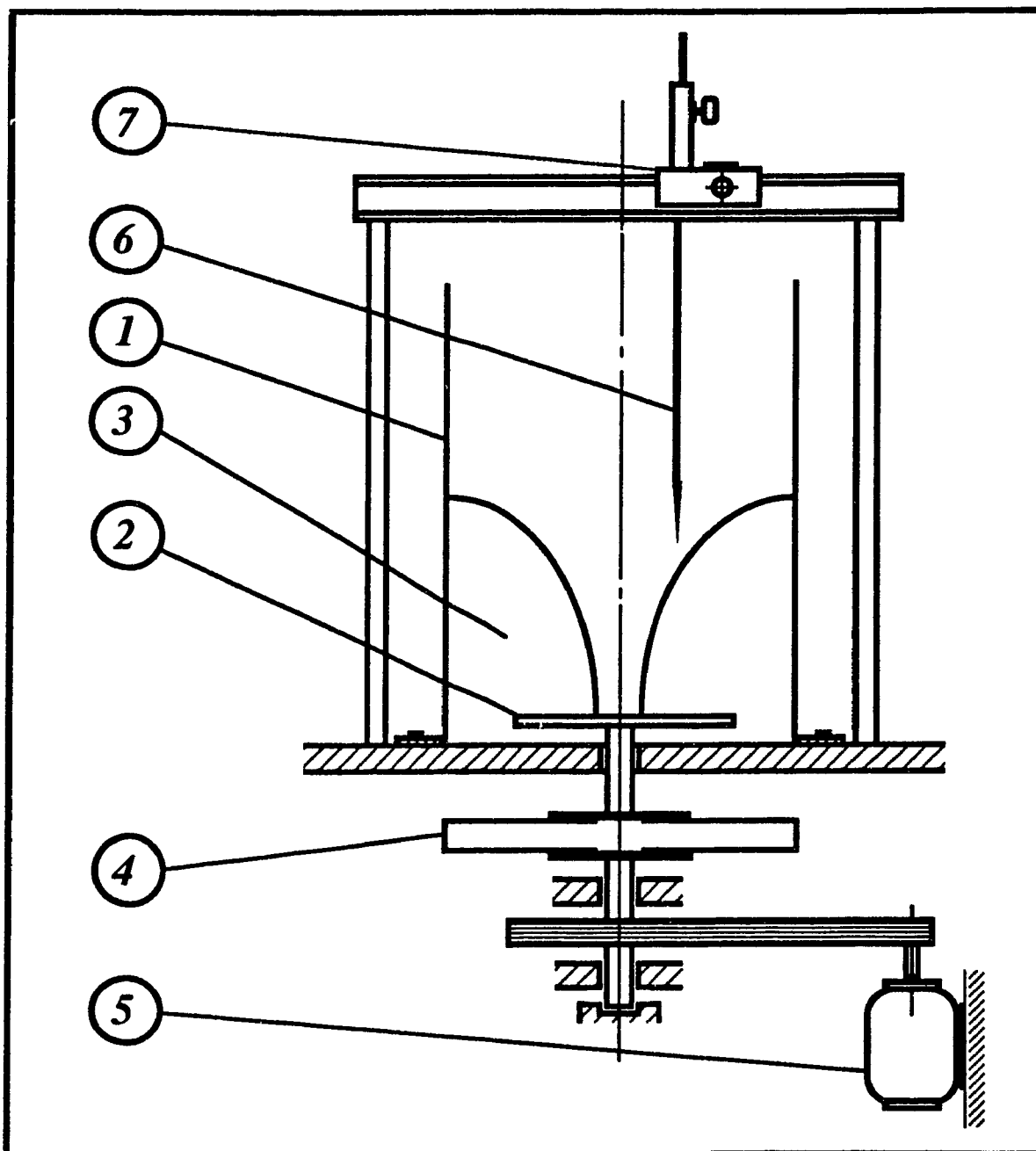
Another important parameter to the present analysis is the circulation. Given the angular velocity and geometry of the agitator, one is interested to know the strength of the produced vortex. A theoretical determination of the

latter quantities will require a complete theoretical flowfield characterization. This also is obtained experimentally.

For vortices with tall thin cores, the axisymmetric and bending waves described by Maxworthy et al (1985), and Maxworthy (1988) are known to force the vortex center to precess about the geometric center of the containing vessel in the direction of the rotating stirrer, and to undulate. For the cases where vortices with relatively short, thick cores were produced, the flowfield was nearly free from the above mentioned problems over a wide range of the parameters involved. Increasing the angular velocity beyond a certain critical value however, harmonic disturbances manifested by varicose undulations of the free-surface will emerge. Prichard (1970) waves inside the core are only present during the initial spin-up process. Such a perturbed state behavior of the core filament is beyond the scope of this experimental work. Hence, the previously presented analysis, and the results of the present investigations to be described in this section, are only valid when the influence of the perturbations on the main flow are either absent or negligibly small by comparison to the main flow.

3.1 Experimental Apparatus

The experimental trials are performed in a Plexiglass cylindrical container with an inner diameter of $11\frac{1}{4}$ inches (285.8 mm), partially filled with a liquid. The experimental facility is shown schematically in fig. 3.1. The experiments were performed using liquids with various viscosities; tap water, hydraulic oil (*Shell Tellus Oil - No. 46*) and a glyserol solution (66.7% of glyserol on the volume basis). The viscosities of these three liquids were measured using *the Cannon-Fenske Routine Viscometer*. The corresponding values of kinematic viscosities were found to be $9.87(10^{-7})$ m/s² for water; $3.4763(10^{-5})$ m/s² for the glyserol solution; and $1.0718(10^{-4})$ m/s² for oil. The vortex is generated by a system of an electric motor and a rotating (in the counter-clockwise direction) disk or a bar near the bottom of the container. Four different agitator sizes were used, 101, 151, 202 and 253 mm (numbers represent disk diameters or the length of the bars). The variation of the rotational speed is achieved by an electronic speed controller which permits the selection of speed up to 1200 r.p.m. The container is filled with a liquid to a given original height (H_0) which by the influence of a rotating disk or a cylindrical bar forms an inverted-bell-like free surface profile. The original heights are measured (using a ruler placed on the side of the cylindrical container) from the bottom of the container to a chosen level of the free surface, namely 100, 150, 200, 300 and 350 mm. The relative position of a free surface profile is measured using a point gage which is attached to a traversing mechanism on top of the container. This arrangement allowed gage movements in the three principal directions. The relative position of the needle is recorded using a high precision Vernier scale. The presence of a flywheel improves the constancy of rotary motion.



- | | |
|-------------------------|--------------------------|
| 1 - cylindrical tank | 5 - electric motor |
| 2 - rotating disk (bar) | 6 - measuring needle |
| 3 - working substance | 7 - transverse mechanism |
| 4 - flywheel | |

Fig. 3.1. Schematics of the apparatus.

3.2 Dimensional Analysis

The analysis given previously implied a known core radius. There must be a functional relationship between the core radius and the rest of the parameters involved. Since a theoretical determination is very difficult, dimensional analysis along with that presented in the previous chapter and experimental results will be used to derive such relationships. One expects the core size R_o and the vortex strength, Γ_∞ , to depend on the size of the agitator, R_d , the angular velocity, ω , the fluid density and viscosity, ρ , and, μ , respectively, the original height, H_o , and the radius of the containing vessel, R_t , fig. 3.2. Mathematically,

$$R_o = f_{1n} (\mu, \rho, \omega, R_d, R_t, H_o) \quad (3.1)$$

$$\Gamma_\infty = f_{2n} (\mu, \rho, \omega, R_d, R_t, H_o) \quad (3.2)$$

Application of Buckingham π -theorem gives the following relations:

$$R_o/R_d = f_{1n} (Re = \omega R_d^2/\nu, R_d/R_t, H_o/R_d); \quad (3.3)$$

$$\Gamma_\infty / \omega R_d^2 = f_{2n} (\omega R_d^2/\nu, R_d/R_t, H_o/R_d) \quad (3.4)$$

where, Re is a Reynold's number which is a non-dimensional representation of a tangential velocity measured at the tip of the disk or the bar and other dimensionless groups are the geometrical representations of characteristic dimensions.

The next step is to establish a procedure to relate these non-dimensional groups. Consider eq. (3.1) and eq. (3.3) which both relate the dimensionless

radius and other parameters through an unknown function, f_{1n} . Qualitatively, f_{1n} is to

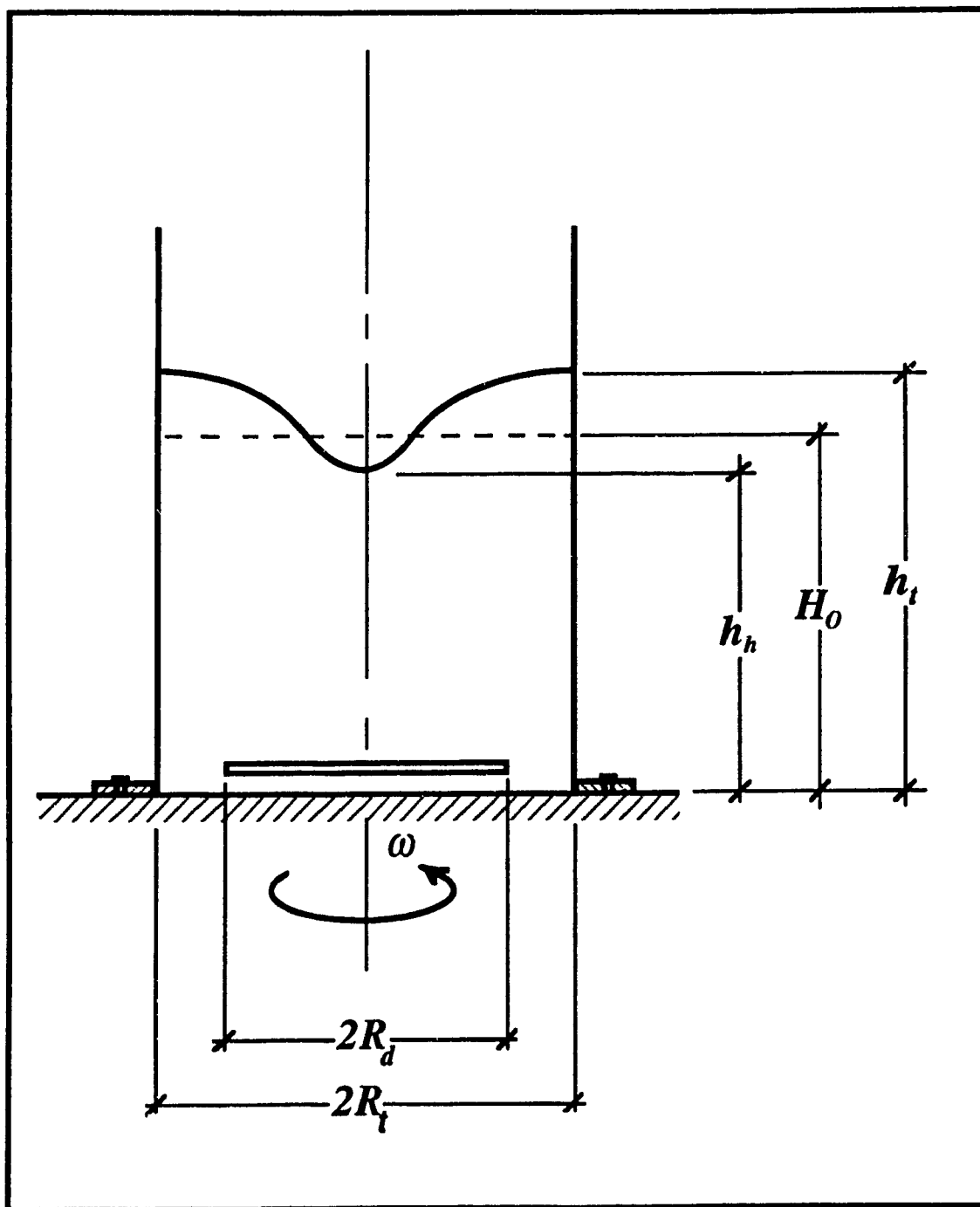


Fig. 3.2. Characteristic dimensions.

be determined keeping in mind that the total liquid volume, before and after rotation, remains the same.

Employing the new formula for the free surface distribution, assuming that the general shape given by eq. (2.24) represents well the real interface, one can integrate to find the total liquid volume under the free surface,

$$2\pi \int_0^{\bar{R}_t} \frac{2r}{\pi} \tan^{-1} \bar{r}^2 dr = 2\bar{R}_t^2 \tan^{-1} \bar{R}_t^2 - \ln(\bar{R}_t^4 + 1) \quad (3.5)$$

where $\bar{r} = r/R_0$ and $\bar{R}_t = R_t/R_0$. Equating the volumes of liquid inside the container before and after rotation gives,

$$\pi \frac{H_0 - h_h}{h_\infty - h_h} \bar{R}_t^2 = 2\bar{R}_t^2 \tan^{-1} \bar{R}_t^2 - \ln(\bar{R}_t^4 + 1) \quad (3.6)$$

From eq. (2.24),

$$\frac{h_t - h_h}{h_\infty - h_h} = \frac{2}{\pi} \tan^{-1} \bar{R}_t^2 \quad (3.7)$$

Solving the above equation for $h_\infty - h_h$ one obtains:

$$h_\infty - h_h = \frac{\pi}{2} \frac{h_t - h_h}{\tan^{-1} \bar{R}_t^2} \quad (3.8)$$

Substituting eq. (3.8) into eq. (3.7) gives

$$\frac{H_0 - h_h}{h_t - h_h} = 1 - \frac{\ln(\bar{R}_t^4 + 1)}{2\bar{R}_t^2 \tan^{-1} \bar{R}_t^2} \quad (3.9)$$

The above equation can be rearranged to attain the implicit form:

$$\ln(\bar{R}_t^4 + 1) + \frac{(1 - 1)}{\delta} 2\bar{R}_t^2 \tan^{-1}\bar{R}_t^2 = 0 \quad (3.10)$$

where,

$$\delta = \frac{h_t - h_h}{H_o - h_h}$$

Eq. (3.10) is a non-linear algebraic equation which implies that an analytical solution is not available. The application of a numerical method to obtain the root for R_t is therefore required. This is achieved using the Newton-Raphson method for a given value of δ . Alternatively, eq. (3.10) can be expressed in an explicit form in terms of the dimensionless parameter, δ , which implies that the graphical solution is also available:

$$\delta = \frac{2\bar{R}_t^2 \tan^{-1}\bar{R}_t^2}{2\bar{R}_t^2 \tan^{-1}\bar{R}_t^2 - \ln(\bar{R}_t^4 + 1)} \quad (3.11)$$

However, contrary to the above equation, δ , in the present analysis, serves as an independent variable. The graphical representation of eq. (3.11) is illustrated on fig. 3.3. The purpose of employing eq. (3.11) is to ascertain the behavior of δ versus R_t which may guide to a proper numerical method as well as an appropriate initial guess for the Newton-Raphson method. By definition $\bar{R}_t = R_t/R_o$. Therefore, for a given value of R_t , which is the inner radius of a cylindrical container, the radius of a core is to be determined:

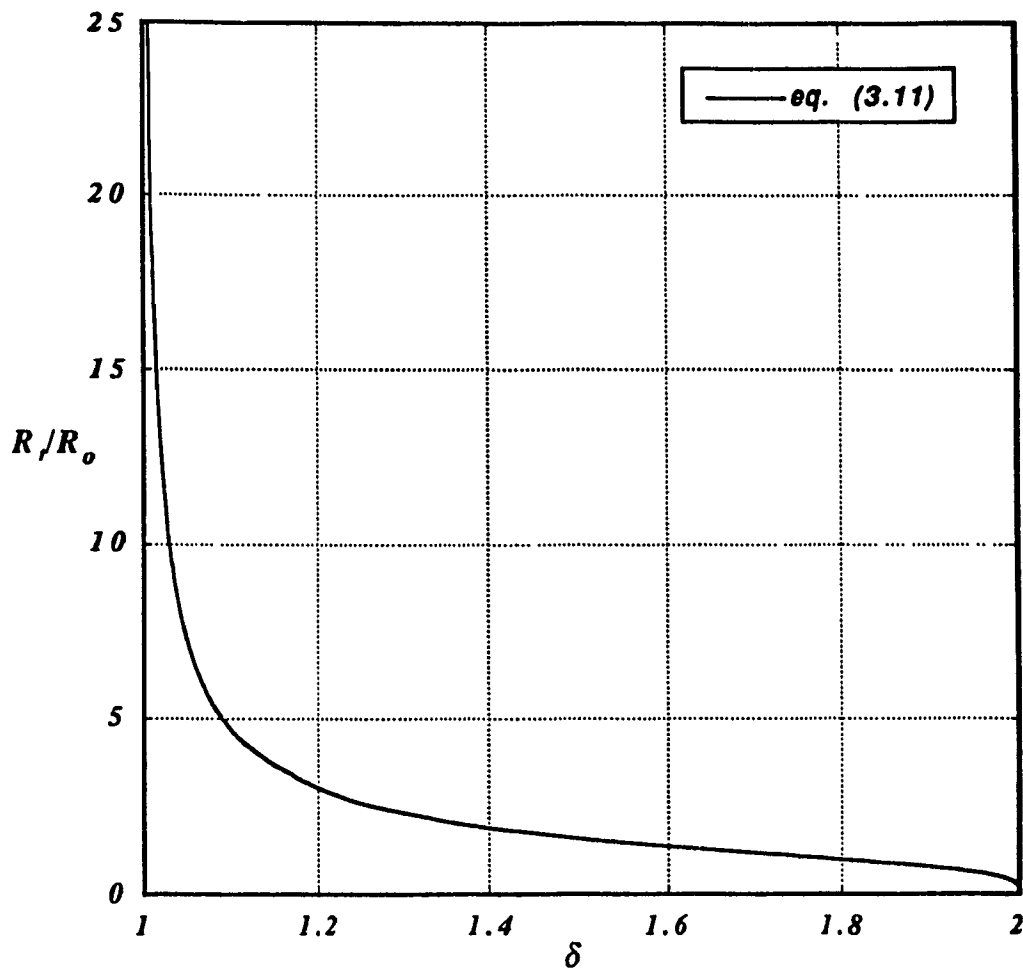
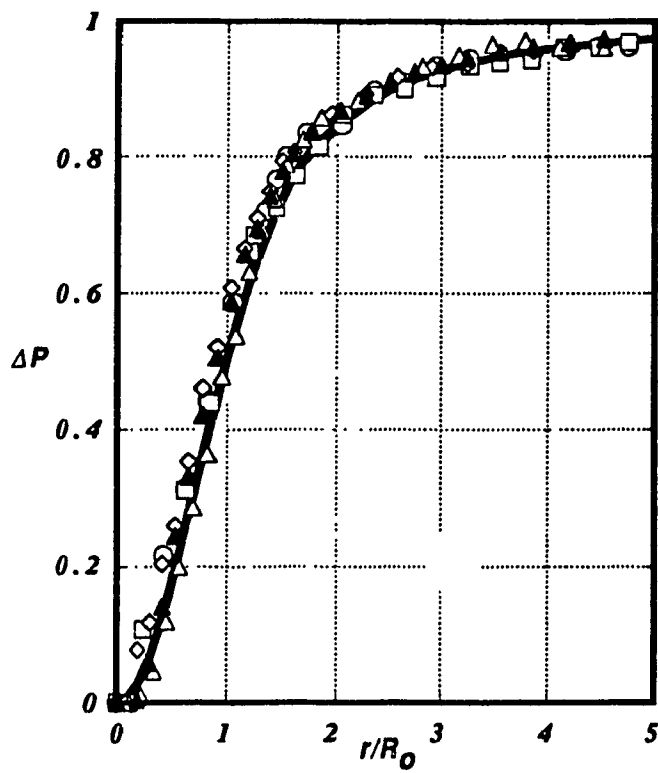


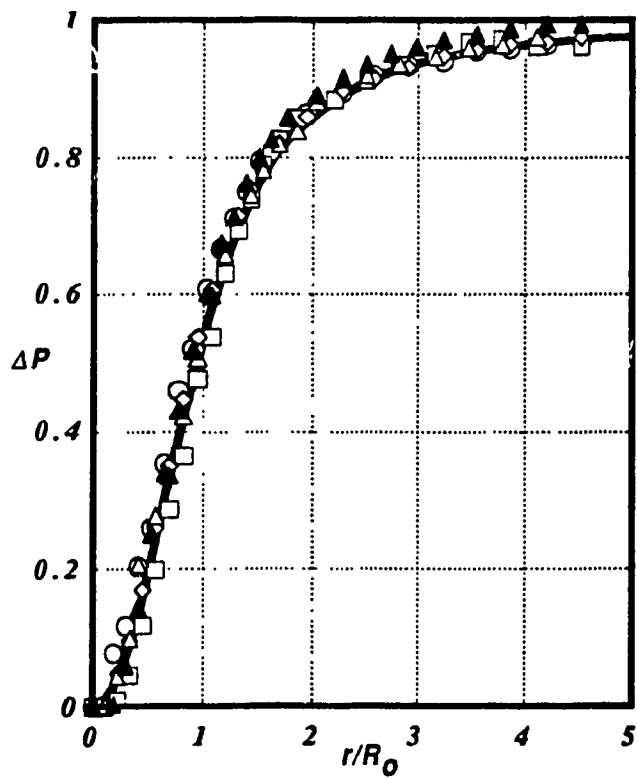
Fig. 3.3. Relationship between two dimensionless groups.

$$R_o = R_t / \bar{R}_t$$

Using the free-surface elevations measured via a point gage and the core radius obtained solving eq. (3.10) one can plot the non-dimensional free-surface shape as a function of the dimensionless radius. A large number of such graphes representing the interface under different conditions were produced. Here, a sample of several such profiles are shown in fig. 3.4. It is evident that the correlation is satisfactory.

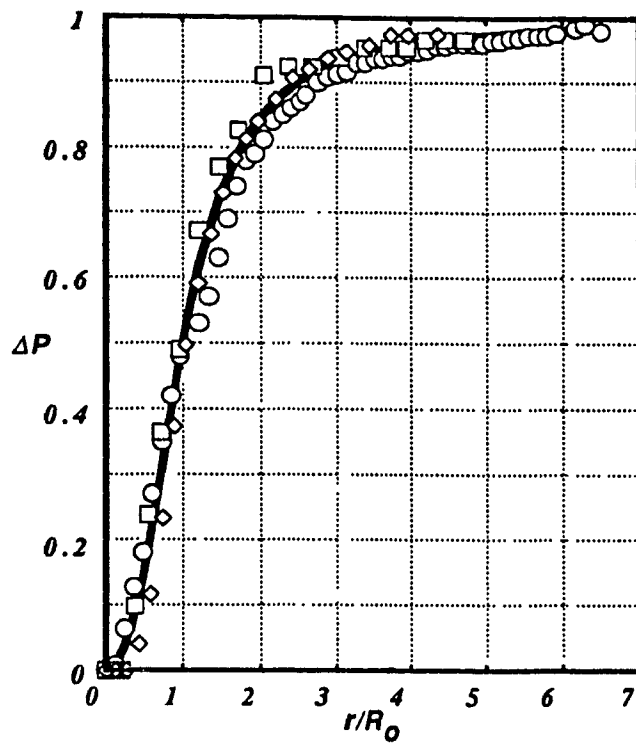


(a) disk



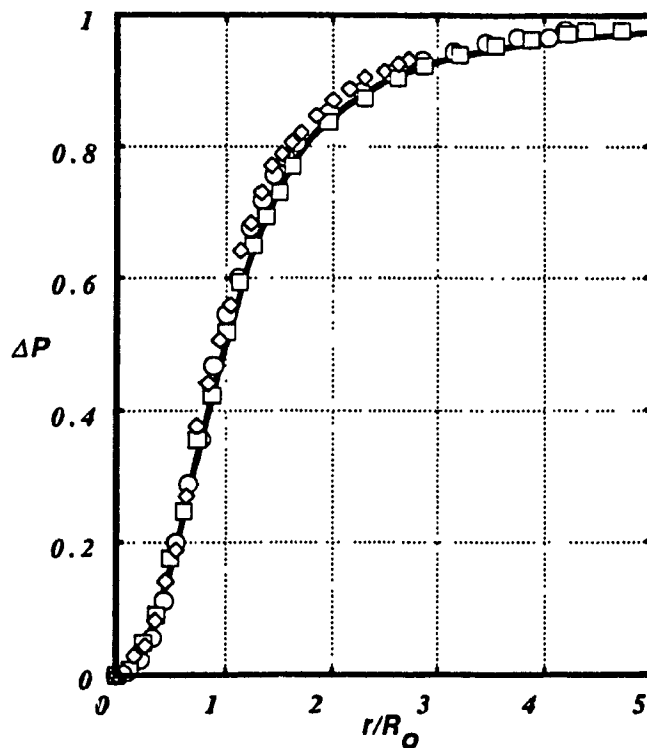
(b) bar

Fig. 3.4.a & b. The free surface profile - experimental points for a disk and bar as a rotating boundary.



- new formula, eq. (2.24)
- $Re = 159,641.7$,
 $Ho/Rd = 6.7627$, $Rd = 0.0505$ m
- $Re = 135,289.6$,
 $Ho/Rd = 7.4753$, $Rd = 0.0505$ m
- ◇ $Re = 108,231.2$,
 $Ho/Rd = 3.3775$, $Rd = 0.0755$ m

(c) disk



- new formula, eq. (2.24)
- $Re = 135,289.6$,
 $Ho/Rd = 3.8415$, $Rd = 0.0505$ m
- $Re = 108,231.7$,
 $Ho/Rd = 7.4753$, $Rd = 0.0505$ m
- ◇ $Re = 81,173.25$,
 $Ho/Rd = 5.0794$, $Rd = 0.0755$ m

(d) bar

Fig. 3.4.c & d. The free surface profile - experimental points for a disk and bar as a rotating boundary.

Similarly, the vortex strength, Γ_∞ can be related to the depression of the free surface interface, $h_t - h_h$, employing the boundary condition at the infinite radius for the new pressure distribution given in Appendix A,

$$\left(\frac{\Gamma_\infty}{2\pi R_o} \right)^2 \frac{\rho}{P_\infty - P_h} = \frac{4}{\pi} \quad (3.12)$$

Rearranging the terms of the above relationship and expressing the pressure as a hydraulic height, one can obtain the following expression for the free surface depression in a cylindrical container of finite diameter,

$$H_o - h_h = \frac{\Gamma_\infty^2}{16\pi R_o^2 g} \quad (3.13)$$

since $h_t - H_o$ is to be measured experimentally, Γ_∞ is considered to be a dependent variable,

$$\Gamma_\infty = 4R_o \sqrt{\pi g (h_\infty - h_h)} \quad (3.14)$$

where g is the gravitational constant. However, the experimental apparatus has a container of finite diameter which inevitably requires one to relate relating the vortex strength to the actual depression of a free surface. Employing eq. (2.24) for the free surface profile yields,

$$h_\infty - h_h = \frac{2(h_t - h_h)}{\pi \arctan(\overline{R}_t^2)} \quad (3.15)$$

Substituting eq. (3.15) into eq. (3.14) one obtains,

$$\Gamma_\infty = \pi R_o \sqrt{\frac{8g(h_t - h_h)}{\arctan(\overline{R}_t^2)}} \quad (3.16.a)$$

or

$$\bar{\Gamma}_{\infty} = \frac{\pi R_o}{vRe} \sqrt{\frac{8g(h_t - h_h)}{\arctan(\bar{R}_t^2)}} \quad (3.16.b)$$

The calculation of the free surface depression also permits the determination of the corresponding Froude number, defined as

$$Fr_o = \frac{V_{\theta_o}^2}{R_o g} \quad (3.17)$$

where, V_{θ_o} is the azimuthal velocity component at the core radius. By definition,

$$\Gamma_{\infty} = 2\pi R_o V_{\theta} \text{ or } 2\pi R_o V_{\theta_o}$$

which shows that,

$$Fr_o = \frac{\Gamma_{\infty}^2}{4\pi^2 R_o^3 g} \quad (3.18)$$

From eq. (2.24) the Froude number can also be given by,

$$Fr_o = \frac{2(h_t - h_h)}{R_o \arctan(\bar{R}_t^2)} \quad (3.19)$$

The prime objective here is to establish through experiments the relationships among the main non-dimensional parameters given by eqs. (3.3) and (3.4).

3.3 The Core Size and the Vortex Strength

The validity of eq. (2.24) in representing the observed free surface has been established in the previous section. Here the new model together with experimental free-surface data are employed to obtain the characteristics of the core and the vortex strength.

The experimental trials are combined in sets of data corresponding to a single disk or bar diameter for five different positions of undisturbed free surface levels. For each particular original height, the free surface levels are measured at the geometrical center and at the circumferential wall of the container using a high-precision measuring needle; the measurements are conveyed in pairs of readings of free surface levels, namely h_h, h_t for 15-20 values of agitator speed which is controlled by an electronic speed controller and monitored by a digital read-out angular speed gauge. The choice of angular speed entirely depends on general behavior of a vortex core. The aim is to avoid regimes at which the flowfield is perturbed by undesirable wave activity. In particular, if the speed is very low, column undulation and precession occurs. Yet, if the speed is considerably high, large corrugation and sloshing appear. Hence, for one particular value of the original height, the angular velocity is bounded in a range at which the flowfield remains relatively undisturbed.

To engage the previously introduced theoretical relations, a pair of readings of the free surface profile is employed to calculate a dimensionless quantity, δ and a free surface depression which must be a function of Re , R_d/R_t and H_0/R_d . Solution of eq. (3.10) permits the determination of the radius of the

core for a fixed value of δ . It is then utilized to determine a functional dependence among the dimensionless groups involved in eq. (3.3). A large number of experiments have been performed using different liquids, agitator sized and initial heights. The outcome of the experimental work is shown in the fig. 3.5. It is clear from these results that the dimensionless core radius depends simply on the geometry of the problem.

The functional dependance of R_o/R_d to R_d/R_t is illustrated graphically in fig. 3.6. According to the figure, all the points fall approximately on a straight line declining as the relative size of the agitator increases. It can also be seen that it is not important what type or agitator is used. It is worth noting in passing that Vatistas (1986) arrived at a similar conclusion (that the core depends solely on geometrical parameter β) for the vortex produced in a vortex chamber.

Similarly, the implementation of eq. (3.14) permitted the determination of the vortex strength as a function of the prevailing dimensionless groups. The results are presented graphically in fig. 3.7. Each particular graph corresponds either to a disk or a bar diameter, and the three working liquids on the figure demonstrates a certain functional dependence between the vortex strength, Re and the original height. The results indicate that for water the vortex strength remains almost constant as Re increases. For oil and glyserol solution, which have higher values of viscosity, the results possesses an almost linear dependence with positive slope among the strength and Reynold's number.

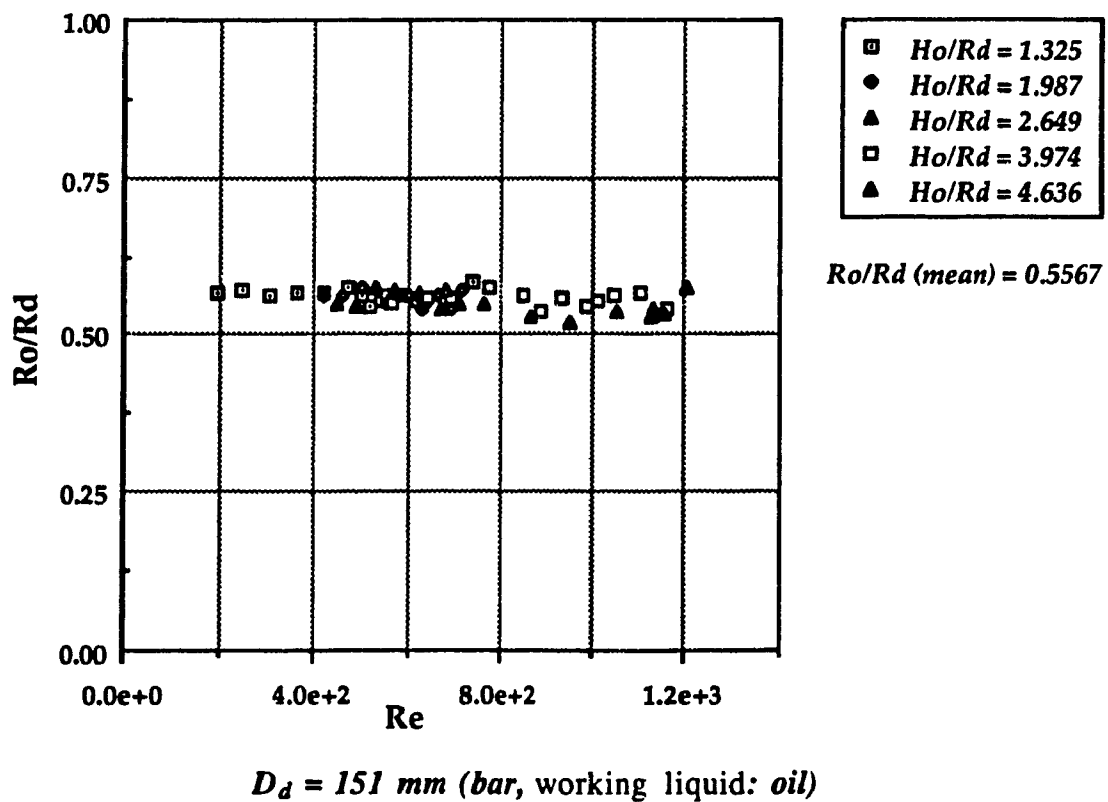
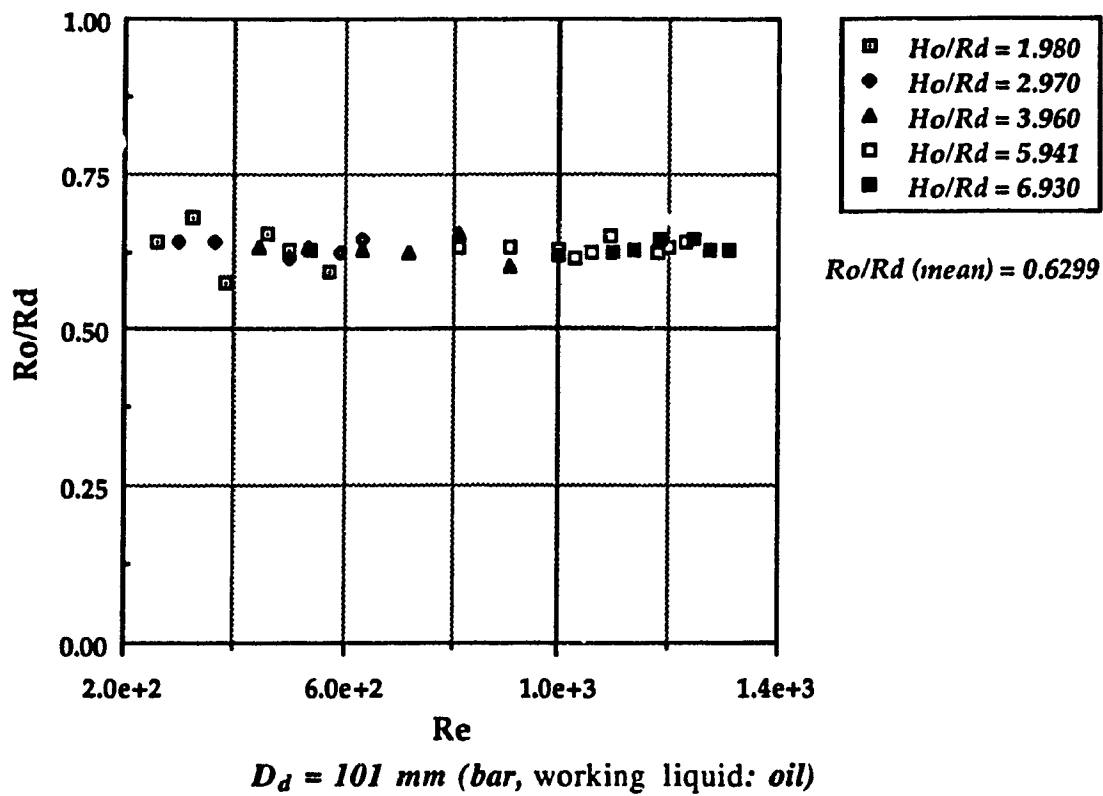


Fig. 3.5.a. A radius of a core is constant as Re varies.

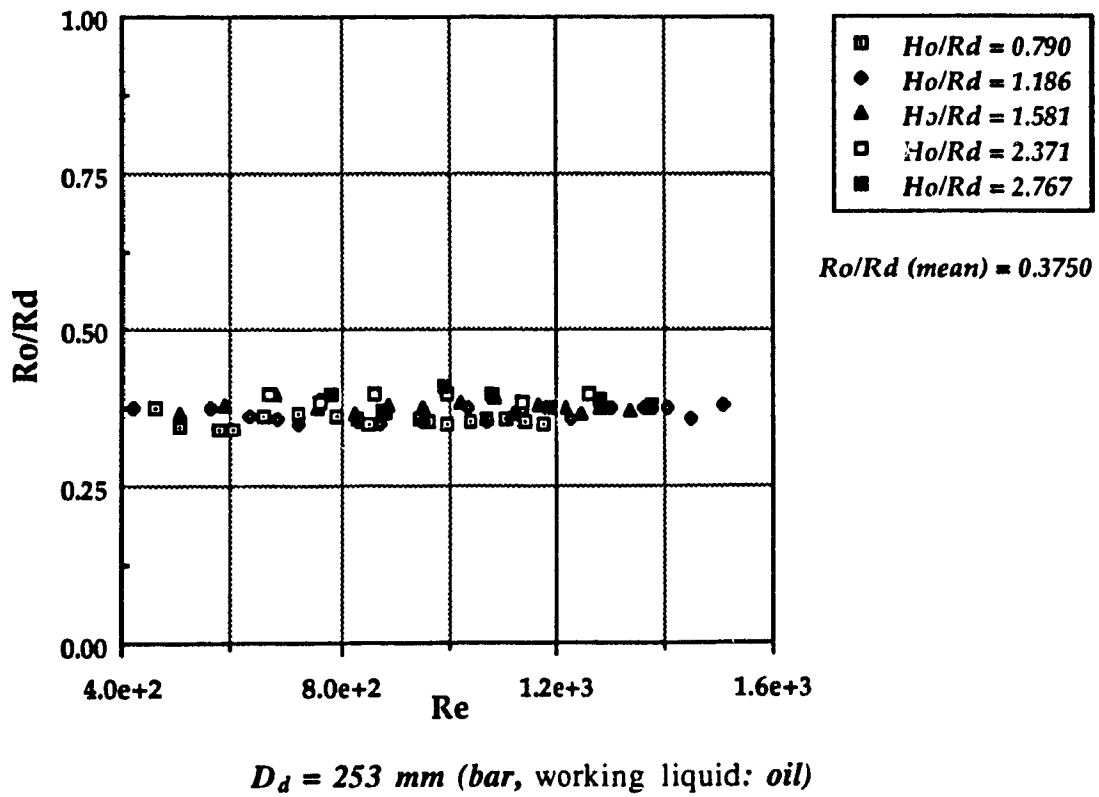
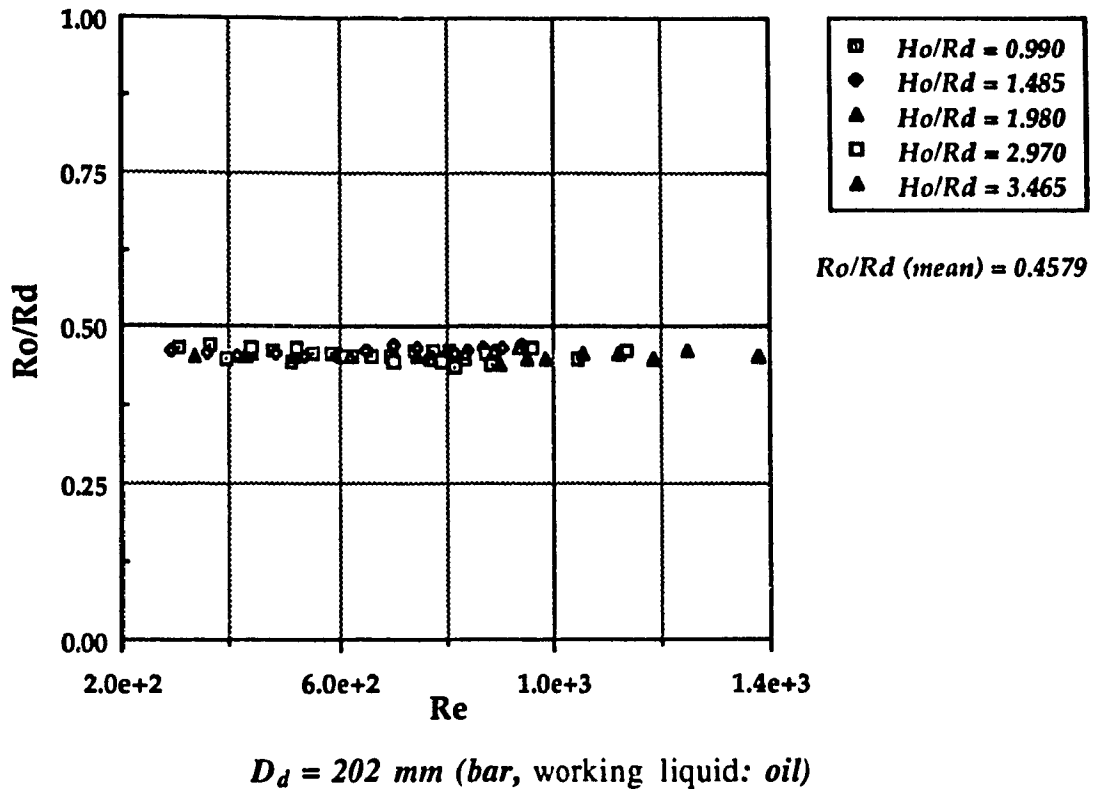


Fig. 3.5.b. A radius of a core is constant as Re varies.

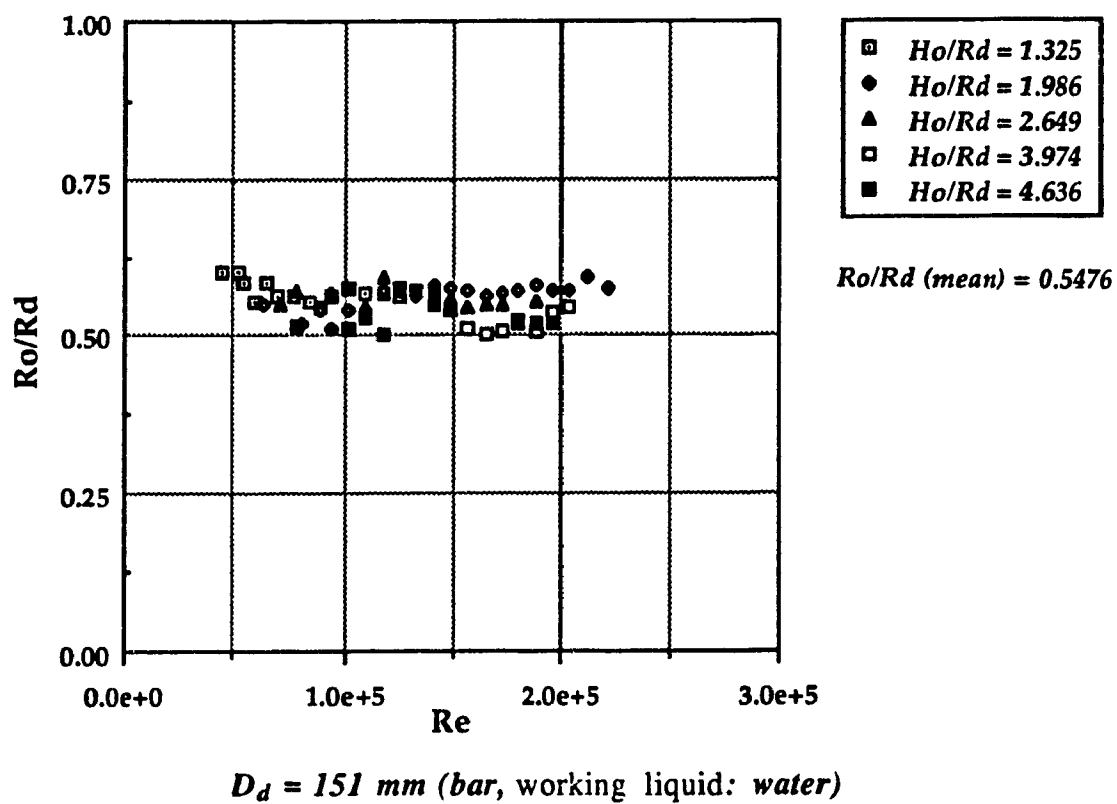
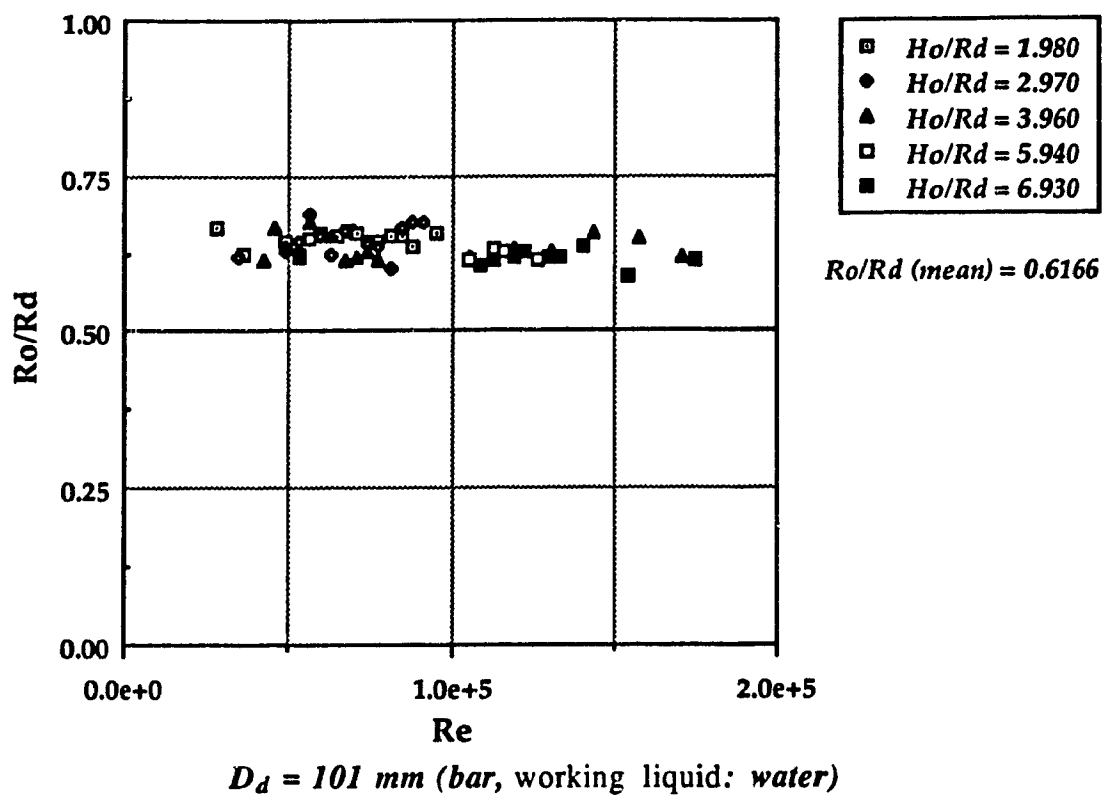


Fig. 3.5.c. A radius of a core is constant as Re varies.

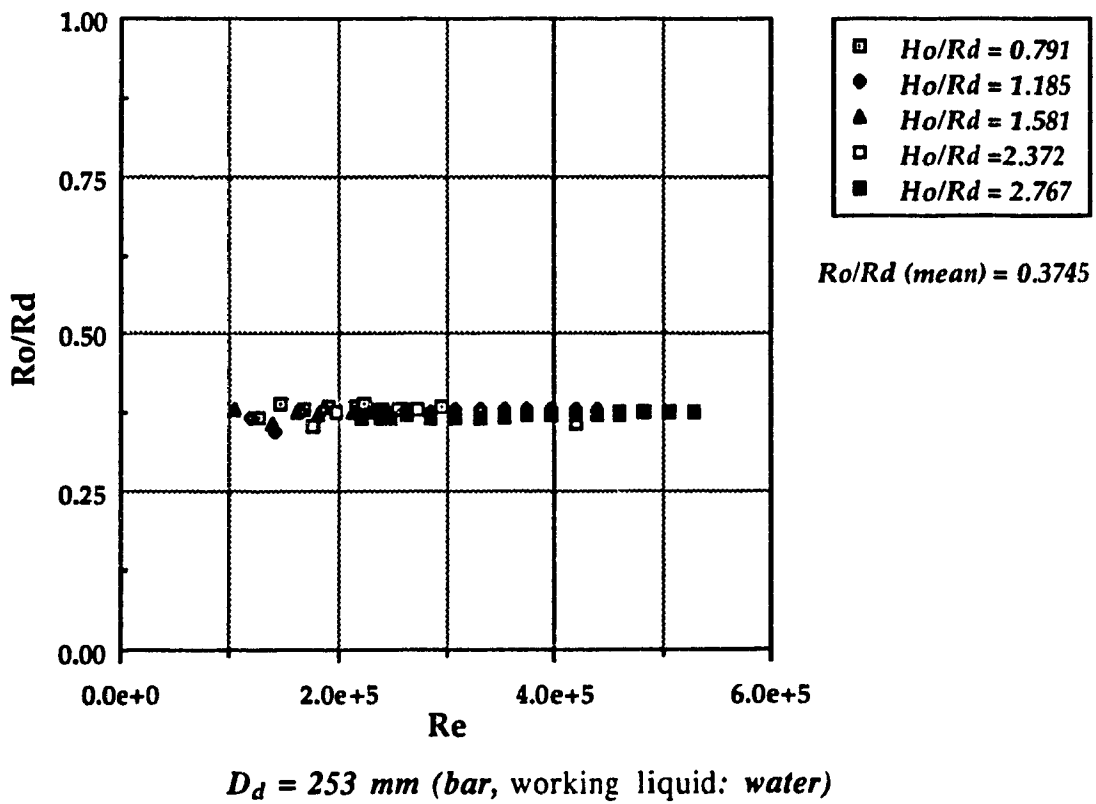
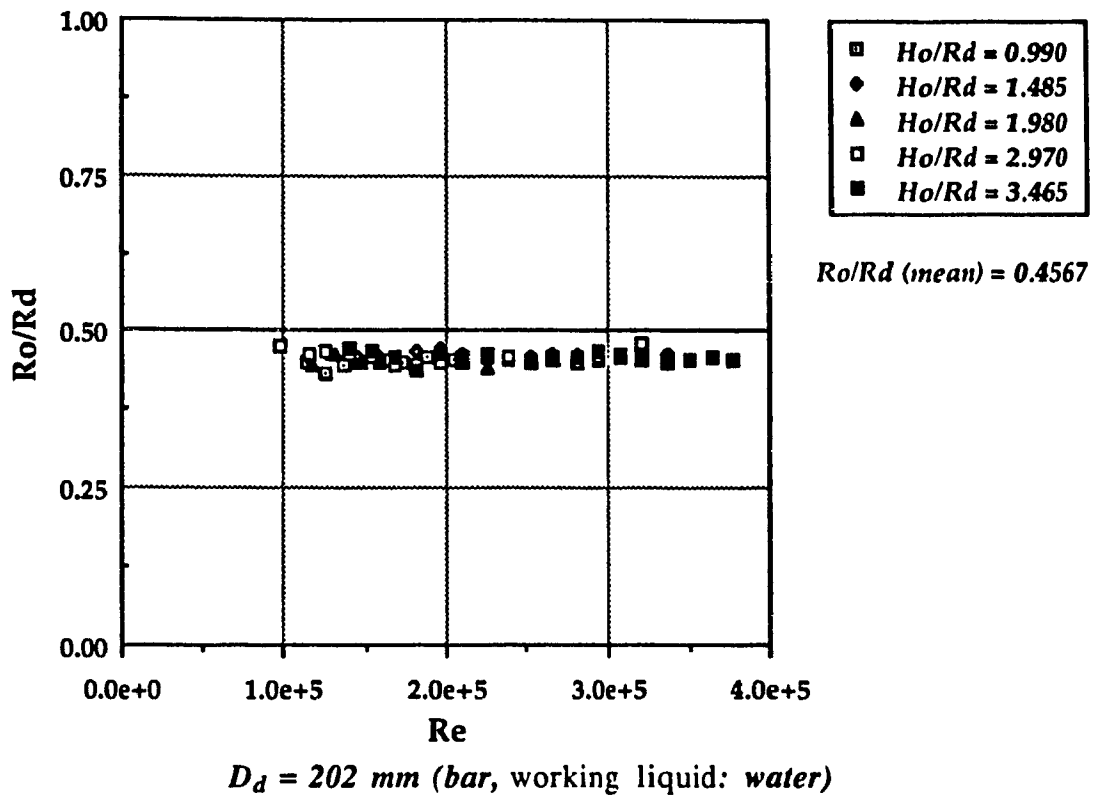
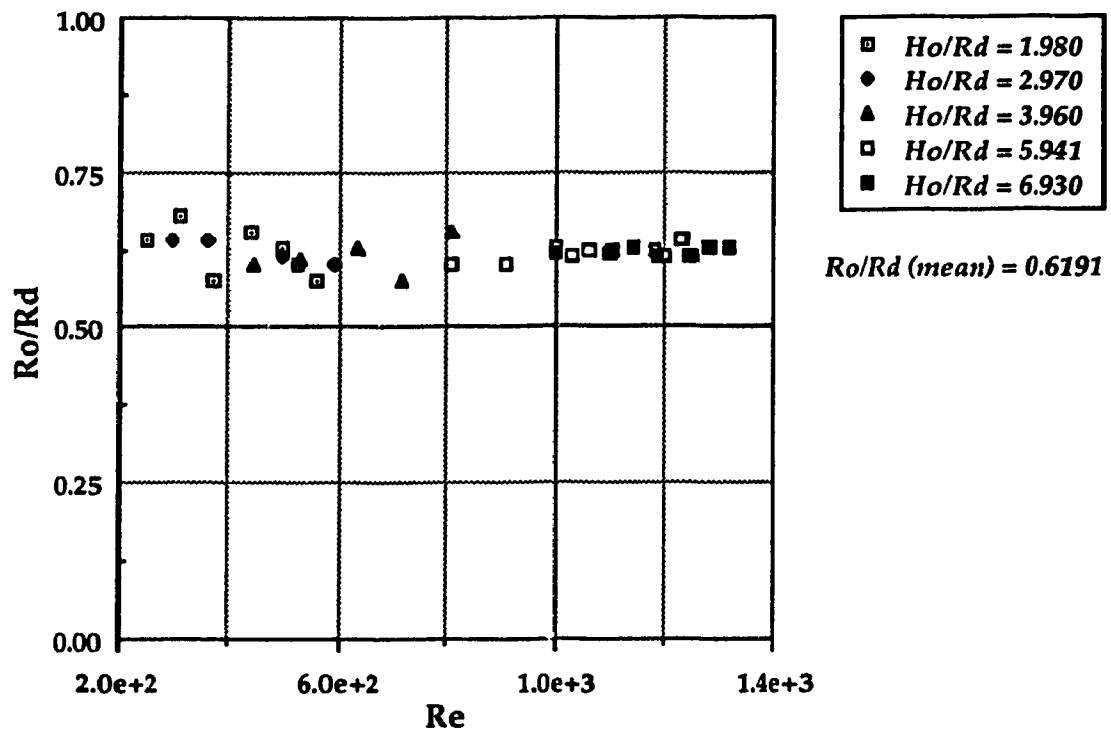
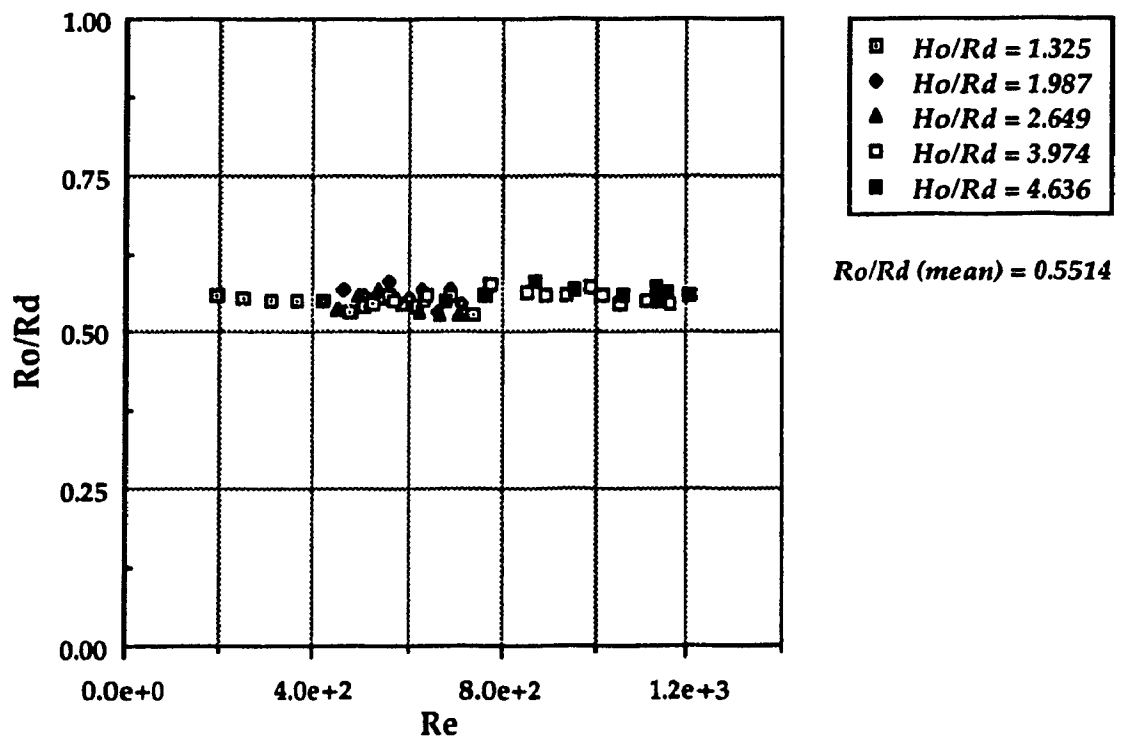


Fig. 3.5.d. A radius of a core is constant as Re varies.



$D_d = 101$ mm (disk, working liquid: oil)



$D_d = 151$ mm (disk, working liquid: oil)

Fig. 3.5.e. A radius of a core is constant as Re varies.

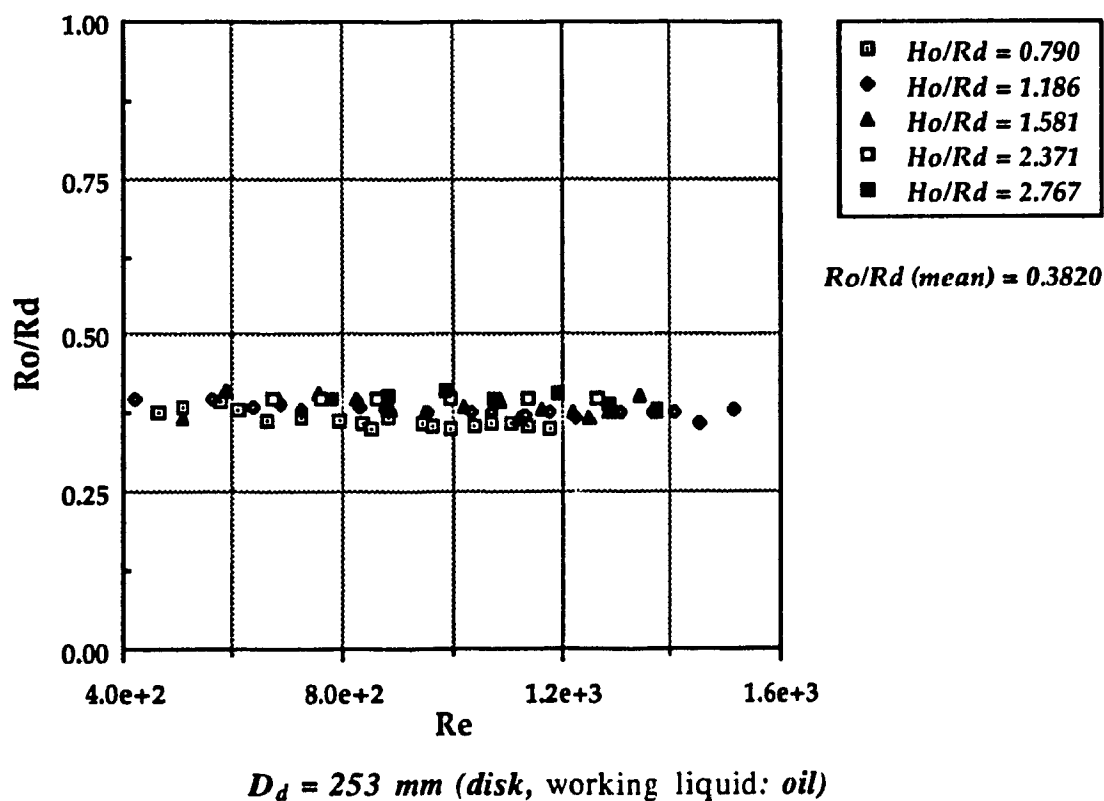
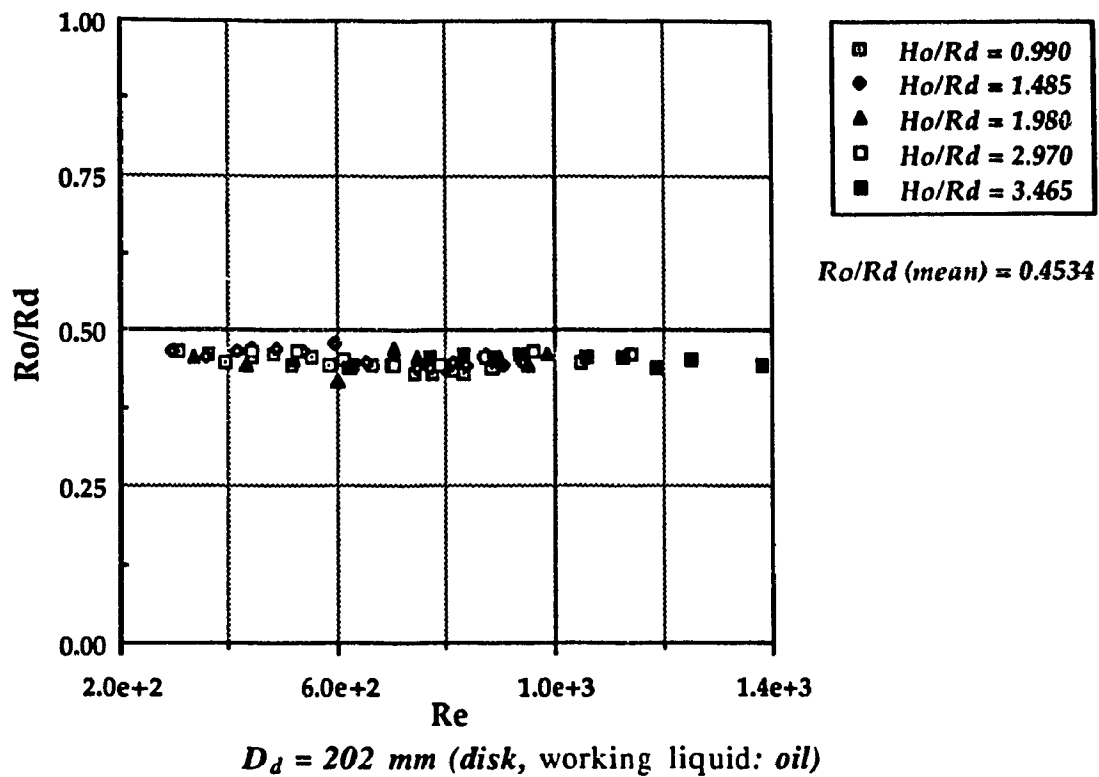


Fig. 3.5.f. A radius of a core is constant as Re varies.

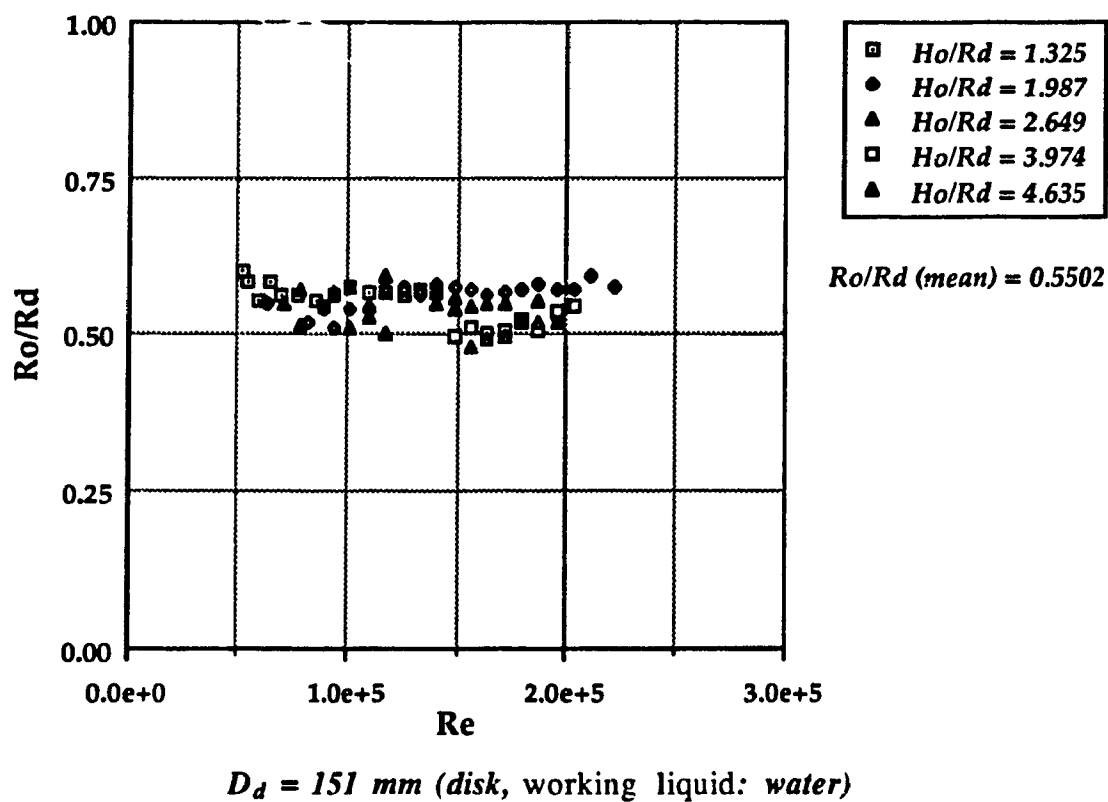
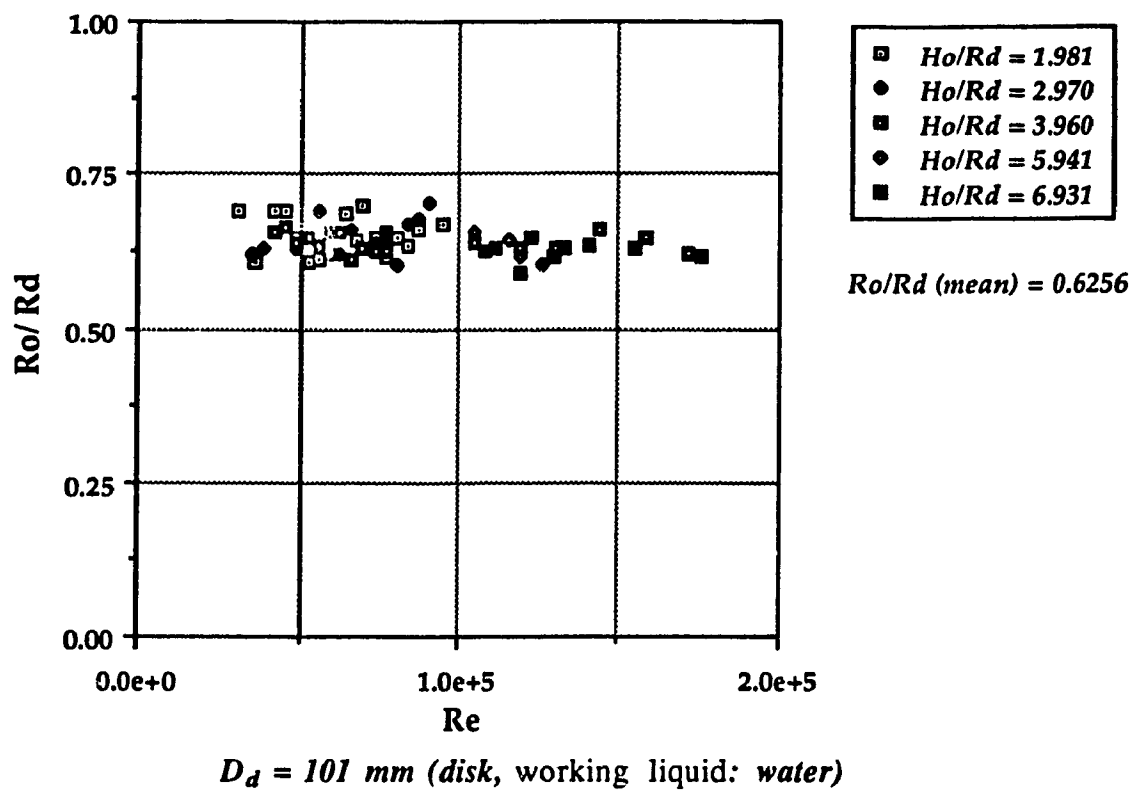


Fig. 3.5.g. A radius of a core is constant as Re varies.

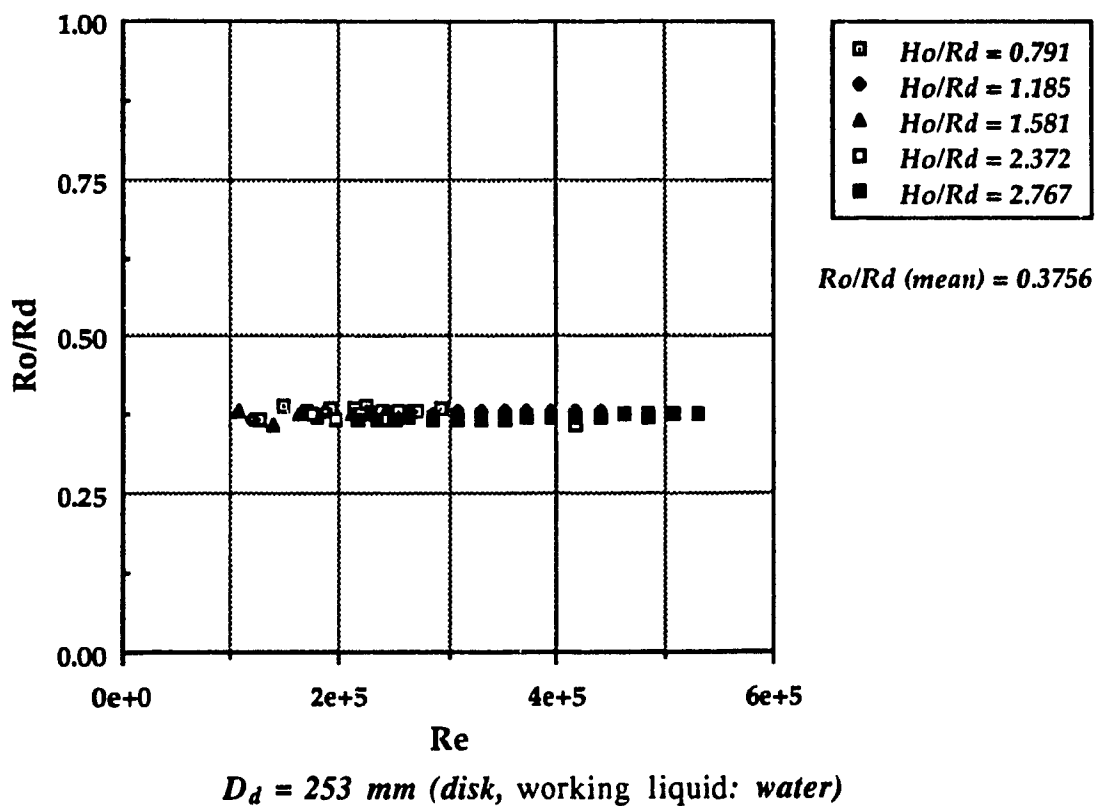
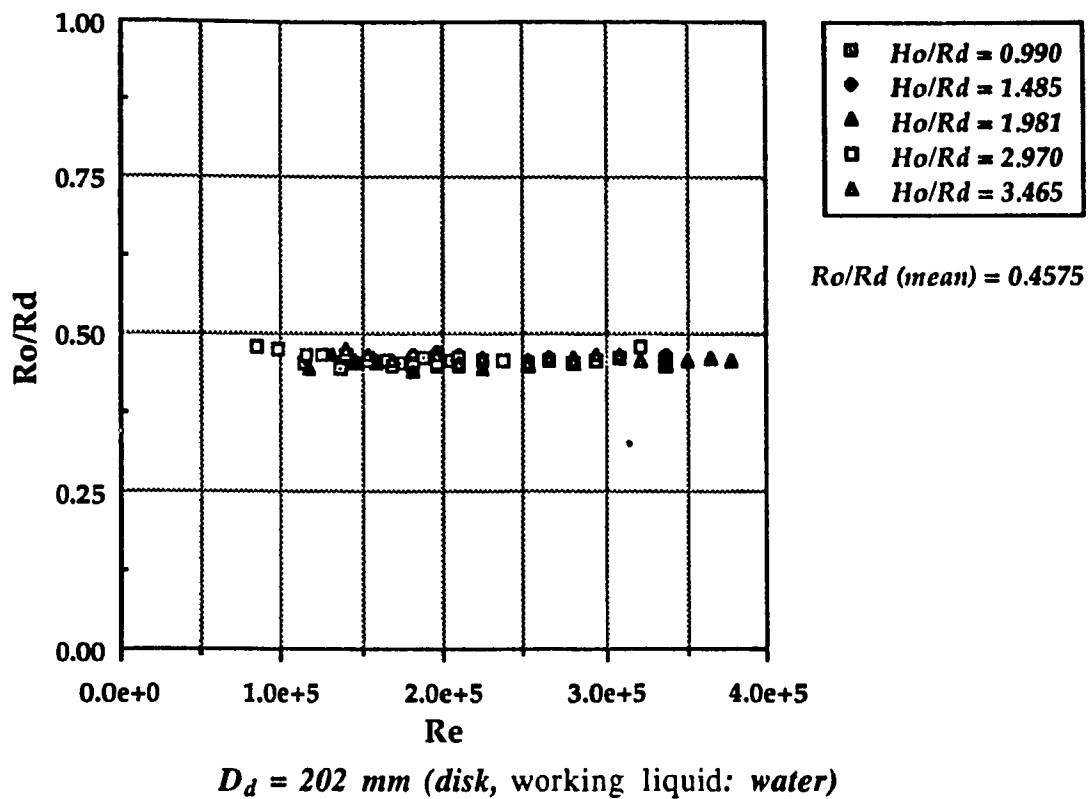


Fig. 3.5.h. A radius of a core is constant as Re varies.

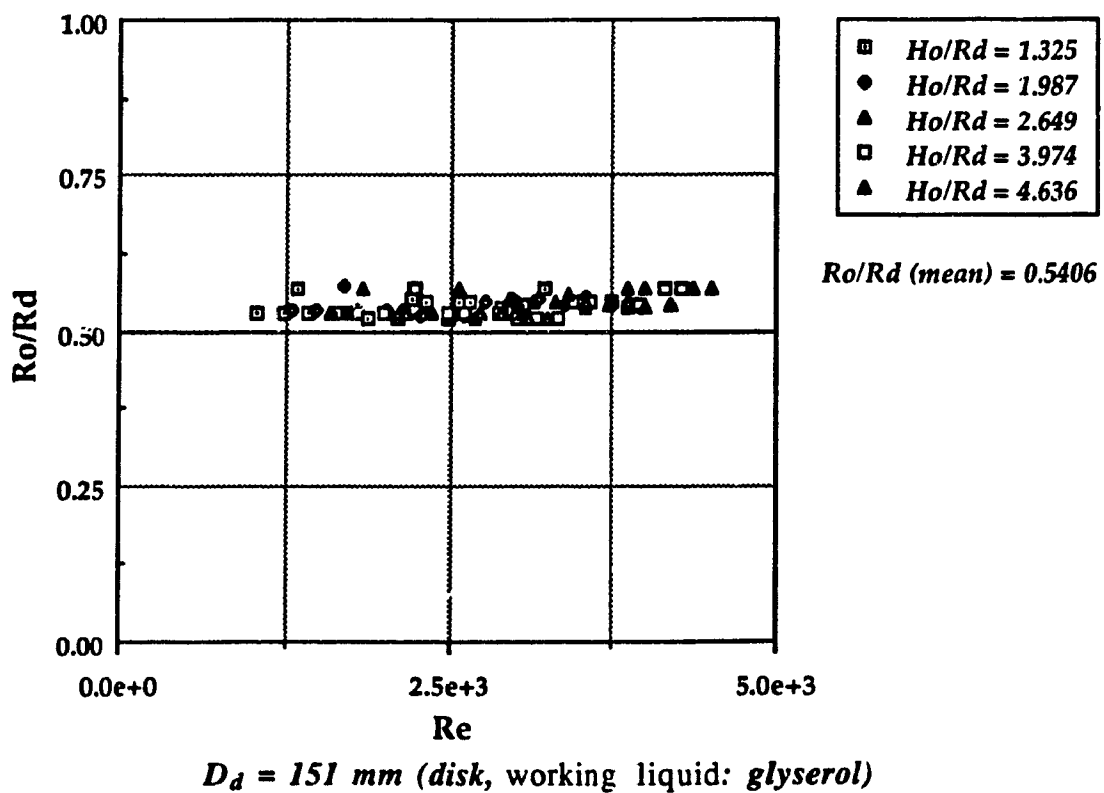
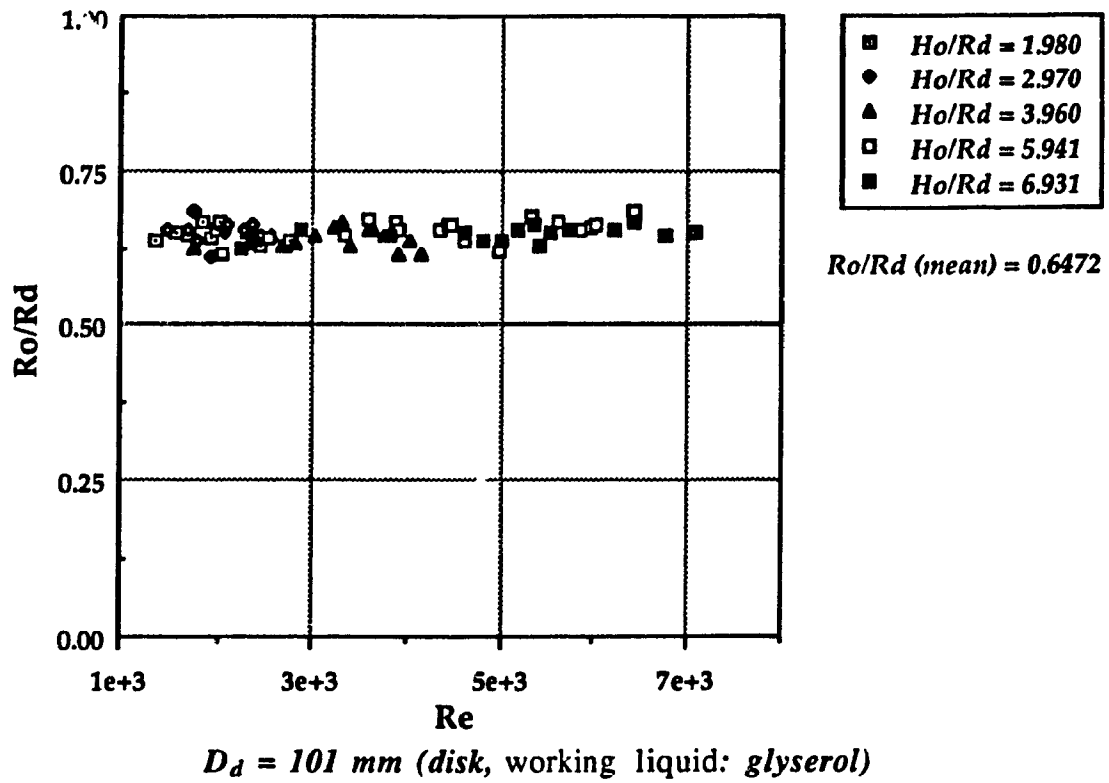


Fig. 3.5.i. A radius of a core is constant as Re varies.

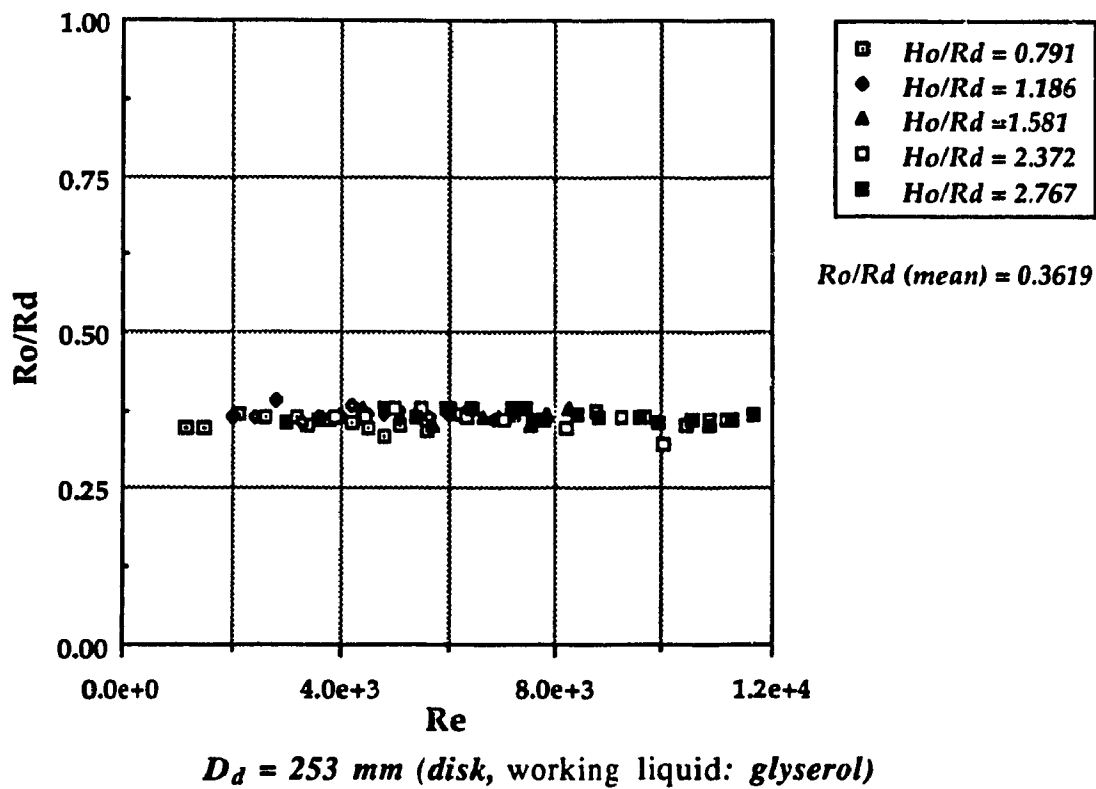
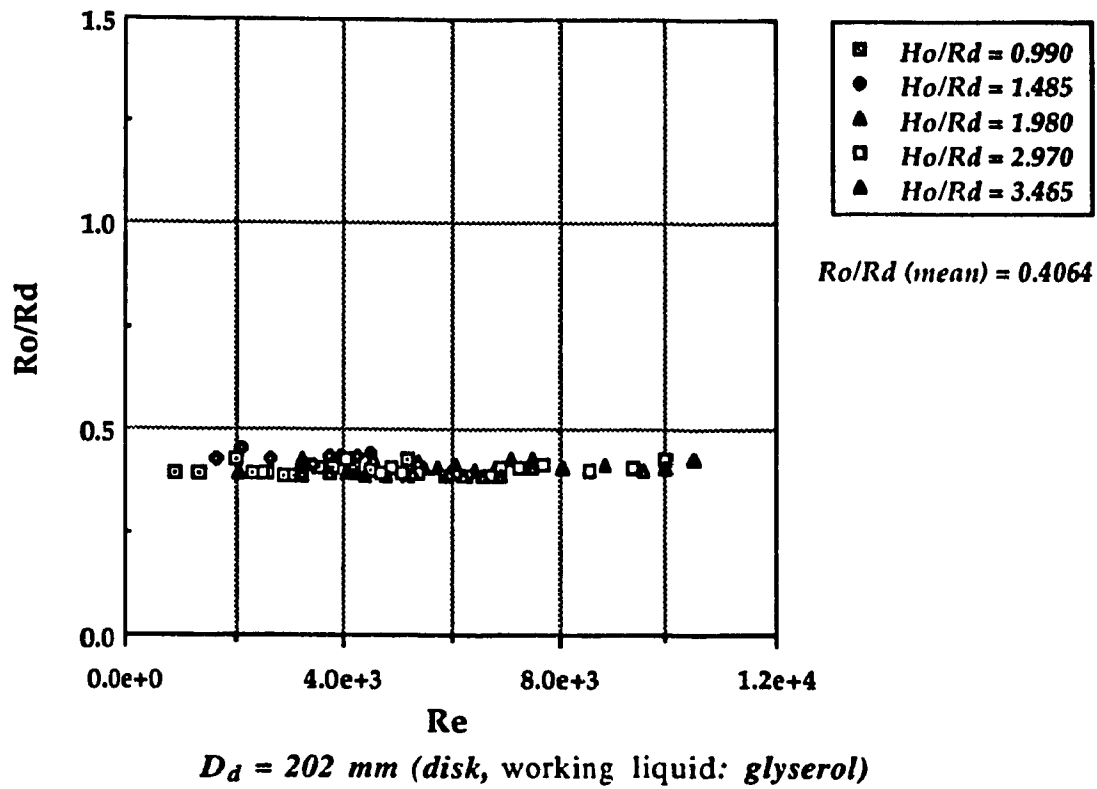
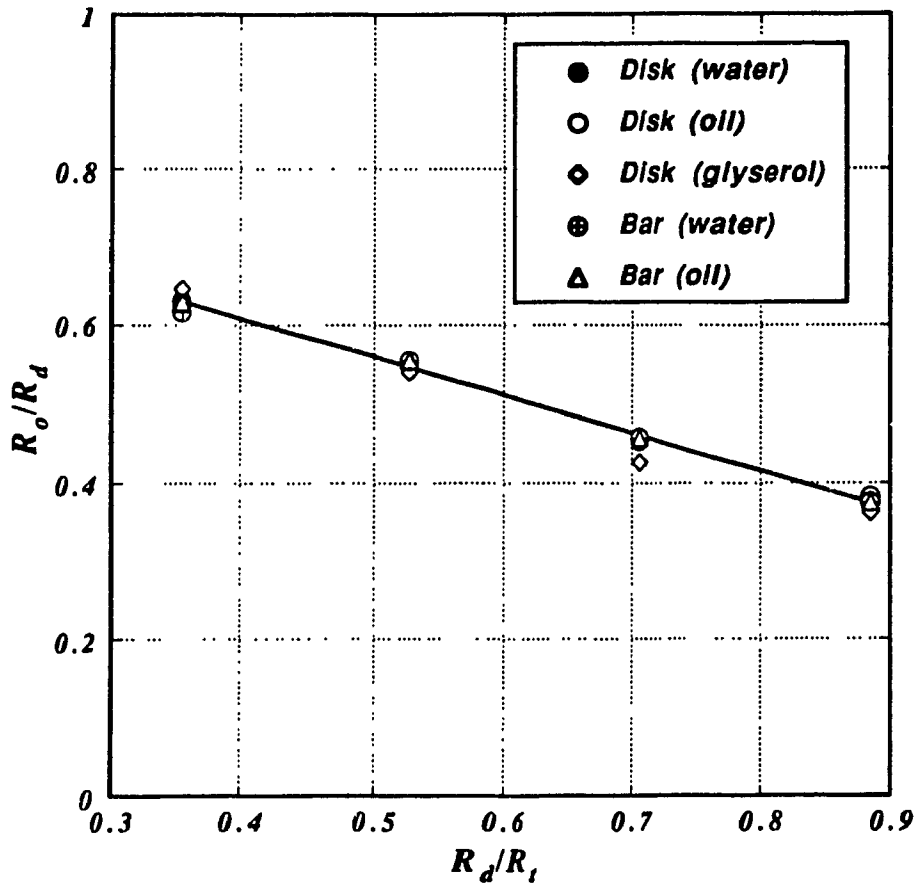


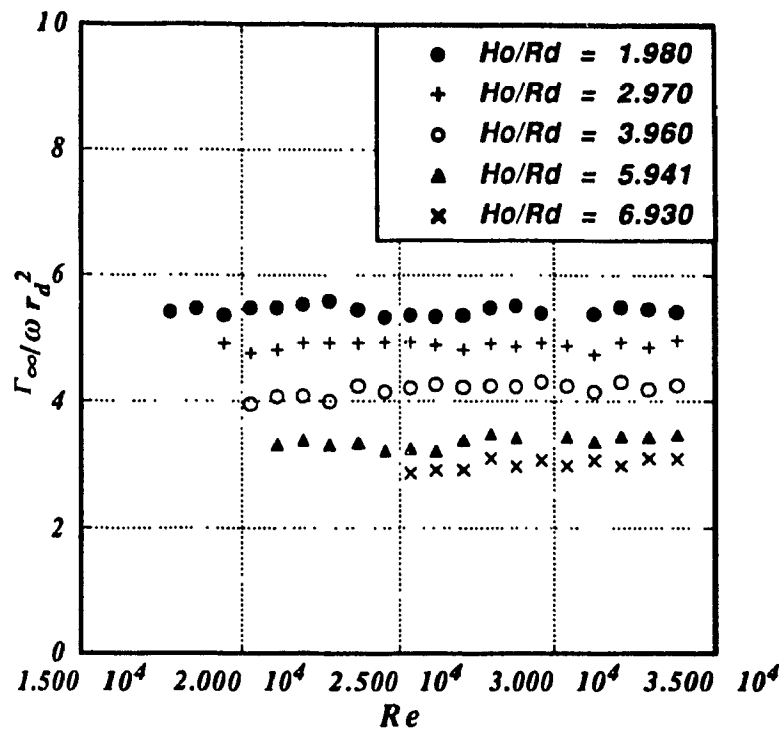
Fig. 3.5.j. A radius of a core is constant as Re varies.



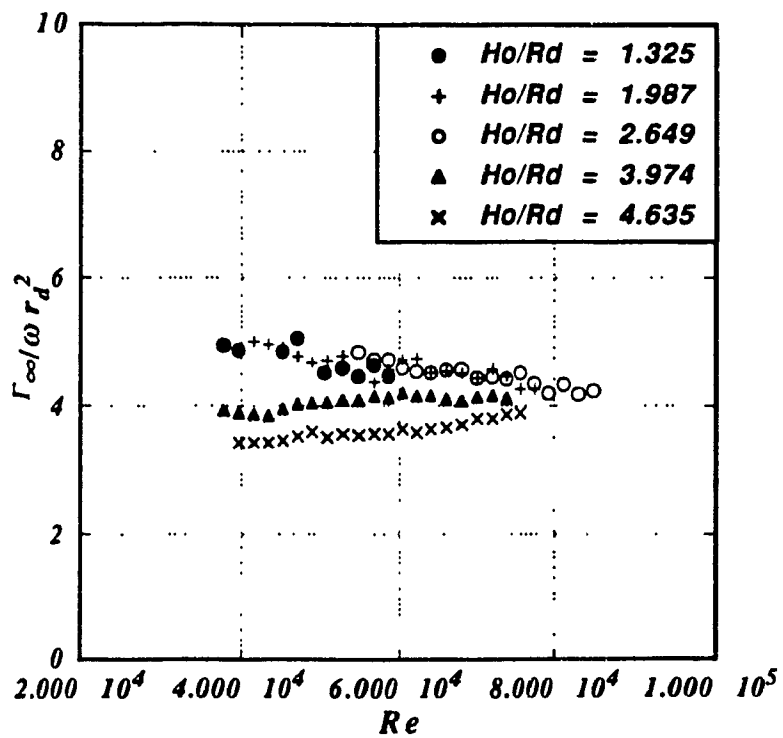
$$\frac{R_o}{R_d} = 0.80238 - 0.48351 \frac{R_d}{R_t}$$

Fig. 3.6. The linear dependence between the radii of a core and the cylindrical container.

The dependence of the vortex strength on the original height of the working liquid in the container is also evident from the experimental trials. According to fig. 3.7, the strength decreases as the values of the original height increases. This depicts the diminishing effects of viscous diffusion in larger systems (higher values of H_0).

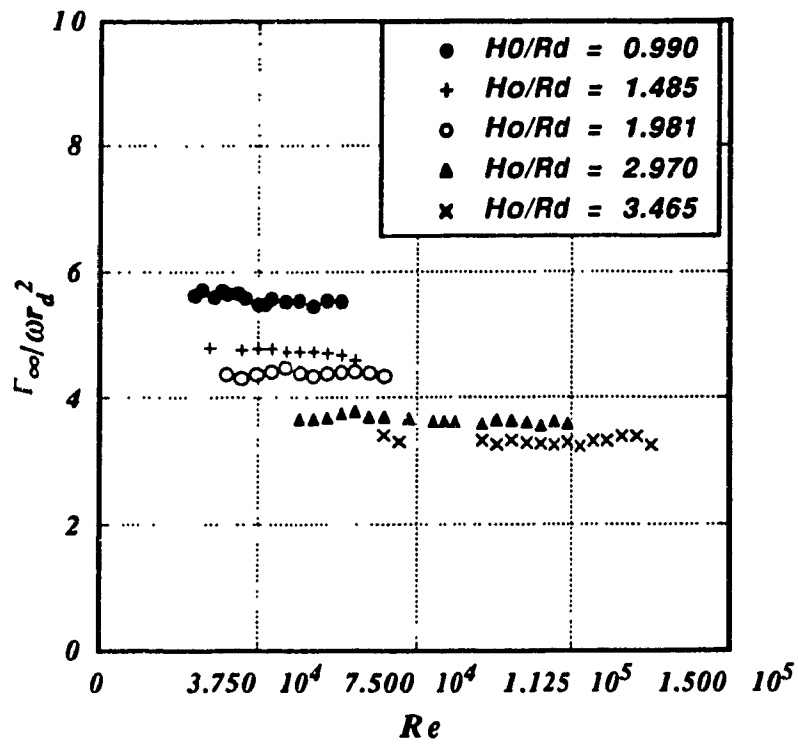


$D_d = 101.0$ mm (disk, working liquid: water)

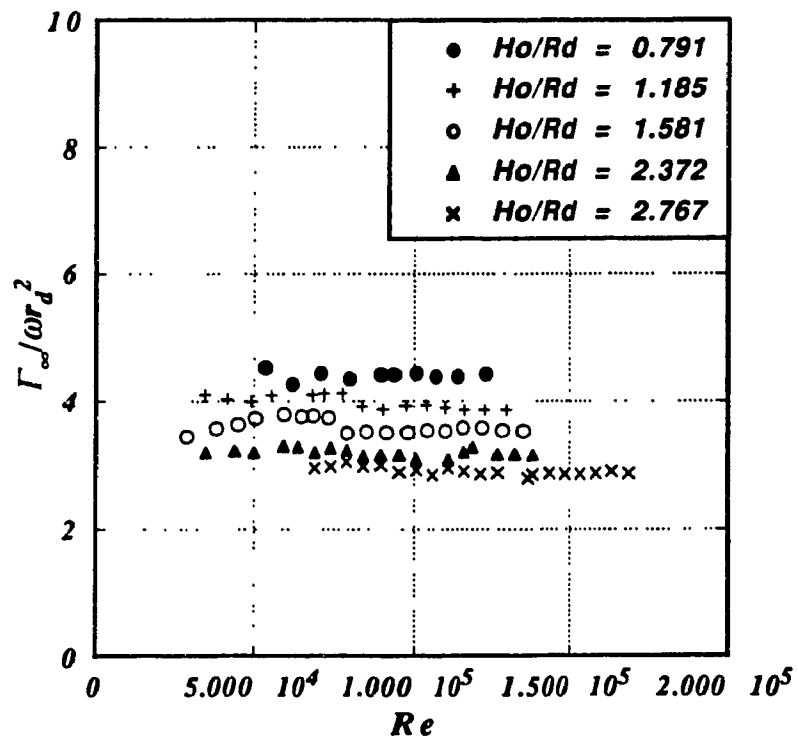


$D_d = 151.0$ mm (disk, working liquid: water)

Fig. 3.7.a. Relationship between the vortex strength and Re .

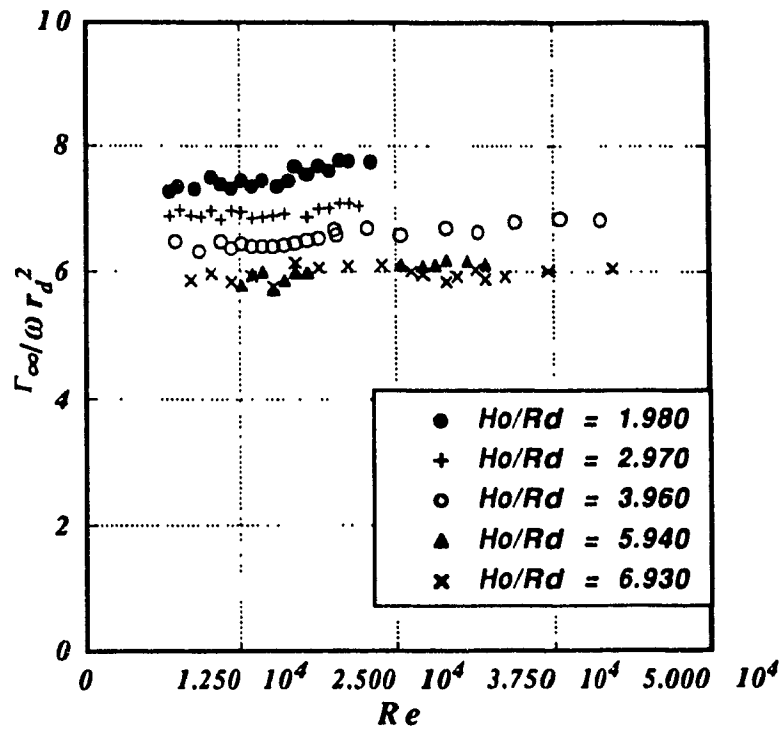


$D_d = 202.0$ mm (disk, working liquid: water)

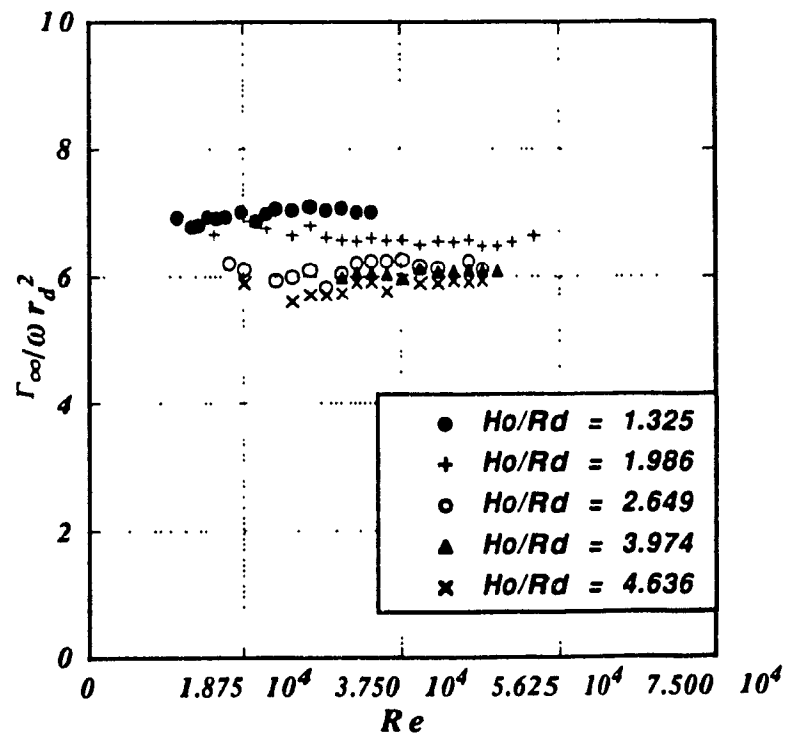


$D_d = 253.0$ mm (disk, working liquid: water)

Fig. 3.7.b. Relationship between the vortex strength and Re .

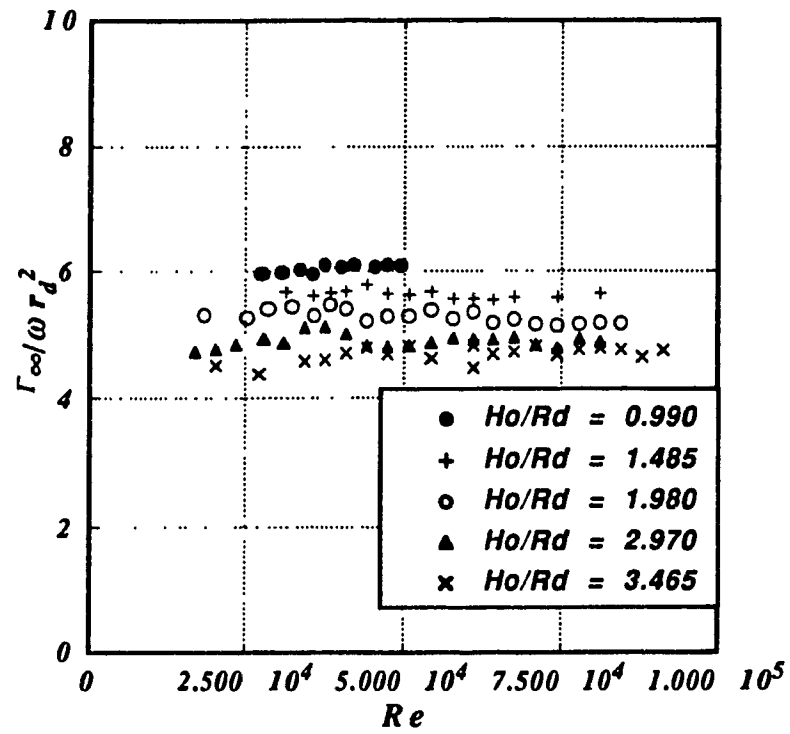


$D_d = 101.0 \text{ mm}$ (bar, working liquid: water)

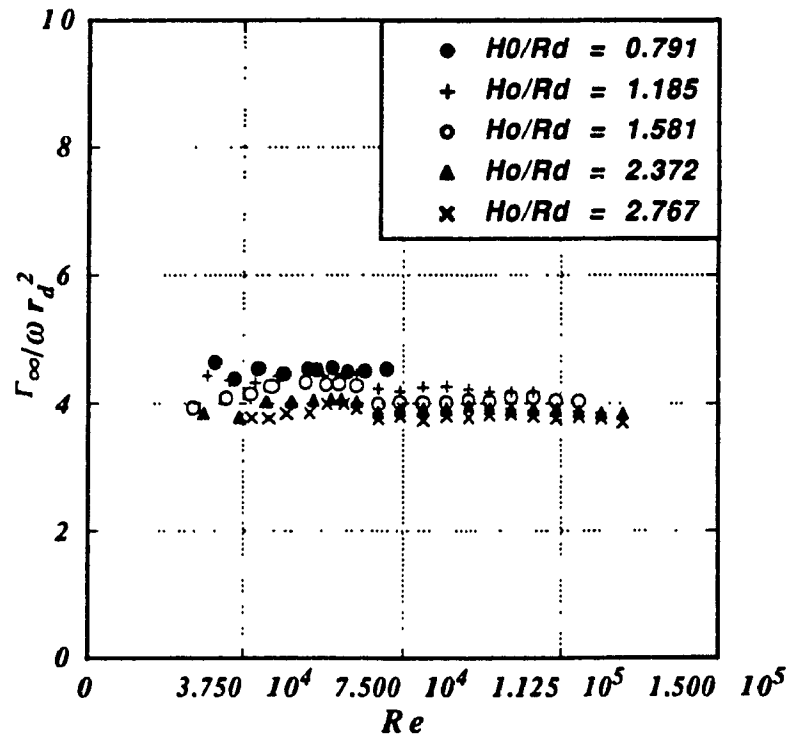


$D_d = 151.0 \text{ mm}$ (bar, working liquid: water)

Fig. 3.7.c. Relationship between the vortex strength and Re .

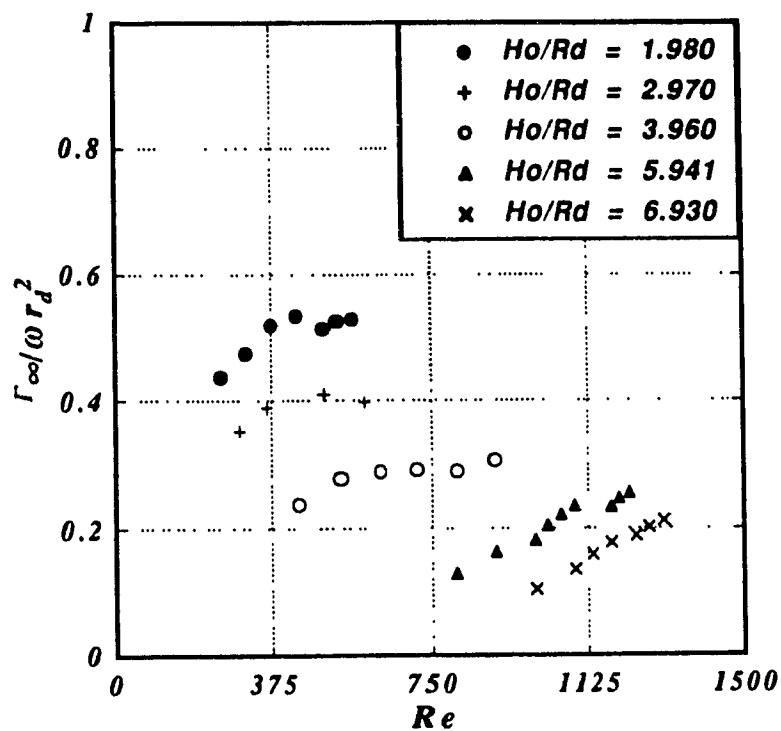


$D_d = 202.0 \text{ mm}$ (bar, working liquid: water)

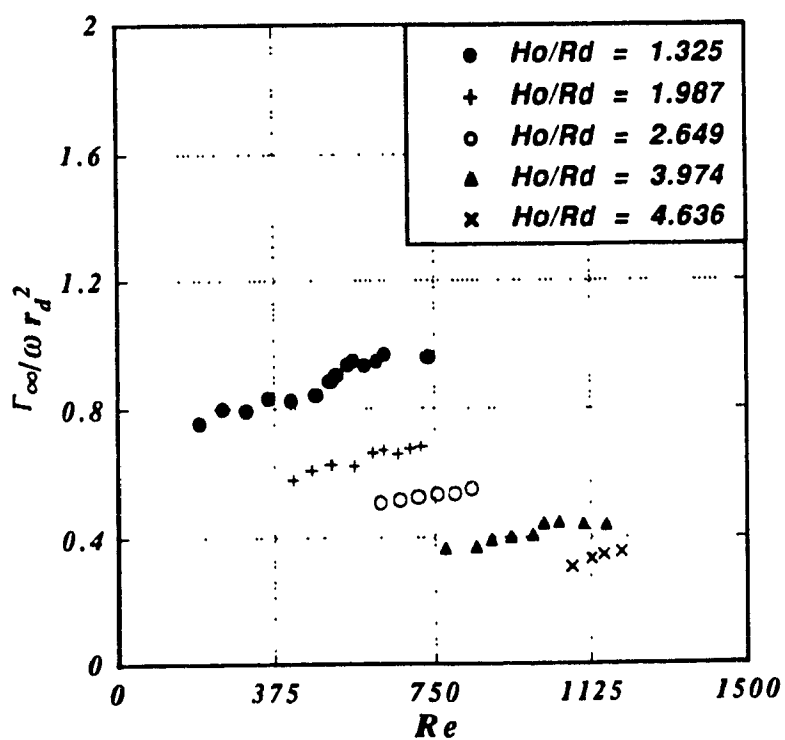


$D_d = 253.0 \text{ mm}$ (bar, working liquid: water)

Fig. 3.7.d. Relationship between the vortex strength and Re .

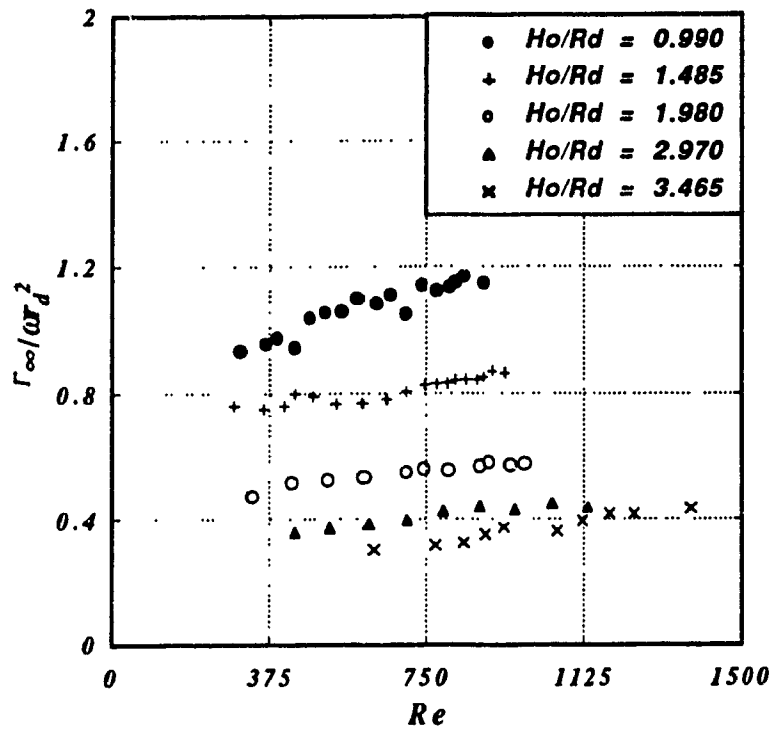


$D_d = 101.0 \text{ mm}$ (disk, working liquid: oil)

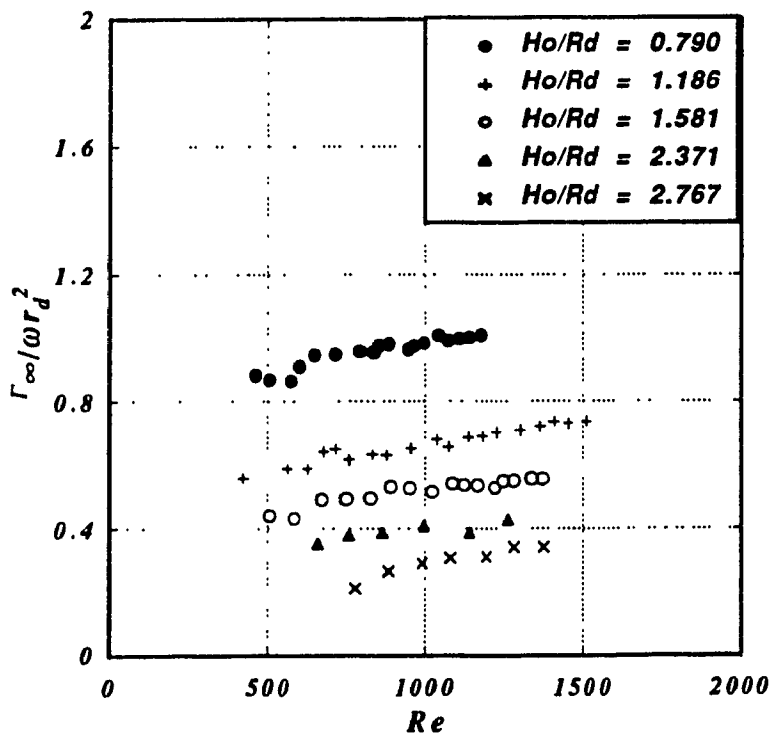


$D_d = 151.0 \text{ mm}$ (disk, working liquid: oil)

Fig. 3.7.e. Relationship between the vortex strength and Re .

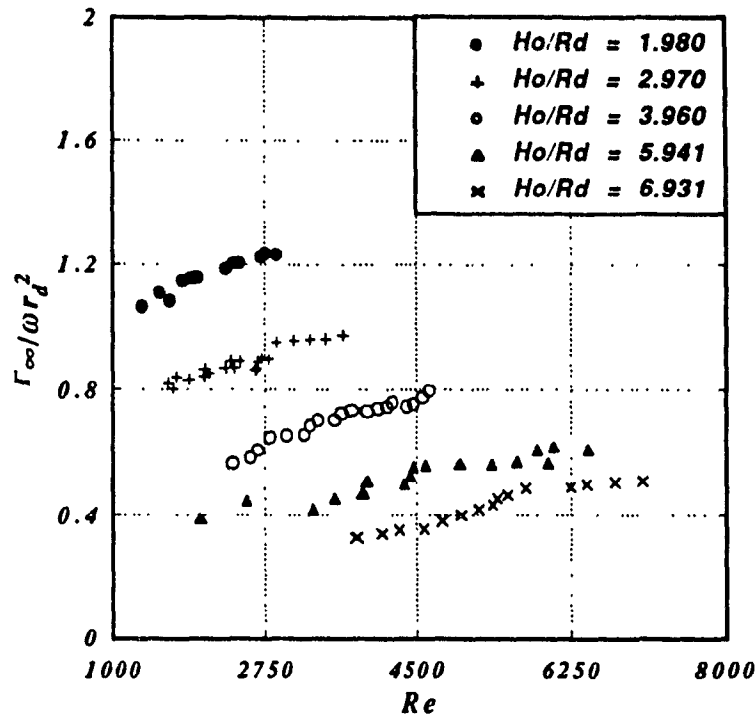


$D_d = 202.0 \text{ mm}$ (disk, working liquid: oil)

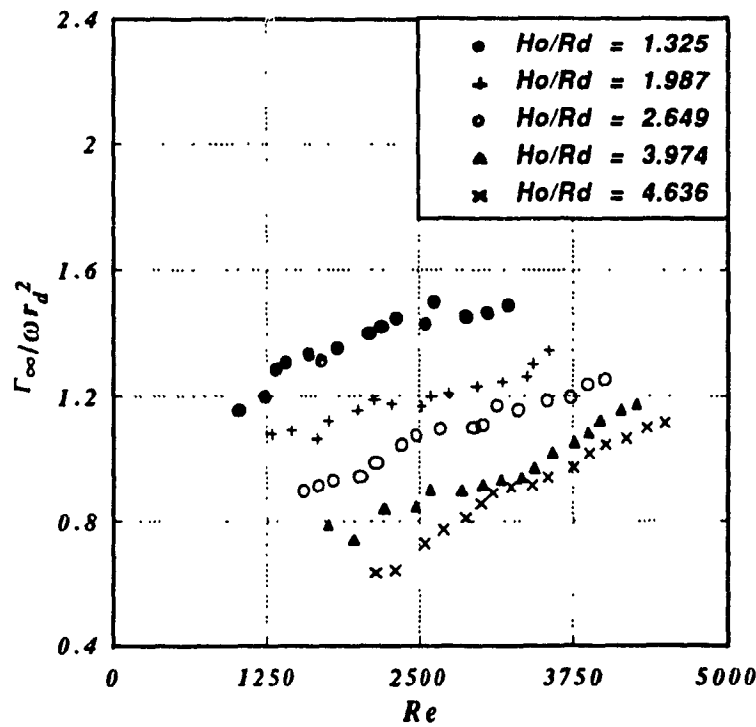


$D_d = 253.0 \text{ mm}$ (disk, working liquid: oil)

Fig. 3.7.f. Relationship between the vortex strength and Re .

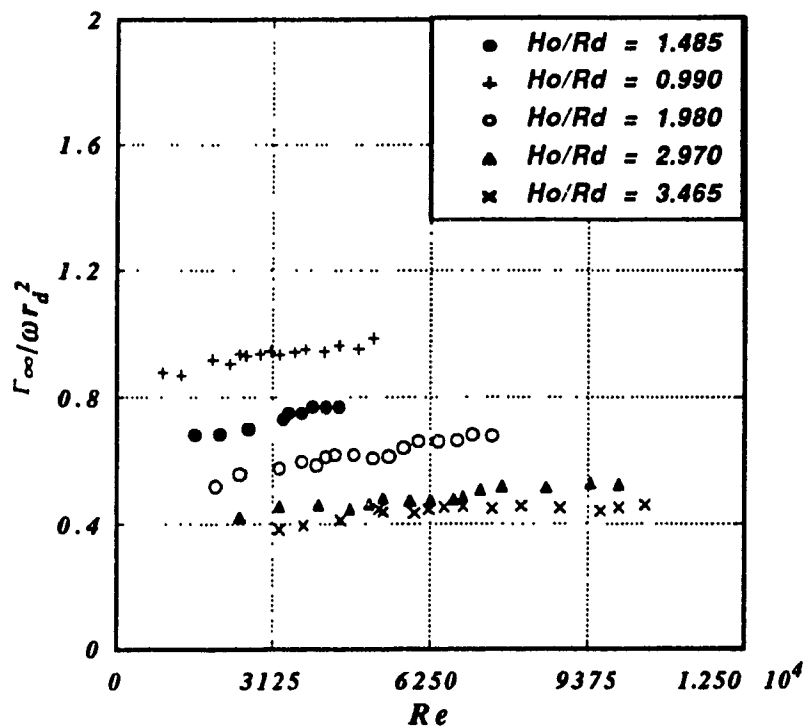


$D_d = 101.0$ mm (disk, working liquid: glycerol solution)

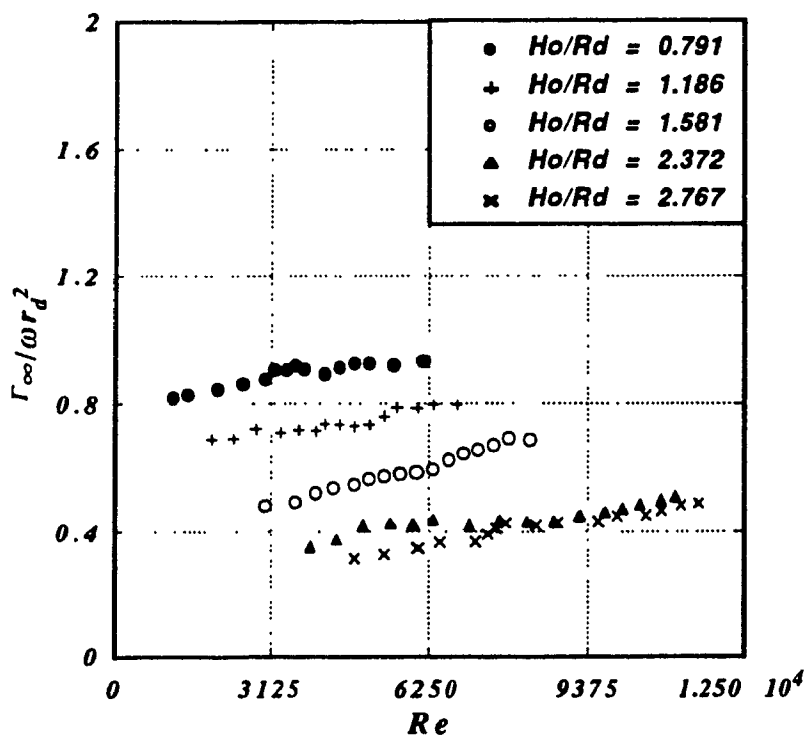


$D_d = 151.0$ mm (disk, working liquid: glycerol solution)

Fig. 3.7.g. Relationship between the vortex strength and Re .



$D_d = 202.0$ mm (disk, working liquid: glycerol solution)



$D_d = 253.0$ mm (disk, working liquid: glycerol solution)

Fig. 3.7.h. Relationship between the vortex strength and Re .

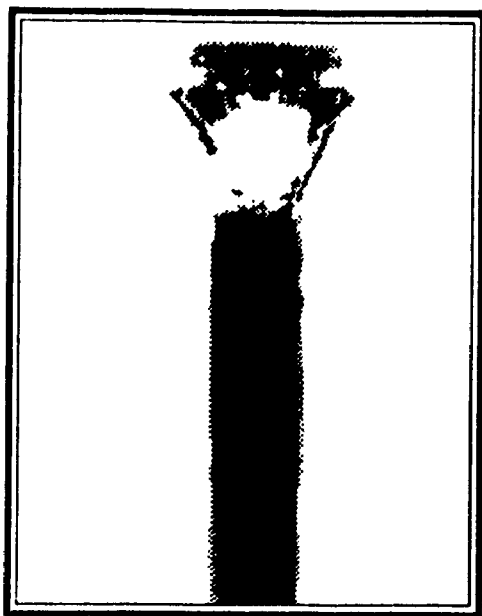
3.4 Wave Activity in the Core

During a detailed mapping of the steady free-surface profile as a function of the disk diameter, R_d , the original water level, h_0 , and the rotational speed of the disk, ω , several problems were encountered. All these were attributed to the dynamic nature of the core. For vortices with tall thin cores, the familiar axisymmetric and bending waves described by Maxworthy et al (1985), and Maxworthy (1988) forced the vortex center to precess about the geometric center of the containing vessel in the direction of the rotating stirrer, and to undulate.

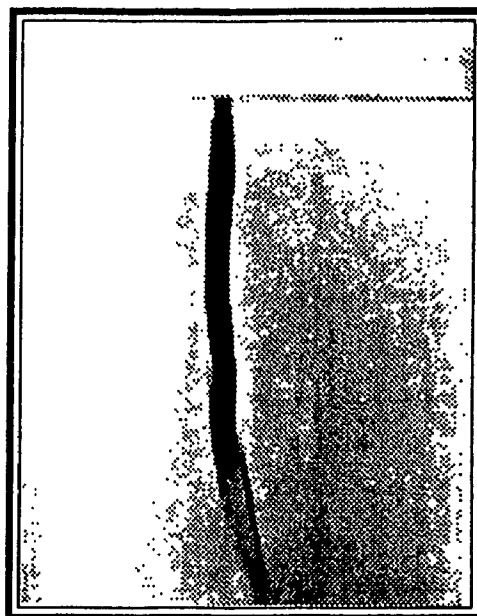
For the cases where vortices with relatively short, thick cores were produced; the flowfield was nearly free from the above mentioned problems. In the case of low disk velocities, the free-surface profile was smooth, see fig. 3.8.d. Increasing ω , harmonic disturbances manifested by the varicose undulations of the free-surface are evident from fig. 3.8.e and f emerged. If one superimposes Kelvin's (1880) harmonic perturbations of the core to the mean core radius, \bar{r}_s , the following relation is obtained,

$$\bar{r} = \bar{r}_s + \Re\{c e^{-i(mz + n\theta - \sigma t)}\} \quad (3.20)$$

where c is a constant, m, n are the wave numbers in the z and θ directions respectively and σ is the angular frequency. For $t = 0$ and $z = 0$ several equilibrium states are shown in fig. 3.9. These are very similar to the ones obtained experimentally by Vatistas (1990), and the core shapes obtained numerically solving the fully 3-d problem, see fig. 4.8. If the mean core \bar{r}_s in eq. (3.20) is allowed to be represented by eq. (2.24) then for $t = 0$, $m = 4$, $n = 2$ and $c = 0.065$,



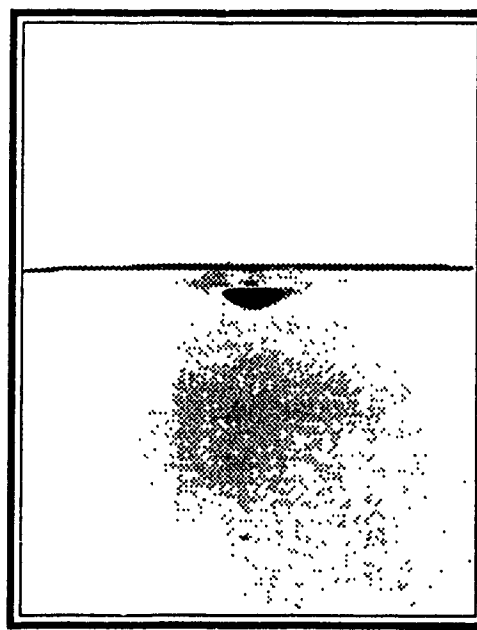
*(a) wave propagations
in axial direction.*



*(b) precession of a vortex
core.*

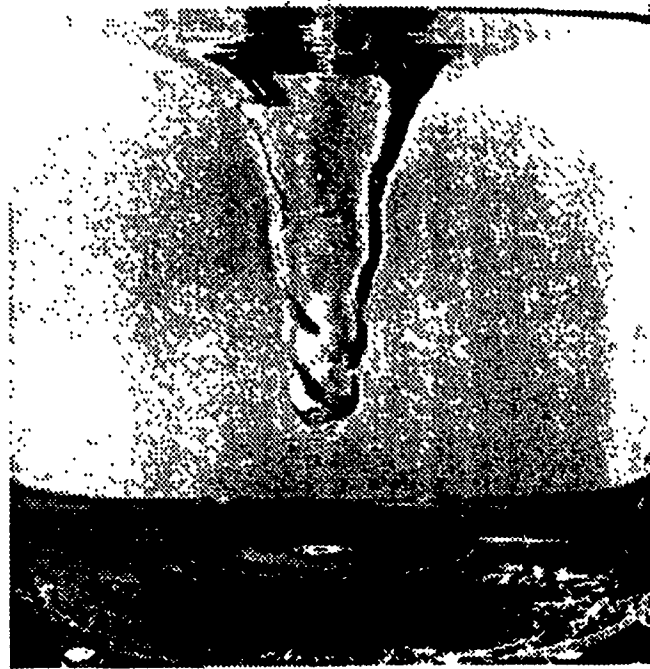


*(c) wave propagations in
axial direction.*



*(d) relatively undisturbed free
surface profile.*

Fig. 3.8. a - d. Oscillatory behavior of a vortex core.



(e)



(f)

Fig. 3.8.e & f. Oscillatory behavior of a vortex core - varicose core behavior.

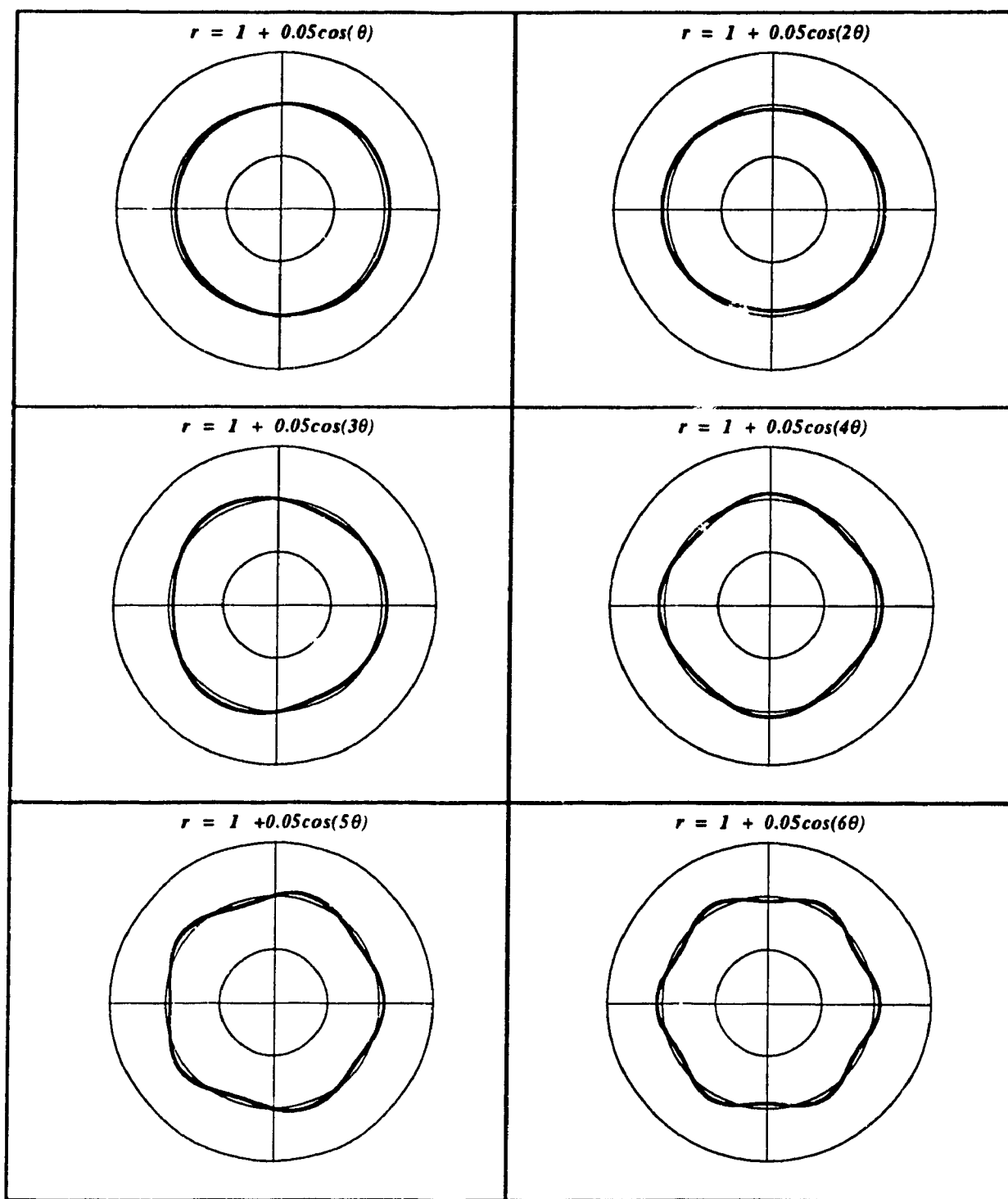


Fig. 3.9. Variation of equilibrium states, ($z = 0, t = 0$).

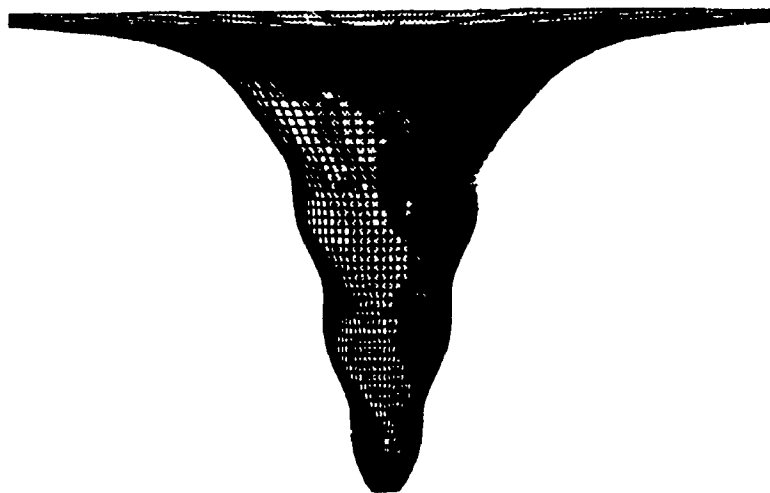
$$\bar{r} = \sqrt{\tan\left(\frac{z}{4}\right)} + 0.065 \cos (2\theta + 4z) \quad (3.21)$$

The results of the observed and theoretical (eq. (3.21)) free-surface profiles (frozen in time) are given in fig. 3.10. The similarity between the two is remarkable but not unexpected.



(a) Observed free surface profile.

$$\bar{r} = \sqrt{\tan \frac{Z}{4}} + 0.065 \cos (2\theta + 4z)$$



(b) Theoretically obtained free surface profile.

Fig. 3.10 Comparison of varicose core behavior.

4. Application of the New Vortex Model

4.1 Vortex Chamber

One of the main concerns in the design of vortex chambers is the pressure drop developed across the chamber. The task to develop formulations with the aim to effectively predict *a priori* the value of the latter parameter has been the subject of extensive research in the past (Lewellen (1971), Shakespeare et al (1980), Troyankin et al (1969) and Vatistas et al (1986)). Although Burgers' model approximates the tangential velocity better than Rankine's vortex, if used in the analysis presented by Vatistas et al (1989) to determine the pressure drop across the chamber, it will produce an equation which will require evaluation of exponential integrals.

The new vortex model is also applied to vortex chamber flows. The aim of the present exercise is to see whether the new tangential velocity distribution produces any substantial differences in the determination of the pressure drop using analogous to free-vortex assumptions employed by Vatistas (1986). Also, the implementation of the novel vortex model permits the elimination of additional complications which are the inevitable using Burgers' vortex model.

Consider the schematics of a typical vortex chamber, given on fig. 4.1. The integral form of the energy equation with neglected potential and viscous-dissipation energies is given by:

$$\int_s \left(P + \frac{1}{2} \rho q^2 \right) \vec{q} \cdot d\vec{S} = 0 \quad (4.1)$$

where, \vec{q} is a velocity vector, P is a static pressure, ρ is the density of a working substance and \vec{S} is the control-surface vector. Then, the energy balance across the vortex chamber yields

$$\int_{A_{out}} \left(P + \frac{1}{2} \rho q^2 \right) V_z dA = \int_{A_{in}} \left(P + \frac{1}{2} \rho q^2 \right) \vec{q} \cdot \vec{n} dA \quad (4.2)$$

Under the following assumptions,

- i. At the exit, the static pressure is constant and equal to the ambient, P_a .
- ii. The axial velocity at the exit is uniform and extends up to the core.
- iii. The radial velocity is neglected across the control volume.
- iv. The fluid is incompressible.
- v. At the inlet, there is no axial velocity and the other two velocity components are uniform.
- vi. The tangential velocity is given by eq. (2.23).

the pressure drop, $P_{in} - P_{out}$, is deduced from the energy equation, eq. (4.2):

$$P_{in} - P_{out} = P_{in} - P_a = \frac{\rho}{R_e^2 - R_o^2} \int_{R_o}^{R_e} \left(\frac{\Gamma_\infty}{2\pi} \right)^2 \frac{r^3}{R_o^4 - r^4} dr + \frac{\rho V_z^2}{R_e^2 - R_o^2} \int_{R_o}^{R_e} r dr - \frac{\rho}{2} q_{in}^2 \quad (4.3)$$

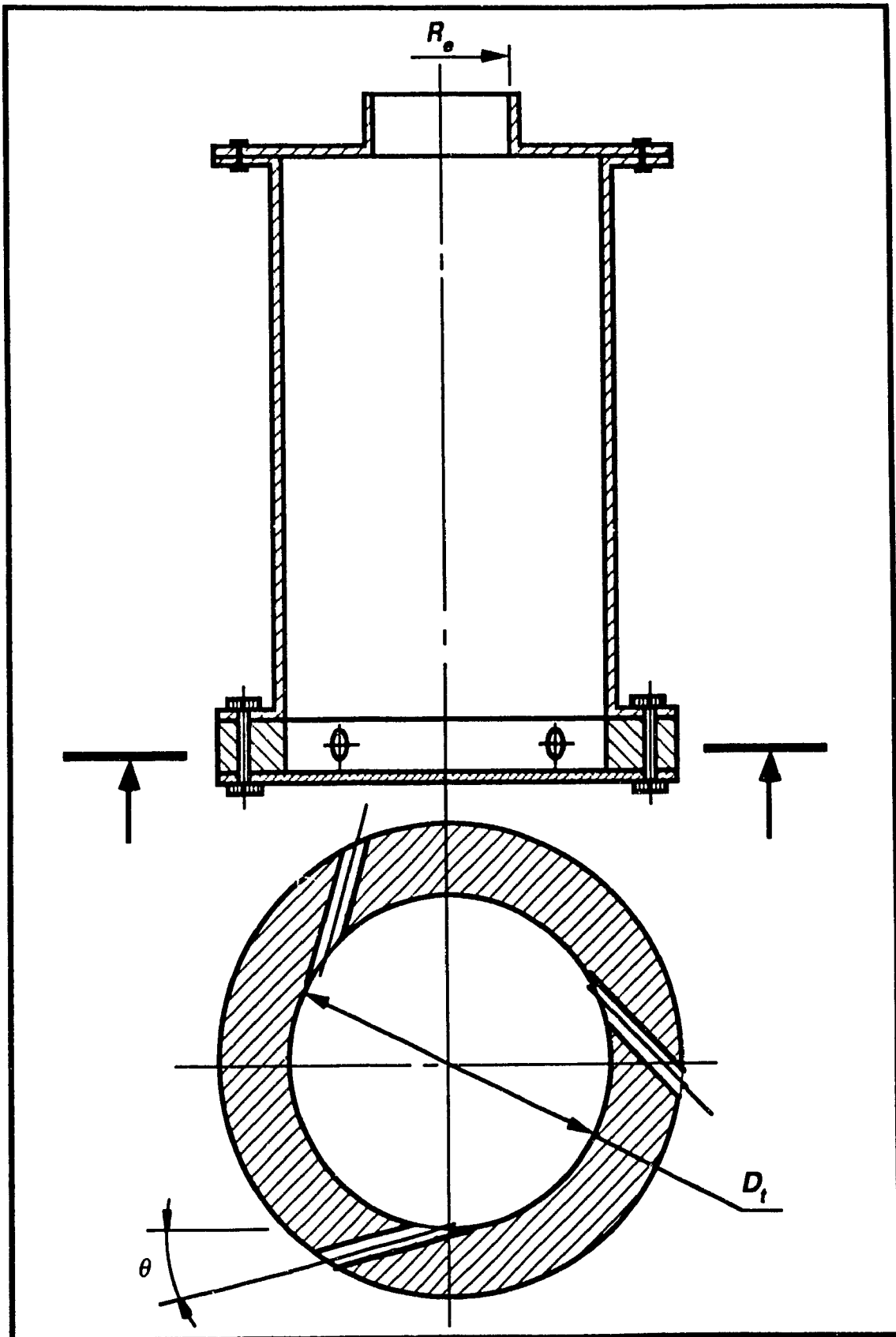


Fig. 4.1 Schematics of a vortex chamber.

Performing the integration and rearranging the terms, the above equation is represented in its dimensionless form expressing the dimensionless pressure drop in terms of the geometrical parameter β ,

$$\Delta\tilde{P} = \frac{\beta}{(1 - x_c^2)^2} + \frac{\ln\left(\frac{1}{2}(x_c^4 + 1) / x_c^4\right)}{2(1 - x_c^2)} \quad (4.4)$$

where, $x_c = R_o/R_e$, is a dimensionless representation of a core radius at the exit of a vortex chamber,

$$\Delta\tilde{P} = \left(\frac{2(P_{in} - P_a)}{\rho q_{in}^2} + 1 \right) \left(\frac{R_e/R_t}{\cos \theta} \right)^2 \quad \text{is the dimensionless form of the pressure drop,}$$

$$\beta = \left(\frac{A_{in}/A_t}{R_e/R_t \cos \theta} \right)^2 \quad \text{is the swirl parameter which is the inverse of swirl number often quoted in the technical literature, see Gupta et al (1984).}$$

According to Vatistas et al (1986) the core size may be obtained using the minimum principle which is mathematically expressed by,

$$\frac{\partial \Delta\tilde{P}}{\partial x_c} = 0;$$

Application of the above condition on eq. (4.4) yields,

$$2\beta - \frac{(1 - x_c^2)^2}{2x_c^2(1 + x_c^4)} - (1 - x_c^2) \ln \sqrt{\frac{1}{2} \left(1 - \frac{1}{x_c^4} \right)} = 0 \quad (4.5)$$

where a more detailed derivation of eq. (4.5) is provided in *Appendix B*.

The above equation is a non-linear algebraic equation which for a given value of β must be solved for x_c . The solution of the equation is obtained numerically using the Newton-Raphson method. The graphical solution of eq. (4.5) is given in fig. 4.2. It can be seen that the present theory and that of Vatistas (1989) give almost identical results. Eq. (4.5), also agrees well the experimental results by Shakespeare et al (1980) for the region when geometric parameter, β , is less than 10. Since β is inversely proportional to the swirl number the relative strength of the vortex becomes less as β increases. For large values of β there is a substantial deviation of present results from the experimental results. The latter indicates that the present analysis can successfully predict the cores of strong vortices.

Alternatively, combining eq. (4.5) and eq. (4.4), one can relate the minimum pressure drop to the dimensionless core radius x_c and the geometric parameter, β independently:

$$\Delta \tilde{P} = \frac{\beta}{\xi(\beta)} + \zeta(\beta) \quad (4.6)$$

and

$$\Delta \tilde{P} = \frac{\eta(x_c)}{(1 - x_c^2)^2} + \frac{\ln \left\{ \frac{1}{2} (x_c^4 + 1) / x_c^4 \right\}}{2(1 - x_c^2)} \quad (4.7)$$

where, $\eta(x_c)$, $\zeta(\beta)$ and $\xi(\beta)$ are the parametric functions which reflect the functional dependence between x_c and β , eq. (4.5) and fig. 4.2. Both eq. (4.6) and eq. (4.7) are represented graphically in figs. 4.3 and 4.4. Similar to fig. 4.2, the obtained analytical results demonstrate an analogous functional

dependence of the dependent and the independent variables with the analytical results of Vatistas (1989). There are, however, a difference among the results in the region of small β values. The difference can be attributed to the fact that the tangential velocity profile of the Rankine-like model employed by Vatistas (1989) deviates considerably from the actual profile in the neighborhood of the vortex core.

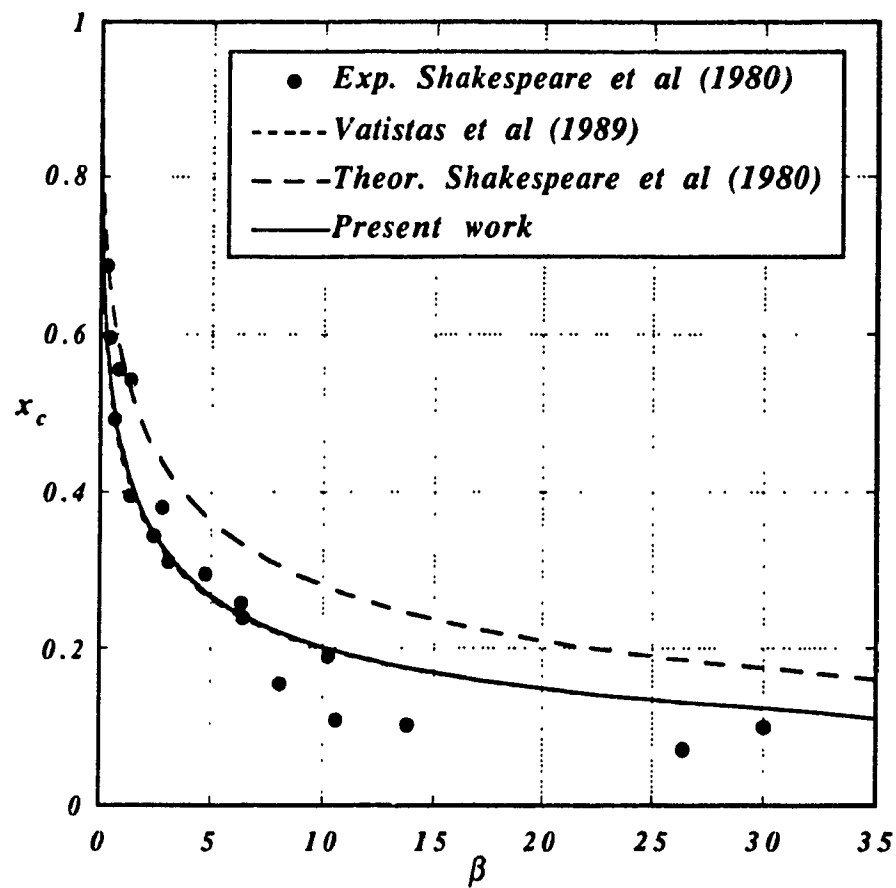


Fig. 4.2. The exit core as a function of geometric parameter, β .

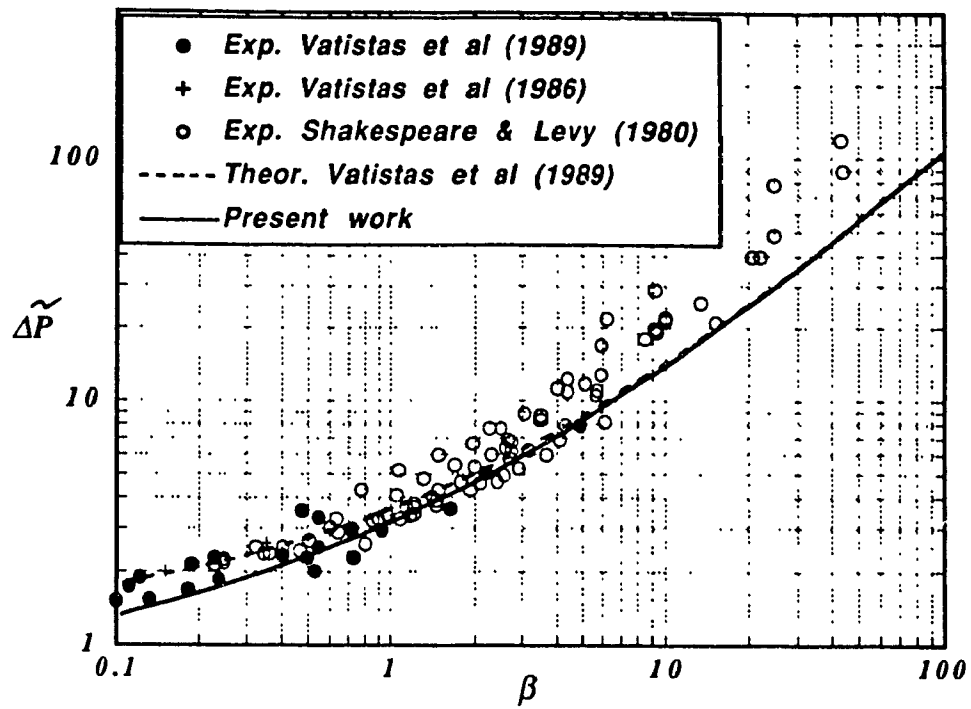


Fig. 4.3. Dimensionless pressure drop v.s. geometric parameter, β .

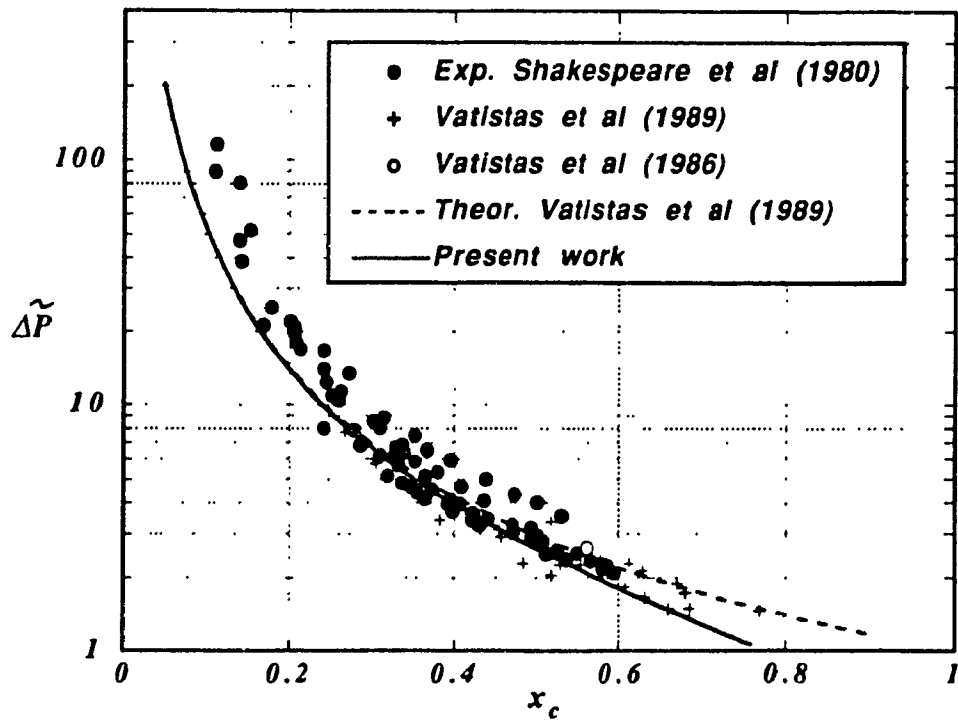


Fig. 4.4. Dimensionless pressure drop v.s. exit core.

According to fig. 4.4, the dimensionless form of the pressure drop might become less than one, indicating that the actual pressure drop is negative. Since such an outcome is physically not possible a condition to restrict the application of the theory must be given. This is,

$$1 \leq \left(\frac{\cos \theta}{R_e/R_t} \right)^2 \Delta \tilde{P} \quad (4.8)$$

If Eq. (4.8) is expressed in a form where the swirl angle, θ , is the dependent variable, the following condition restricting the value of θ is obtained,

$$\theta = \cos^{-1} \left(\frac{R_e/R_t}{\sqrt{\Delta \tilde{P}}} \right) = \cos^{-1} \left(\frac{R_e/R_t}{\sqrt{\frac{\beta}{\xi(\beta)} + \zeta(\beta)}} \right) \quad (4.9)$$

The results of eq. (4.9) are represented graphically in fig. 4.5

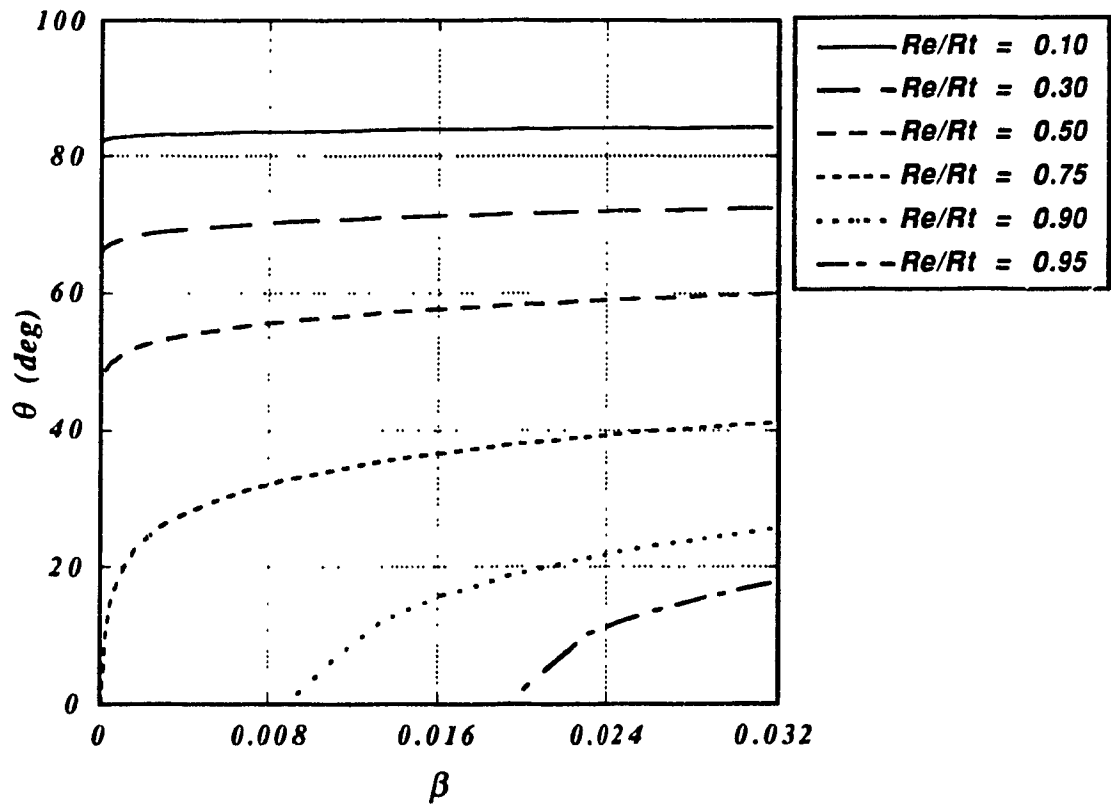


Fig. 4.5. Swirl angle as a function of geometric parameter, β and the aspect ratio, R_e/R_t .

4.2 Concentration of a Fine Sediment Particle

Another application which was selected to apply the new model deals with fine particle concentrations in a liquid vortex. Experimental as well as theoretical investigations were first performed by Julien (1985 and 1986). Burgers' model was applied by Vatistas (1989) to analyze the same problem.

Consider a fine spherical sediment particle of a density, ρ_p and diameter, d_p . Under the influence of the centrifugal force which is balanced by the pressure force, the drag force and the inertia force, the particle swirls outwards of the vortex center with a velocity, V_p . Since the present analysis is focused on particles of small diameter, the velocity of the particle does not substantially differ from the velocity of the rotating fluid which make the Coriolis force negligible compared to other forces acting on the particle. Thus, the radial velocity of the particles, V_p' , can be determined by the balance of the prevalent forces:

$$m_p a_r = F_c - F_p - F_v \quad (4.10)$$

where the three forces on the right hand side of the above equation are centrifugal, pressure and the radial component of the viscous force respectively, and m_p is the mass of the particle, $\pi \rho_p d_p^3 / 6$, a_r is the radial acceleration of the particle. From eq. (2.2.a), the centrifugal and pressure forces are

$$F_c = \frac{\pi}{6} \rho_p d_p^3 \frac{V_t^2}{r} \quad (4.11)$$

$$F_p = \frac{\pi}{6} \rho d_p^3 \frac{V_\theta^2}{r} \quad (4.12)$$

respectively, where V_t is the tangential velocity of the particle. According to Stoke's drag law, the radial component of viscous force acting on the particle is

$$F_v = 3\pi\rho\nu V_p' d_p \quad (4.13)$$

Combining these prevalent forces and dividing eq. (4.10) by the mass of the particle, one can obtain an expression of the radial acceleration:

$$a_r = \frac{V_t^2}{r} - \frac{\rho}{\rho_p} \frac{V_\theta^2}{r} - 18 \frac{\rho}{\rho_p} \frac{V_p'}{d_p^2} \quad (4.14)$$

The radial acceleration of the particle vanishes as the velocity of the particle approaches the velocity of the fluid. Since the values of the two are very close, the radial acceleration assumed to be negligible. Thus, from eq. (4.14), the radial component of velocity of the particle is:

$$V_p' = \frac{1}{18\nu} \left(\frac{\rho_p}{\rho} - 1 \right) \frac{d_p^2}{r} \frac{V_\theta^2}{r} \quad (4.15)$$

If the new formula of tangential velocity given by eq. (2.24) is implemented into eq. (4.15),

$$V_p' = \frac{1}{72\nu r_o} \left(\frac{\rho_p}{\rho} - 1 \right) \left(\frac{d_p}{r_o} \right)^2 \frac{\Gamma_\infty^2}{\pi^2} \frac{\bar{r}}{1 + \bar{r}^4} \quad (4.16)$$

Under the equilibrium conditions, namely, when the centrifugal force on a particle is balanced by the diffusion flux, the concentration of a particle is governed by a linear differential equation,

$$\epsilon \frac{dC}{C} = V_p' dr \quad (4.17.a)$$

where, C is a sediment concentration of a particle, ϵ is a particle diffusion coefficient. Substitution of eq. (4.16) into (4.17.a) yields,

$$\epsilon \frac{dC}{C} = \frac{1}{72\nu} \left(\frac{\rho_p}{\rho} - 1 \right) \left(\frac{d_p}{r_o} \right)^2 \frac{\Gamma_\infty^2}{\pi^2} \frac{\bar{r}}{1 + \bar{r}^4} d\bar{r} \quad (4.17.b)$$

Integrating eq. (4.17.b) from \bar{r} to ∞ gives the following expression,

$$-\frac{1}{a} \ln(C/C_\infty) = \frac{\pi}{2} - \arctan(\bar{r}^2) \quad (4.18)$$

where, C_∞ is the sediment concentration of a particle far from the center of rotation and

$$a = \frac{1}{144\nu\epsilon} \left(\frac{\rho_p}{\rho} - 1 \right) \left(\frac{d_p}{r_o} \right)^2 \left(\frac{\Gamma_\infty}{\pi} \right)^2$$

The graphical representation of eq. (4.18) given in fig. 4.6 demonstrates the validity of the above analysis; eq. (4.18) confirms the experimental results obtained by Julient (1985) and (1986). Although there is a difference in the neighborhood of the center of the core, between eq. (4.18) and the results obtained using Burgers' vortex model, (Vatistas (1989)), the difference is rapidly converging to zero as r increases. While both methods predict reality

equally well, eq. (4.18) is considerably simpler by comparison to the equation derived by Vatistas (1989).

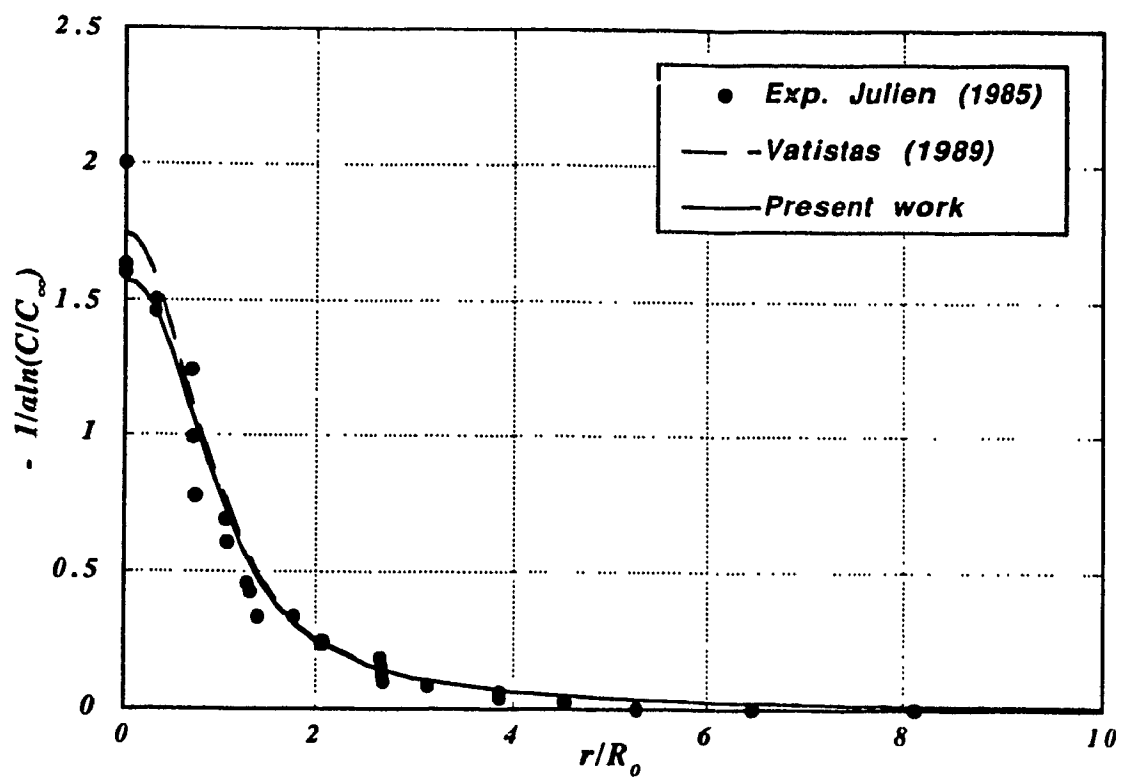


Fig. 4.6. Concentration of a fine sediment particle.

5. Numerical Simulation

One of the main objectives of conducting a numerical analysis is to validate the hypothesis that the profound wave activity which was observed experimentally is indeed prevailed by the governing equations of motion. Moreover, a detailed mapping of the flowfield at the fixed time frame permits the rigorous assessment of the secondary flow formation. In the future, the developed scheme will enable one to construct the solution manifold of the problem under consideration.

A number of flow situations have been successfully solved in the past by the incorporation of appropriate assumptions to bring the governing equations to a form amenable to mathematical treatment. The majority of the problems however, require the solution of the complete set of Navier-Stokes equations. Since such a rigorous theoretical flow characterization is not possible, an approximate solution through the application of numerical methods is at the present the only alternative.

In this section numerical solutions for the agitator problem are obtained. The aim here is (a) to obtain the secondary flow structure, (b) to present the evolution of the flow in time, and (c) to demonstrate that the experimentally observed wave activity of the core is present in the solutions of the Navier-Stokes equations. In order to simulate the 3-d problem with an interface and a moving boundary, an existing algorithm the SOLA-VOF (2-d algorithm) was

extended to fully 3-d. A novel approach for boundary condition implementation at the geometrical center of the domain was developed. Many investigators advocate that the numerical solution using the conservative form of the equations might be more appropriate. However, for the problem under consideration and in a variety of other situations, numerical experiments have shown that this is not the case. Under certain conditions if the same problem is solved using the two different formulations, the one where the governing equations are in conservative form will be unstable. The cumulative effects of the parasitic divergence term will contaminate the results and provoke numerical instability.

5.1 Governing Equations

Consider the agitator problem as it was introduced previously. The fluid motion taking place inside the flow domain are governed by the fully 3-d, transient, incompressible momentum equations in cylindrical coordinates with constant viscosity. These are,

mass continuity

$$\frac{\partial u}{\partial x} + \frac{1}{x} \frac{\partial w}{\partial z} + \frac{\partial v}{\partial y} + \frac{u}{x} = 0 \quad (5.1)$$

x-momentum

$$\frac{Du}{Dt} - \frac{w^2}{x} = -\frac{\partial \bar{P}}{\partial x} + \nu \left(\nabla^2 u - \frac{u}{x^2} - \frac{2}{x^2} \frac{\partial w}{\partial z} \right) \quad (5.2.a)$$

y-momentum

$$\frac{Dv}{Dt} = g_y - \frac{\partial \bar{P}}{\partial y} + \nu \nabla^2 v \quad (5.2.b)$$

z-momentum

$$\frac{Dw}{Dt} + \frac{uw}{x} = -\frac{1}{x} \frac{\partial \bar{P}}{\partial y} + \nu \left(\nabla^2 v + \frac{2}{x^2} \frac{\partial u}{\partial z} - \frac{w}{x^2} \right) \quad (5.2.c)$$

where,

$$\frac{D}{Dt} = \frac{\partial}{\partial t} + u \frac{\partial}{\partial x} + v \frac{\partial}{\partial y} + \frac{1}{x} \frac{\partial}{\partial z}$$

and

$$\nabla^2 = \frac{\partial^2}{\partial x^2} + \frac{1}{x} \frac{\partial}{\partial x} + \frac{\partial^2}{\partial y^2} + \frac{1}{x^2} \frac{\partial^2}{\partial z^2}.$$

Here, x represents a radial, y - axial, z - tangential directions of a fixed cylindrical coordinate system; u, v, w are the velocity components of corresponding axis - x, y, z , respectively; g_y is the y -component of the body acceleration, ν is the kinematic viscosity of working substance.

The exceedingly non-linear character of the above equations excludes the possibility of employing linearized theory which is limited to the assumption of small amplitude. This is the inevitable characteristic of Navier-Stokes equations. In a view of discretization of governing equations, the aim is to minimize the degree of non-linearity. The existing methods of discretization recommend the representation of the equations in conservative (divergence) form for further discretization which allows to insure the conservation of both continuity and momentum in a finite difference domain. However, in the practical sense, it is impossible to accomplish it simultaneously, unless mass continuity was previously satisfied. Since continuity, of course in the numerical sense, is not fully satisfied due to truncated and round-off errors, etc., this leads to an argument that the conservative representation of momentum equations is not always an appropriate form. As a result, it contributes an additional error in momentum equations and occasionally may lead to unstable results.

Consider the convective terms of eq. (5.2.a) which can be written in conservative form as

$$\frac{\partial u}{\partial t} + \frac{\partial u^2}{\partial x} + \frac{\partial uv}{\partial y} + \frac{1}{x} \frac{\partial uw}{\partial z} - u \left(\frac{\partial u}{\partial x} + \frac{1}{x} \frac{\partial w}{\partial z} + \frac{\partial v}{\partial y} \right) - \frac{w^2}{x} \quad (5.3)$$

the terms in brackets are defined as momentum flux and equal to

$$\frac{\partial u}{\partial x} + \frac{1}{x} \frac{\partial w}{\partial z} + \frac{\partial v}{\partial y} = - \frac{u}{x} \quad (5.4)$$

from continuity equation. The present scheme employs an iterating technique based on SOLA-VOF by extensive application of continuity equation which must rather be written as

$$\frac{\partial u}{\partial x} + \frac{1}{x} \frac{\partial w}{\partial z} + \frac{\partial v}{\partial y} + \frac{u}{x} = D \quad (5.5)$$

where, D (divergence) is a tolerance parameter which certainly is not equal to zero. Hence, the conservative form of the convective term acquired an extra parasite parameter D:

$$\frac{\partial u}{\partial t} + \frac{\partial u^2}{\partial x} + \frac{\partial uv}{\partial y} + \frac{1}{x} \frac{\partial uw}{\partial z} - u \left(D - \frac{u}{x} \right) - \frac{w^2}{x} \quad (5.6)$$

Typical values of the divergence typically range from 10^{-3} to 10^{-6} depending on the required accuracy and hardware capabilities. For short term computations, the presence of non-zero divergence may not be as crucial as for lengthy, time-consuming problems. As the number of computer operations increases, the growth of mass deficiency reaches a point at which the accumulated error is becoming significant and may even reach the order

of magnitude of the convective or the viscous terms. Inevitably, this leads to falsified results or, even worse, to numerical instability.

The finite difference method employed here, uses the forward-time, centered-space difference scheme to discretize the governing equations. As it was mentioned previously, special attention must be attributed to the non-linear terms of the convective part of governing equations; namely, the upstream-differencing must be employed to retain the stability requirements.

Thus, the governing equations in finite difference form are given by,

x-momentum

$$U_{i,j,k}^{n+1} = U_{i,j,k}^n + \Delta t \left(\frac{1}{\Delta x} (P_{i-1,j,k} - P_{i,j,k}) - FUX - FUY - FUZ + FUC + v^*VISCX \right)^n \quad (5.7.a)$$

y-momentum

$$V_{i,j,k}^{n+1} = V_{i,j,k}^n + \Delta t \left(\frac{1}{\Delta y} (P_{i,j-1,k} - P_{i,j,k}) - FVX - FVY - FVZ + v^*VISCY \right)^n \quad (5.7.b)$$

z-momentum

$$W_{i,j,k}^{n+1} = W_{i,j,k}^n + \Delta t \left(\frac{1}{x\Delta z} (P_{i,j,k-1} - P_{i,j,k}) - FWX - FWY - FWZ - FWC + v^*VISCZ \right)^n \quad (5.7.c)$$

where i, j, k are spatial indexes, n is a time level, $FUX, FUY, FUZ, FUC, FVX, FVY, FVZ, FVC, FWX, FWY, FWZ, FWC$, are the convective members and

VISCX, VISCY, VISCZ are the viscous fluxes (for detailed description of the above terms see Appendix C)

The grid configuration used is shown in fig. 5.1. The location of dependent variables, U , V , W and P can be seen from a magnified cell given in the same figure. The pressure is located at the center of the cell whereas radial, axial and azimuthal velocities are located on the sides of the computational cell which signifies that the dependent variables are placed in a staggered fashion. A staggered grid greatly simplifies an application of boundary conditions; moreover, it assures the principle of continuity and momentum equations associated primarily with the influxes and outfluxes of mass and momentum. In particular, the net convection (the influxes and outfluxes of momentum) through a computational cell is becoming more predominant than other terms of the governing equations as Re increases. This is a crucial aspect as far as numerical instability is concerned, especially, when the finite-difference discretization is implemented. In order to facilitate the application of boundary conditions, the computational grid field is surrounded by a layer of fictitious cells. For instance, if the flow field viewed in a radial-axial plane, the tangential velocity is not laying right on a solid boundary and it is therefore required that the value of the velocity on the adjacent fictitious cell to be adjusted to the corresponding value of the tangential velocity of the solid boundary.

The location of each and every cell in the computational domain is denoted by index, i , j , k . For this particular problem, 20 cells in radial, 20 cells in axial and 18 cells in azimuthal directions were chosen. The choice of a grid configuration as well as spatial increments of three mutually perpendicular

axis, Δx , Δy , Δz depends on the geometry of a given problem, numerical stability criteria and the computer hardware which includes real-time operational speed or central processing unit (CPU) time as well as memory storage capacity.

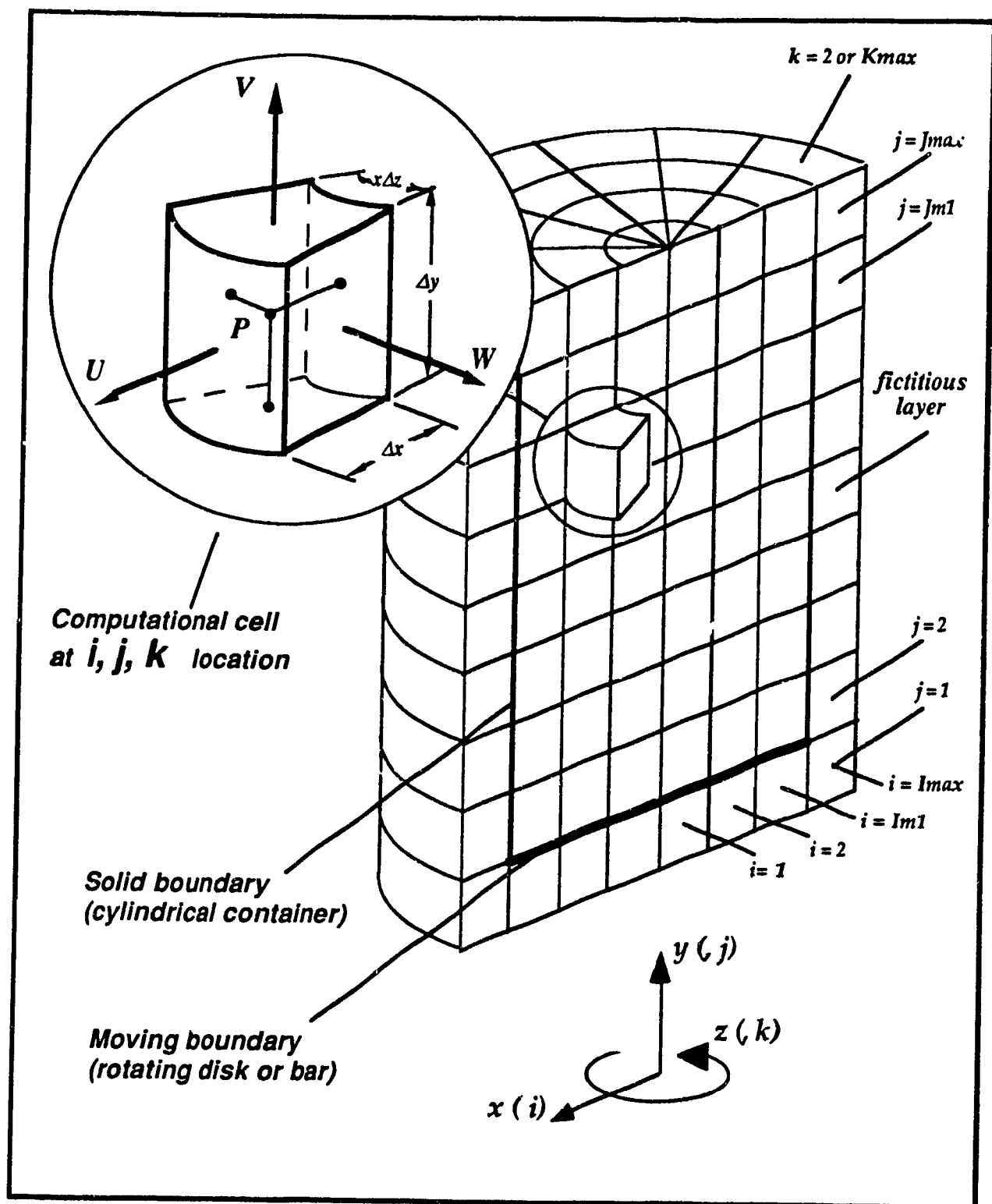


Fig. 5.1. General mesh arrangement.

5.2 Truncated Error Analysis

Errors arising due to the truncated terms influences greatly the stability criteria of every numerical algorithm. Attempts to solve partial differential equations in the past were often not successful. The oscillatory diverging nature of the error frequently contaminates the discretized equations causing violations of numerous natural laws. For instance, negative diffusion is the main contribution to the error which ultimately violates the second law of thermodynamics. In order to minimize the error, appropriate restrictions which ensures stability must be implemented.

At first, the analysis is to be focused on the general behavior of truncated error as a result of dependent variable discretization using Taylor series expansion where low-order terms must represent the discretized governing differential equations, and all high-order terms are to be considered as a truncated error. Such an approach gives a better chance to distinguish the discretized equations which include the high-order terms, from those which are actually to be solved by the means of finite-difference technique. The latter depicts that equations which exclude the truncated error are rather a hybrid of the actual governing equations and in most cases, fail to portray the nature of the governing equations.

The von Neuman-Fourier error analysis is frequently defined as a rigorous one; it allows the assessment of the nature of error growth whether it is oscillating, diverging or a combination of both; as a result, it assists in obtaining the means to minimize its presence and, ultimately, establish the stability criteria. The analysis is well suited for linear equations, but not

applicable to the equations of a non-linear nature. Since discretized equations are represented by a set of algebraic equations, the expression for the truncation error must be, as well, accompanied by an algebraic expression. Moreover, the method requires an explicit form of the errors in order to assign the limiting values of its amplitude. Because most the non-linear equations can not be expressed in an explicit form, the Von Neuman-Fourier analysis can not be applied.

The following example may demonstrate the substance of the above argument. Consider the non-linear parabolic (in time) partial differential equation:

$$\frac{\partial \vartheta}{\partial t} + \vartheta \frac{\partial \vartheta}{\partial x} = v \frac{\partial^2 \vartheta}{\partial x^2} \quad (5.8)$$

which represents a 1-d transport equation in Cartesian coordinate system with constant diffusion coefficient, v , and $\vartheta(x,t)$ is a velocity component. Defining the error by a finite Fourier series one gets,

$$E = e^{ib_k p \Delta x} e^{\alpha n \Delta t} = G^n e^{i\beta_k p \Delta x} \quad (5.9)$$

where, G^n - amplification factor at time level, n ($n = 0, 1, 2, \dots \infty$)

i - complex operator

β_k - arbitrary constant

p, k - integers

Δx - spatial increment

Discretization of eq. (5.8) using forward difference for the time derivative and central difference for space derivatives yields,

$$\vartheta_i^{n+1} - \vartheta_i^n = -\frac{\Delta t}{2\Delta x} \vartheta_i^n (\vartheta_{i+1}^n - \vartheta_{i-1}^n) + \frac{v\Delta t}{2} (\vartheta_{i+1}^n + \vartheta_{i-1}^n - 2\vartheta_i^n) \quad (5.10)$$

$$G + G^n \frac{\Delta t}{\Delta x} e^{i\beta_k p \Delta x} i \sin(\beta_k \Delta x) = \frac{2v\Delta t}{2} (\cos(\beta_k \Delta x) - 1) \quad (5.11)$$

Eq. (5.11) is an implicit, non-linear algebraic equation, and an analytical solution is not available. Thus showing clearly the inadequacy of the Von Neuman-Fourier truncation error analysis. One can, however, approximate the error by linearizing the governing equations. This may be only valid when the degree of perturbation is considerably smaller than the predominant components of the flow. Such a linearized truncated error analysis was performed by Hirt (1968).

The ultimate objective here, however, is not to predict the actual distribution of the truncated error but to develop the means to minimize it or even eliminate it. Until now consideration was given to the general behavior of a truncation error. The next step is to consider the actual error terms which are to be introduced when the finite-difference scheme is implemented. Using the previously introduced finite-difference formulation with an addition of high-order terms, the eq. (5.8) will acquire the following form:

$$\frac{\partial \vartheta}{\partial t} + \frac{\Delta t}{2} \frac{\partial^2 \vartheta}{\partial t^2} + \vartheta \frac{\partial \vartheta}{\partial x} = v \frac{\partial^2 \vartheta}{\partial x^2} + O(\Delta x^2, \Delta t^2) \quad (5.12)$$

The second term in the above equation is the only addition to the governing equations while all other high-order terms associated with finite-difference approximation were neglected. For simplicity the second-order time derivative is to be converted into a space derivative. Then, eq. (5.12) becomes,

$$\frac{\partial \vartheta}{\partial t} + \vartheta \frac{\partial \vartheta}{\partial x} = \left(v - \frac{\Delta t}{2} \vartheta^2 - \frac{v \Delta t}{2} \frac{\partial \vartheta}{\partial x} \right) \frac{\partial^2 \vartheta}{\partial x^2} + O(\Delta x^2, \Delta x \Delta t, \Delta t^2) \quad (5.13)$$

This clearly illustrates that the terms in brackets on right-hand side of eq. (5.13) which are defined as an effective diffusion coefficient must not at any time be negative otherwise it will tend to concentrate than diffuse a disturbance. This leads to another condition or rather restriction which indicates that a numerical solution free of instabilities is possible only for the following limited values for the diffusion coefficient,

$$v \geq \frac{\Delta t}{2} \vartheta^2 \quad \& \quad v \geq \frac{v \Delta t}{2} \frac{\partial \vartheta}{\partial x}$$

the second condition is not as significant as the first one, thus, it can be ignored. Then, P^* must be smaller than two; where P^* is defined as a modified Peclet number and it is equal to $\frac{\Delta x^* \vartheta}{v}$ and $x^* = \Delta t \vartheta$. For a number of practical applications where the viscosity is small, the Pe^* is definitely higher than 2 which implies that the above discretization is not appropriate.

The above mentioned problem can be solved using the Donnor-cell method, or upstream-differencing scheme. The scheme was first introduced

by Courant, Isaacson, Rees (1952) and subsequently developed by Los Alamos Laboratory team and others. The physical interpretation of the upwinding technique constitutes that the information to compute the properties (that includes non-linear derivative terms and transport properties, e.i. velocities) must be provided from the upstream section of the flow. The formulation eliminates the negative diffusion coefficient. Depending on the flow direction, the non-linear terms in the transport equations are discretized using a modified form of backward or forward differences, instead of central difference. For instance, if the direction of the flow is to the right, the backward difference is to be applied accordingly.

Consider a convective term in eq. (5.8) which is discretized by the following technique:

$$v \frac{\partial v}{\partial x} \equiv \frac{v_i}{\Delta x} (v_i - v_{i-1}) + O(\Delta x) \quad (5.14)$$

where,

$$v_{i-1} = v_i - \Delta x \left(\frac{\partial v}{\partial x} \right)_i + \frac{\Delta x^2}{2} \left(\frac{\partial^2 v}{\partial x^2} \right)_i + O(\Delta x^3) \quad (5.15)$$

Then, using Taylor series expansion,

$$v \frac{\partial v}{\partial x} \equiv v_i \left(\frac{\partial v}{\partial x} \right)_i - v_i \frac{\Delta x}{2} \left(\frac{\partial^2 v}{\partial x^2} \right)_i + O(\Delta x) \quad (5.16)$$

or

$$v \frac{\partial v}{\partial x} \equiv v_i \left(\frac{\partial v}{\partial x} \right)_i - \alpha |v_i| \frac{\Delta x}{2} \left(\frac{\partial^2 v}{\partial x^2} \right)_i + O(\Delta x) \quad (5.17)$$

where the second term on the right hand side is defined as the upstream differencing and α is the upstream differencing coefficient. Inserting eq. (5.17) in eq. (5.13) leads to:

$$\frac{\partial \vartheta}{\partial t} + \vartheta \frac{\partial \vartheta}{\partial x} = \left(v - \frac{\Delta t}{2} \vartheta^2 + \alpha \left| \vartheta \right| \frac{\Delta x}{2} - \frac{v \Delta t}{2} \frac{\partial \vartheta}{\partial x} \right) \frac{\partial^2 \vartheta}{\partial x^2} + O(\Delta x^2, \Delta x \Delta t, \Delta t^2) \quad (5.18)$$

To assure a positive diffusion coefficient, it is therefore required that

$$v + \alpha \left| \vartheta \right| \frac{\Delta x}{2} \geq \frac{\Delta t}{2} \vartheta^2 + \frac{v \Delta t}{2} \frac{\partial \vartheta}{\partial x} \quad (5.19)$$

Dividing inequality (5.19) by v , one obtains

$$1 + \alpha \left| \vartheta \right| \frac{\Delta x}{2v} \geq \frac{\Delta t}{2v} \vartheta^2 + \frac{\Delta t}{2} \frac{\partial \vartheta}{\partial x} \quad (5.20)$$

Since, v has a relatively small value, $Pe^* \leq 2 + \alpha Pe$. But Pe is always greater than or equal to Pe^* provided that the Courant number is satisfied; hence, it is essential to implement the upstream differencing in order to avoid numerical instability.

5.3 Fractional Volume Function

Problems with the presence of a free boundary have always posed a number of difficulties, in particular, when a finite-difference formulation were implemented. In principle, the difficulty comprises of trapping a free boundary which can arbitrarily be located anywhere within a computational mesh. The earlier developed 2-d algorithm, SOLA-SURF partially accommodated the above requirements. The principle of treating the free boundaries in the latter algorithm was to define a single-valued function, $H(x,t)$ or $H(y,t)$ which represents the distance of the free surface from a rigid boundary. This is feasible only in the case when the slope (dy/dx) of a free boundary at any free boundary cell of computational domain is either less or greater than one. In other words, the measure of function, H , is virtually limited to either a vertical or horizontal position but not both. This principal restriction of SOLA-SURF does not permit any further developments of the algorithm when the application of a 3-d case is required.

Based on their original SOLA-SURF the Los-Alamos Laboratory team introduced another 2-d algorithm, SOLA-VOF which treats the free boundaries in a different fashion. The principal difference is the introduction of a fraction volume scheme which permits more flexibility in trapping the free boundary. This scheme introduces an intrinsic function $F(x, y, z, t)$, the volume of fluid function (VOF), whose values are unity for cells filled with fluid and zero for void cells. Although the virtual nature of F is characteristic to a step function, the entire numerical scheme must still retain the principles of continuum mechanics. F must acquire an intermediate values of zero and unity; thus, cells with values of F between zero and unity contain

the free boundary; correspondingly, the novel function is recognized as *the fractional volume function*.

The continuum principles indicate that the total differential of F with respect to time within a given control volume must be equal to zero:

$$\frac{D}{Dt}(F) = \frac{\partial F}{\partial t} + \bar{V} \cdot (\nabla F) = 0 \quad (5.21)$$

where \bar{V} is the velocity vector. Hypothetically, the latter principle is identical when the fractional volume function is to be defined for the case of solid mechanics. One can consider a solid body of finite volume which, under elastic deformation, still retains its original volume regardless of the final shape of the body. Analogously, for incompressible fluids, the total change of an assigned control volume with respect to time must be equal to zero.

Combining the continuity equation and eq. (5.21) will lead to

$$\frac{\partial F}{\partial t} + \bar{V} \cdot (\nabla F) + F \nabla \cdot \bar{V} = 0$$

or

$$\frac{\partial F}{\partial t} + \nabla \cdot (F \bar{V}) = 0 \quad (5.22)$$

However, the above equation is valid only for the region filled with fluid since continuity equation does not hold at free boundary interface.

The behavior of F entirely depends on the velocity distribution in three mutually perpendicular directions, namely, the incoming or outgoing fluxes of the cell under consideration influences the value of F which mathematically, is expressed by eq. (5.22). In cylindrical coordinates eq. (5.22) has the form,

$$\frac{\partial F}{\partial t} + u \frac{\partial F}{\partial x} + v \frac{\partial F}{\partial y} + \frac{w}{x} \frac{\partial F}{\partial z} = 0 \quad (5.23)$$

Application of the Eulerian principle of discretization for the time derivative and standard finite-difference approximations for space derivatives will lead to a misinterpretation of fractional-volume function. The most appropriate way to obtain F is based on the calculations of the net flux throughout the cell, see Nichols et al (1985).

5.4 Boundary conditions

Uniqueness of the solution depends entirely on initial and boundary conditions of a given problem. As a matter of fact, the numerical simulation cannot be performed without setting physical boundaries of the problem. The present work requires the application of various types of boundary conditions. At the fluid-solid body interface *free-slip*, *non-slip* or *moving wall* conditions may be implemented. If the condition is a rigid free-slip wall, then the velocity normal to the wall must be equal to zero and the gradient of the tangential (to the wall) velocity component is also zero, fig. 5.2. The physical significance of the latter condition is to simulate no dissipation effect due to the presence of a rigid wall and no penetration of flow in a direction normal to the wall.

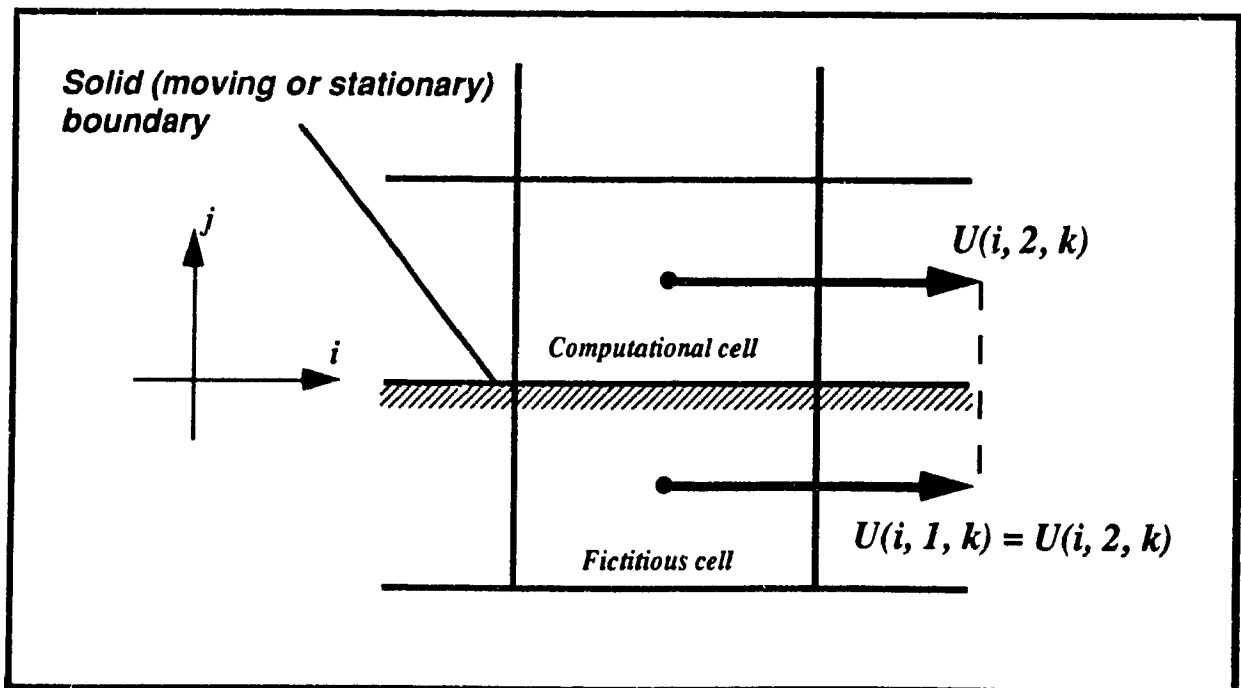


Fig. 5.2. Free-slip boundary conditions.

Similar to the free-slip boundary condition, the non-slip condition requires that the normal as well as the tangential to the wall velocity components must be zero. In the mathematical sense, the tangential velocity on the fictitious boundary cells which surrounds the computational grid field is set to be equal to the negative tangential velocity right over the wall, fig. 5.3. The non-slip condition is a rough approximation to the flow near the rigid boundary.

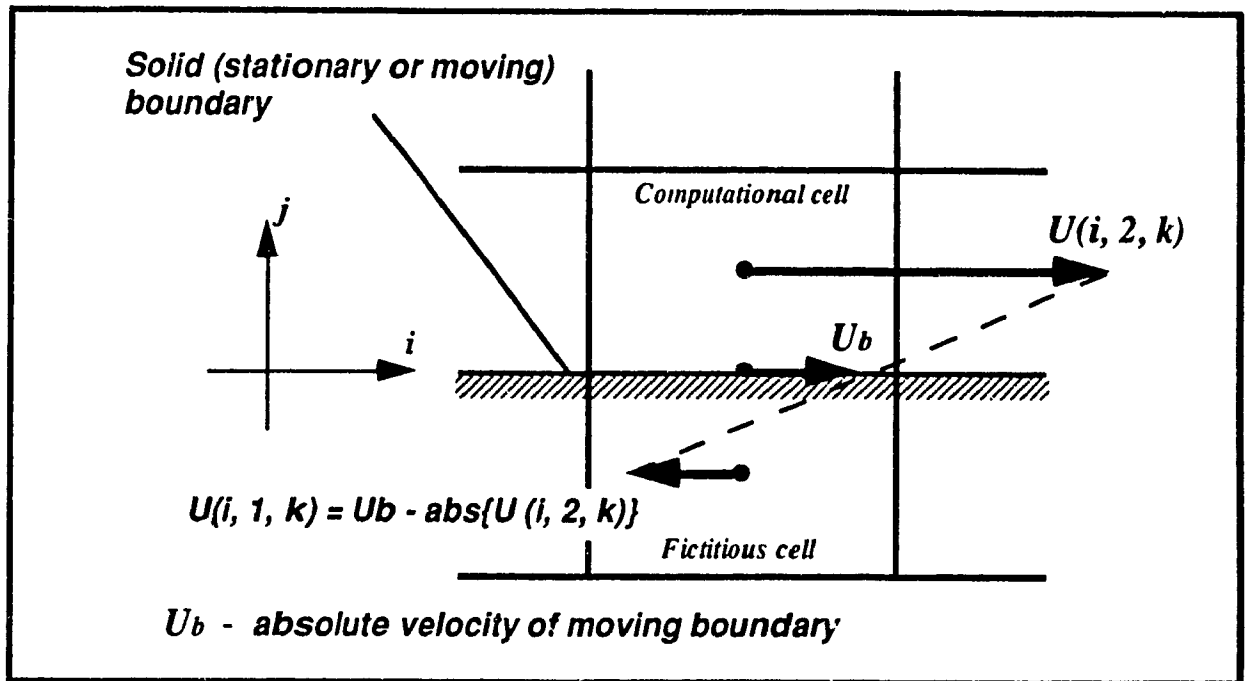


Fig. 5.3. Non-slip boundary conditions.

A moving wall is another type of boundary condition which allows the simulation of moving boundaries. If it is required, for instance, to implement the presence of a rotating disk, then the tangential velocity of the fluid at the solid-fluid interface must be equal to that of the disk. Using linear interpolation, one can obtain the required algebraic relationship between the tangential velocity of the fictitious cell and the velocity right above the disk

(fig. 5.3). The conditions for the other velocity components are imposed according to the non-slip formulation.

The application of periodic boundary conditions is essential for problems where there is a repetitive nature of either the flow field or the structure of the computational grid. Since the problem is governed by the equations of motion in a cylindrical coordinate system which can also be viewed as the equations which have been transformed from a Cartesian space. Such a transformation permits one to view the flow field in a rectangular grid structure instead of a cylindrical one. This is identical to the principle of conformal mapping. Thus, due to the presence of a fictitious layer, the end cells in the azimuthal direction when $\theta = 2\pi$ overlap with the flow domain cells which are one cycle behind (when $\theta = 0$). This condition is implemented using the following relationships:

$$v_{i,j,1} = v_{i,j,k_{\max} - 1}$$

&

$$v_{i,j,k_{\max}} = v_{i,j,2}$$

where v is a general physical property.

Similarly, the fictitious cells at the geometrical center for $\theta = 0$ overlap with the vertical layer containing flow domain cells when $\theta = \pi$. This condition is numerically applied using the following relations:

$$v_{1,j,k} = v_{2,j,k_{m2}}$$

where,

$$KM2 = \frac{KMAX - 2}{2} + k; \text{ for } KMAX - 2 \leq \frac{KMAX - 2}{2} + 1$$

$$k - \frac{KMAX - 2}{2}; \text{ for } KMAX - 2 \geq \frac{KMAX - 2}{2} + 1$$

providing that kmax is an even number, fig. 5.4.

Special attention must be attributed to free surface boundary conditions which are considerably sensitive to any type of physical abnormalities that may be involved when developing a numerical algorithm; this may include the inevitable effects of truncated errors, size of a grid field, etc. Applying the free surface boundary conditions the following two requirements,

Normal stress

$$-P + 2\mu \frac{\partial U_n}{\partial n} = 0 \quad (5.24)$$

Tangential stress

$$\frac{\partial U_n}{\partial m} + \frac{\partial U_m}{\partial n} = 0 \quad (5.25)$$

must be satisfied, where U is the velocity vector, n and m are spatial components in directions normal and tangent to the surface interface respectively. In cylindrical coordinates, the normal stress conditions are

$$-P + 2\mu \frac{\partial u}{\partial x} = 0$$

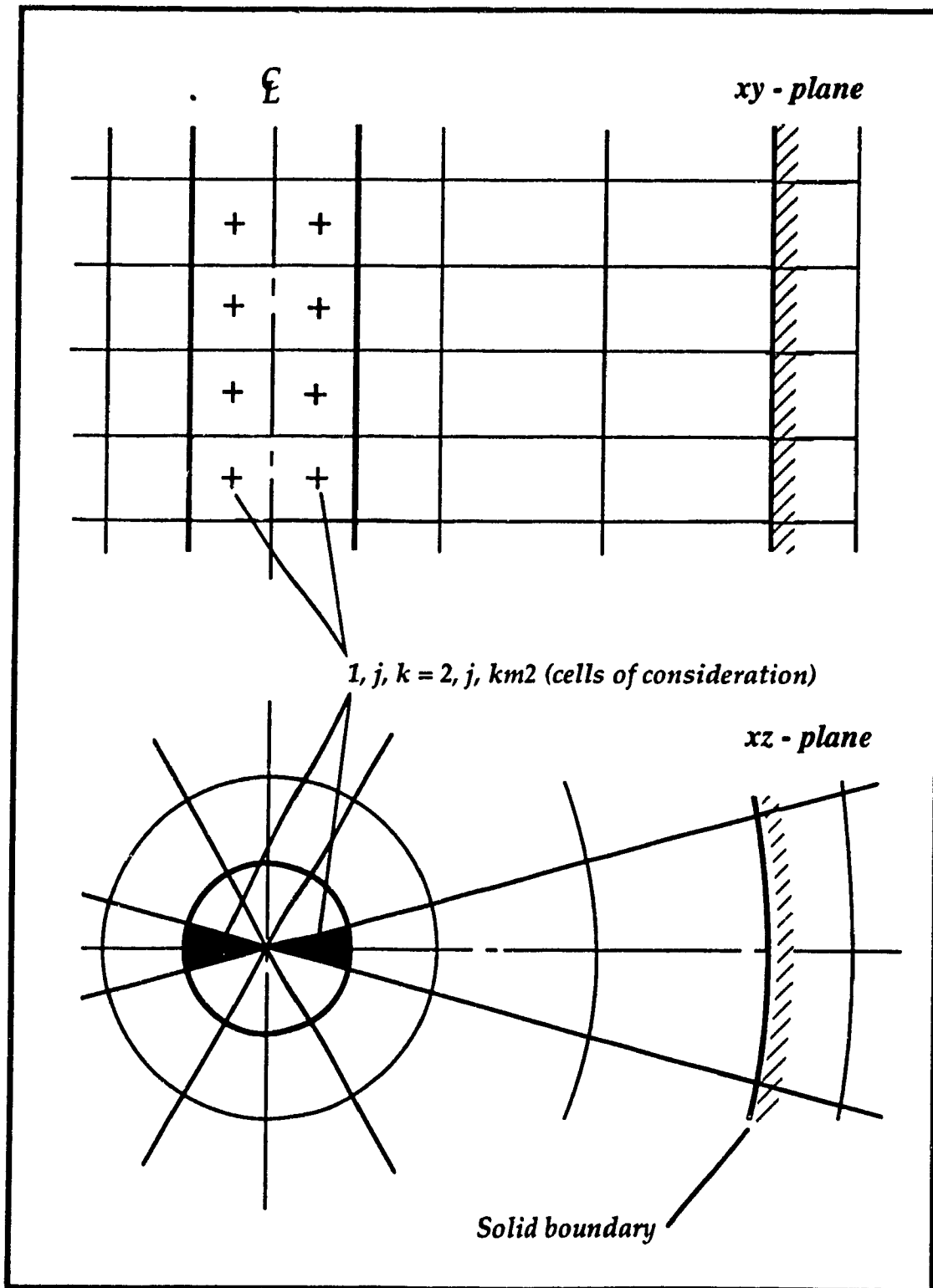


Fig. 5.4. Azimuthal boundary conditions.

$$-P + 2\mu \left(\frac{1}{x} \frac{\partial w}{\partial z} + \frac{u}{x} \right) = 0$$

$$-P + 2\mu \frac{\partial v}{\partial y} = 0$$

Addition of the three normal stress components give,

$$P = \frac{2\mu}{3} \left(\frac{\partial u}{\partial x} + \frac{1}{x} \frac{\partial w}{\partial z} + \frac{\partial v}{\partial y} + \frac{u}{x} \right) = \frac{2\mu}{3} D \quad (5.26)$$

which clearly shows that normal stress conditions are satisfied automatically when pressure iteration technique is performed.

Contrary to the normal stress relations, tangential stress conditions must be applied explicitly. The following relations are obtained using the cylindrical transformation:

$$\frac{1}{x} \frac{\partial u}{\partial z} + \frac{\partial w}{\partial x} - \frac{w}{x} = 0 \quad (5.27.a)$$

$$\frac{\partial u}{\partial y} + \frac{\partial v}{\partial x} = 0 \quad (5.27.b)$$

$$\frac{1}{x} \frac{\partial v}{\partial z} + \frac{\partial w}{\partial y} = 0 \quad (5.27.c)$$

These may be incorporated directly into the numerical algorithm; however, it will involve a number of undesirable complications. In particular, additional partial differential equations have to be solved implicitly. This can be avoided by employing the following hybrid relations obtained from eq. (5.27)

$$\frac{\partial u}{\partial z} = 0 \quad \& \quad \frac{\partial(xw)}{\partial x} = 0 \quad (5.28.a)$$

$$\frac{\partial u}{\partial y} = 0 \quad \& \quad \frac{\partial v}{\partial x} = 0 \quad (5.28.b)$$

$$\frac{\partial v}{\partial z} = 0 \quad \& \quad \frac{\partial w}{\partial y} = 0 \quad (5.28.c)$$

The expressions possess the same principle of numerical implementation with the free-slip solid wall boundary conditions.

5.5 Computational procedure

Assigning initial values of velocities and pressure, the numerical algorithm employs a time-marching technique to advance the flow field toward the successive time level. A preliminary computation of velocities is performed using discretized momentum equations followed by a pressure iterating technique to assure that continuity equation is satisfied. This double stage step is accomplished at a fixed time frame which is followed by a consecutive time-march to the next time step. The process is repeated on the basis of the previously obtained values of dependent variables until a desirable time level is reached.

Although the discretized equations enable one time-step, the newly computed values of velocities will not, in general, satisfy the continuity requirements. In order to satisfy continuity equation for each and every computational cell (excluding those which contain a free surface), the pressure in each cell must be adjusted appropriately. Physically speaking, the velocities computed according to eq. (5.20) invoke the inconsistency of a net outflux or influx at a single cell. The degree of inconsistency is measured by introducing the residual value of D (divergence) which theoretically must be minimized to zero by means of changing the pressure within cells; for instance, if there is an excessive accumulation of mass within the cell, the value of pressure must be lowered appropriately, or if there is a depletion of mass, the pressure must be increased correspondingly. Qualitatively, the change of velocity within the cell on the four faces of a cell is related to pressure increment and other independent variables employing the equations of motion,

$$U_{i,j,k} \rightarrow U_{i,j,k} + \frac{\Delta t \Delta P}{\Delta x}$$

$$U_{i-1,j,k} \rightarrow U_{i-1,j,k} - \frac{\Delta t \Delta P}{\Delta x}$$

$$V_{i,j,k} \rightarrow V_{i,j,k} + \frac{\Delta t \Delta P}{\Delta y}$$

$$V_{i,j-1,k} \rightarrow V_{i,j-1,k} - \frac{\Delta t \Delta P}{\Delta y}$$

$$W_{i,j,k} \rightarrow W_{i,j,k} + \frac{\Delta t \Delta P}{x \Delta z}$$

$$W_{i,j,k-1} \rightarrow W_{i,j,k-1} - \frac{\Delta t \Delta P}{x \Delta z}$$

The above relations are substituted into the discretized continuity equation to obtain the following expression for the residual value of divergence D:

$$D = \nabla \cdot \bar{V} = -2\Delta t \Delta P \left(\frac{1}{(\Delta x)^2} + \frac{1}{(\Delta y)^2} + \frac{1}{(x \Delta z)^2} \right)$$

There are two unknowns in the above equation which can be evaluated by breaking it down into two independent equations:

$$D = \nabla \cdot \bar{V}$$

$$\Delta P = - \frac{D}{2\Delta t \left(\frac{1}{(\Delta x)^2} + \frac{1}{(\Delta y)^2} + \frac{1}{(x \Delta z)^2} \right)} \quad (5.29)$$

Thus, pressure within a cell is changed according to:

$$P \rightarrow P + \Delta P$$

For cells containing the free surface, an interpolation technique is required to update the cell pressure. For simplicity, consider the 2-d case of free surface profile shown in fig. 5.5. If the free surface profile deflects locally less than 45° , then the cell right below the free surface cell is the adjacent full cell. Nichols et al (1971) suggest the following expression of pressure interpolation/extrapolation

$$\Delta P = \eta(P_a - P_{ns}) + (1 - \eta)P_f - P_s$$

where P_a is the pressure right above the free surface, P_{ns} is the pressure due to surface tension, P_s is the current value of pressure within a surface cell, P_f is the pressure of the adjacent full cell and η is the interpolation factor which mathematically can be expressed by either,

$$\eta = \frac{\Delta y}{d} \text{ or } \eta = \frac{\Delta x}{d} \text{ or } \eta = \frac{x \Delta z}{d}$$

depending on the angle of deflection.

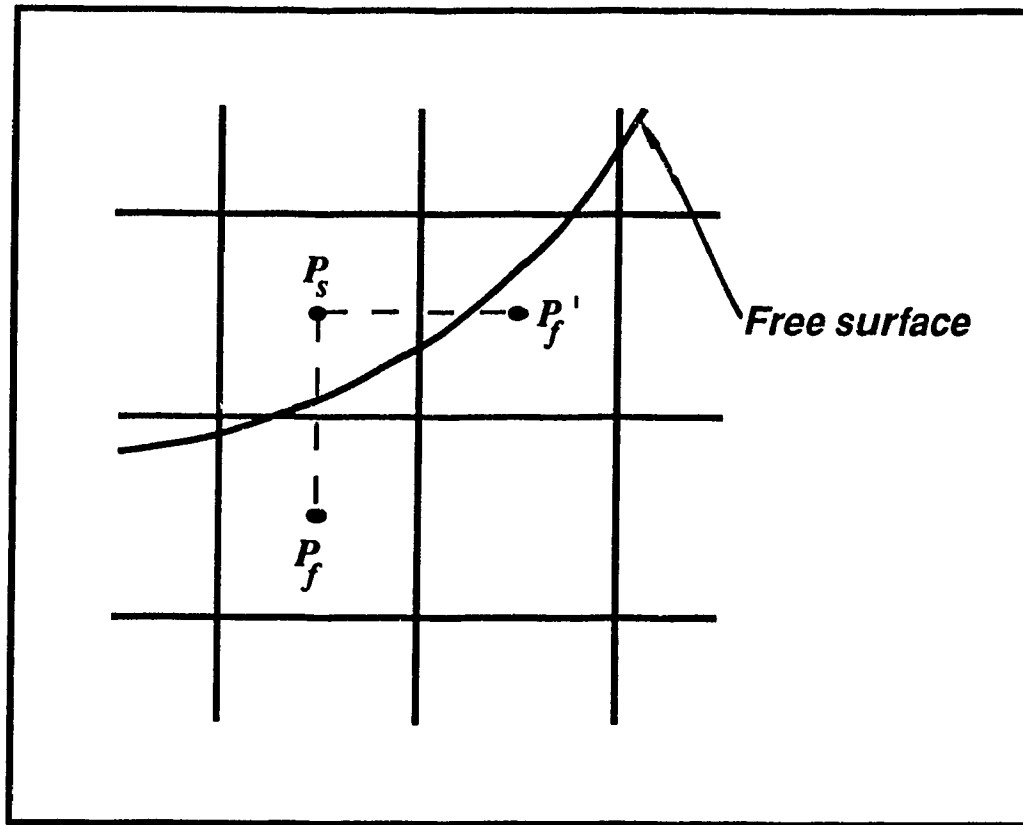


Fig. 5.5. Pressure interpolation on a free surface interface.

In order to accelerate the iteration procedure or even prevent numerical instability, it is advisory to multiply the pressure increment, ΔP , by a relaxation factor, ω . Qualitatively, this factor depends on the number of computational cells present in a boundary domain. An optimum value of ω is 1.8 for a grid field of over 500 cells and 1.2 to 1.5 for smaller grid field; in no case, should the value of ω exceed 2.0 otherwise an unstable iteration will result.

In summary, the entire computational procedure consists of three major steps. The first step is the evaluation of velocities for a new time step based on previously calculated dependent variables, velocities and pressure. The computation proceeds using time-dependent finite difference Navier-Stokes

equation. The adjustment of velocities using pressure correction procedure is required since newly calculated values of velocities will not satisfy the continuity requirements. During the second step, i.e. the process of the iteration, each cell is considered successively and a pressure change drives its instantaneous divergence to zero. Finally, when convergence is achieved for every cell in the entire flow domain, the velocity and pressure advance a successive time step and are used as starting values for the next cycle. The entire procedure is repeated until a desired time level is reached.

5.6 Numerical Results

One of the prime objectives using a numerical technique is first to validate the computer code. This was achieved here by comparing the numerically obtained free surface profile with the experimental results. The results shown in fig. 5.6 have been obtained for flow conditions at which the rotating core remains relatively undisturbed. According to the figure, there is a satisfactory match between the numerical and the experimental free surface profiles. It is clear from the numerical results, presented in the same figure, that small surface waves are present on the interface. These waves, generated in the vortex center convect upwards moving along the free surface. This phenomenon bears the universal characteristics of the diffusion mechanism. During experiments these small amplitude travelling waves have also been observed.

Consider fluid particles in an axial-radial plane set in motion by a rotating disk. Due to the centrifugal force some of the particles will be repelled outwards along the radial direction until they sense the circumferential wall. The solid boundary will then redirect their motion upwards and then the free surface will force them to flow towards the center. Continuity will then compel the particles to close the loop thus generating a recirculating cycle. The problem, however, is 3-dimensional which implies that the fluid not only possess a recirculating behavior in the radial-axial plane but it also undergoes a rotational motion in the radial-azimuthal plane. In the general sense, the particle motion excels in a spiral-like fashion around the surface of the secondary *flow toroid*. Depending on the type of vortex mode (whether it is a combination of free and forced or just forced vortex) the spiral-like

trajectory of the particle around the surface of the toroid may take various paths. The trajectory path may shrink or expand in the azimuthal direction due to the Coriolis effect which is indeed present in the governing equations. Alternatively, the spiral-like path may be viewed as a helix in a Cartesian coordinate system which does not necessarily possess the typical equally spaced coils. In other words, viewing the toroid from the top, the angle between the tangent at any arbitrary point along the path and the line drawn from the center of rotation to the same arbitrary point is not constant as opposed to a normal helix.

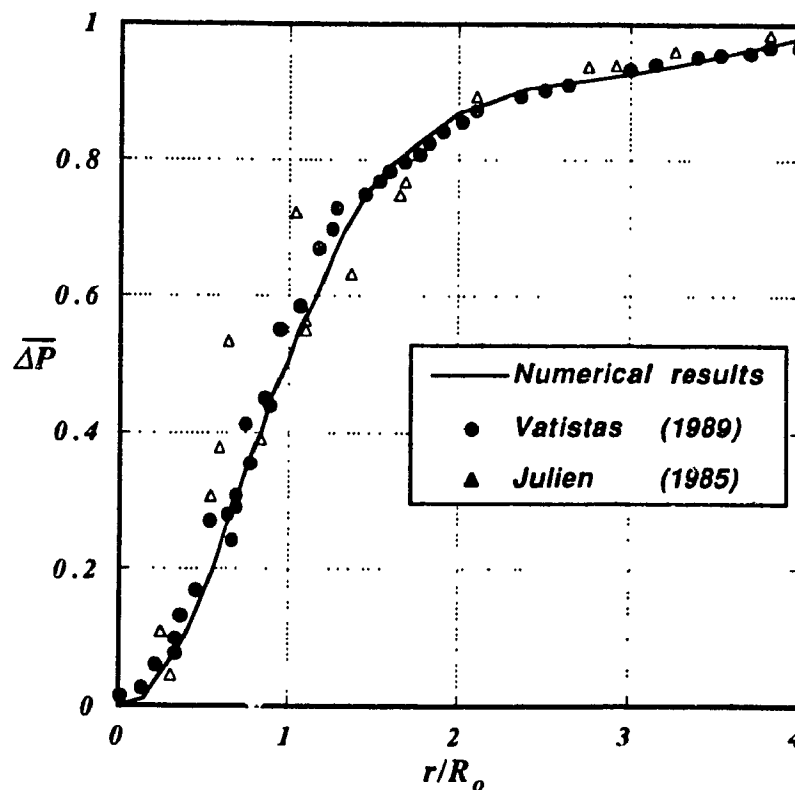


Fig. 5.6. Comparison of numerically obtained free surface profile with some experimental results.

The degree of influence of the Coriolis force depends strictly on the tangential velocity component of the moving particle and on the magnitude

of the viscous-dissipation forces which normally occurs in the vicinity of moving or stationary boundaries. The Coriolis effect becomes more predominant in the regions where vorticity is virtually equal to zero. On the other hand this is not significant in the region of the boundary layer where viscous-dissipation forces dominate. Hence, as a fluid particle is repelled towards the circumferential wall of the cylindrical container, it does not experience the same Coriolis effect to the particle that is impelled towards the line of rotation following the contour on the free surface. This line of argument might explain the irregularities of spiral-like type path.

The obtained numerical results of secondary flow motion are combined in the sets of velocity-vector plots corresponding to three different diameters, 0.08 (3.15), 0.12 (4.72) and 0.20 m (7.87 in), two viscosity values 5.0 (10^{-4}), 5.0 (10^{-5}) m^2/sec and various angular speeds. The results are combined (Fig. 5.7) where the history of evolution of the secondary flow field under various prevailing conditions is demonstrated.

Consider, for instance, the case when $\Omega = 100 \text{ rad/sec}$, $r_{\text{disk}} = 0.06 \text{ m}$, $h_0 = 0.07 \text{ m}$ (fig. 5.7.a). The fluid in a cylindrical container is initially at rest which numerically implies that the three velocity components are set to zero at every computational cell. The pressure is zero at every cell above the free surface interface and hydrostatic inside the liquid, and the volume-fraction function is set to unity in the region filled with fluid and zero elsewhere. The selected spatial increments are $\Delta x = 0.005 \text{ m}$, $\Delta y = 0.005 \text{ m}$, $\Delta z = \pi/9 \text{ rad}$, and $\Delta t = 0.00075 \text{ sec}$ satisfied the required stability criteria. At time equals to 0^+ the disk starts to rotate at a given angular speed. The flow patterns expressed as velocity-vector plots were obtained at various time levels.

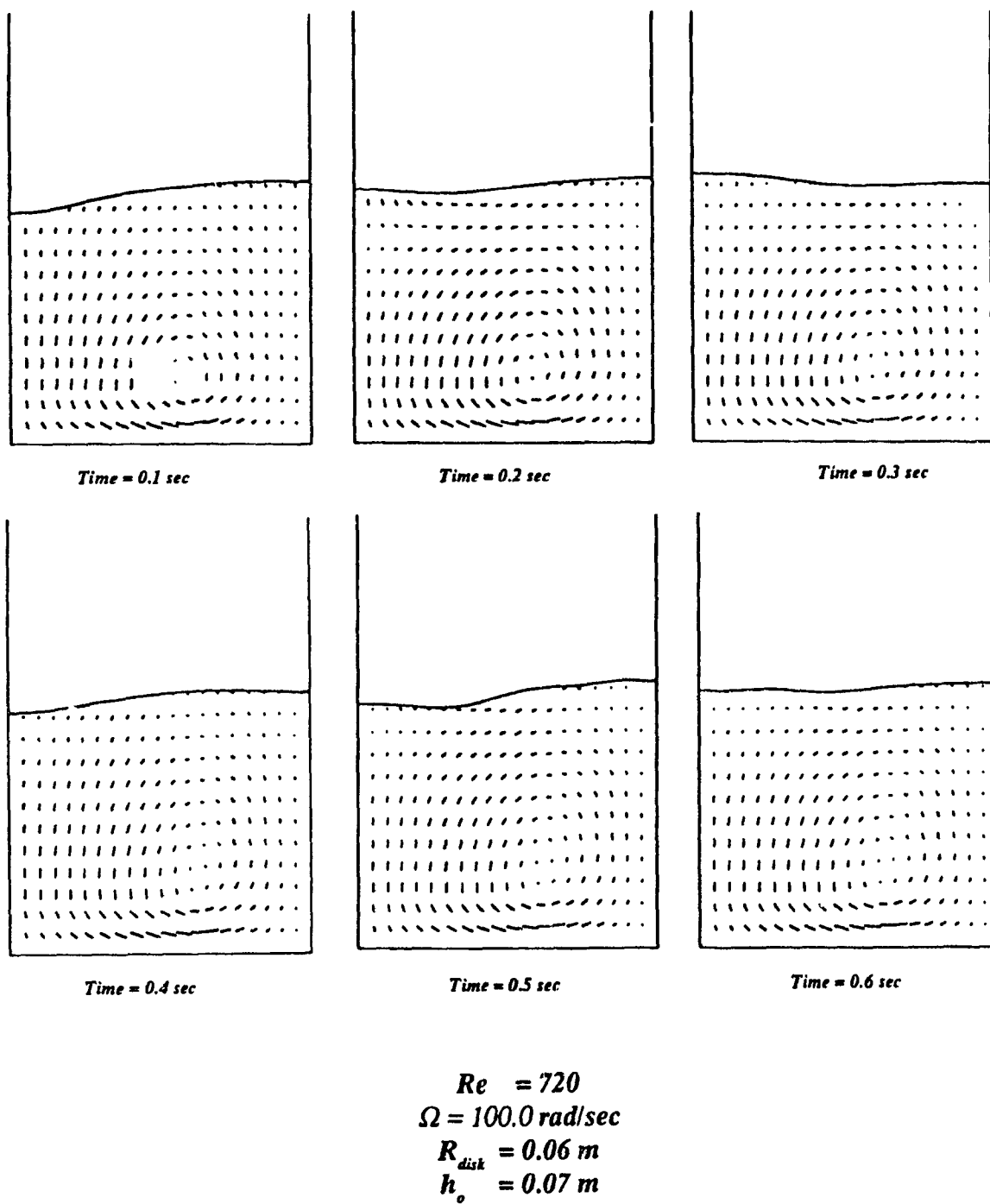
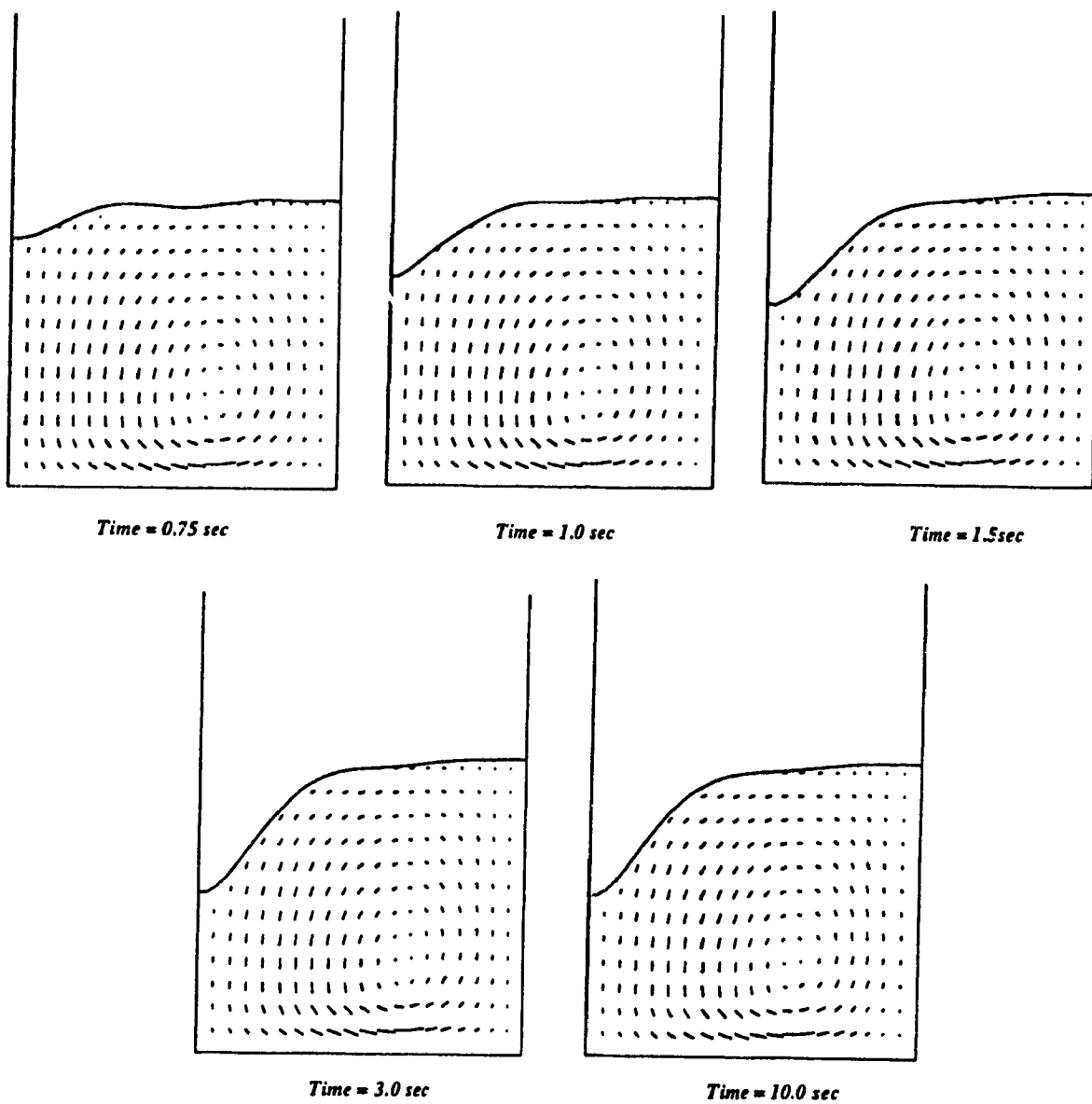
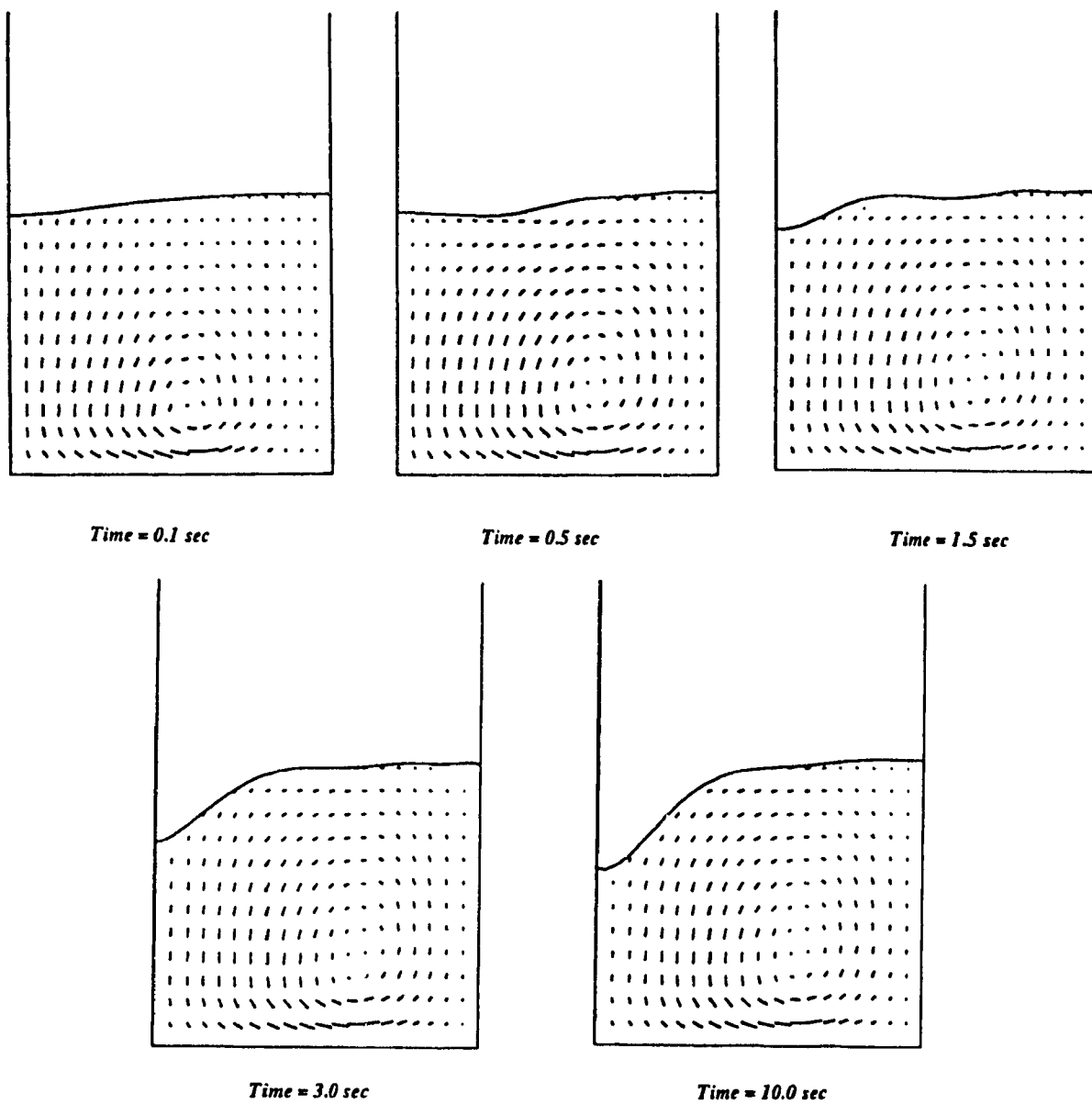


Fig. 5.7. a. The history of evolution of the secondary flow field.



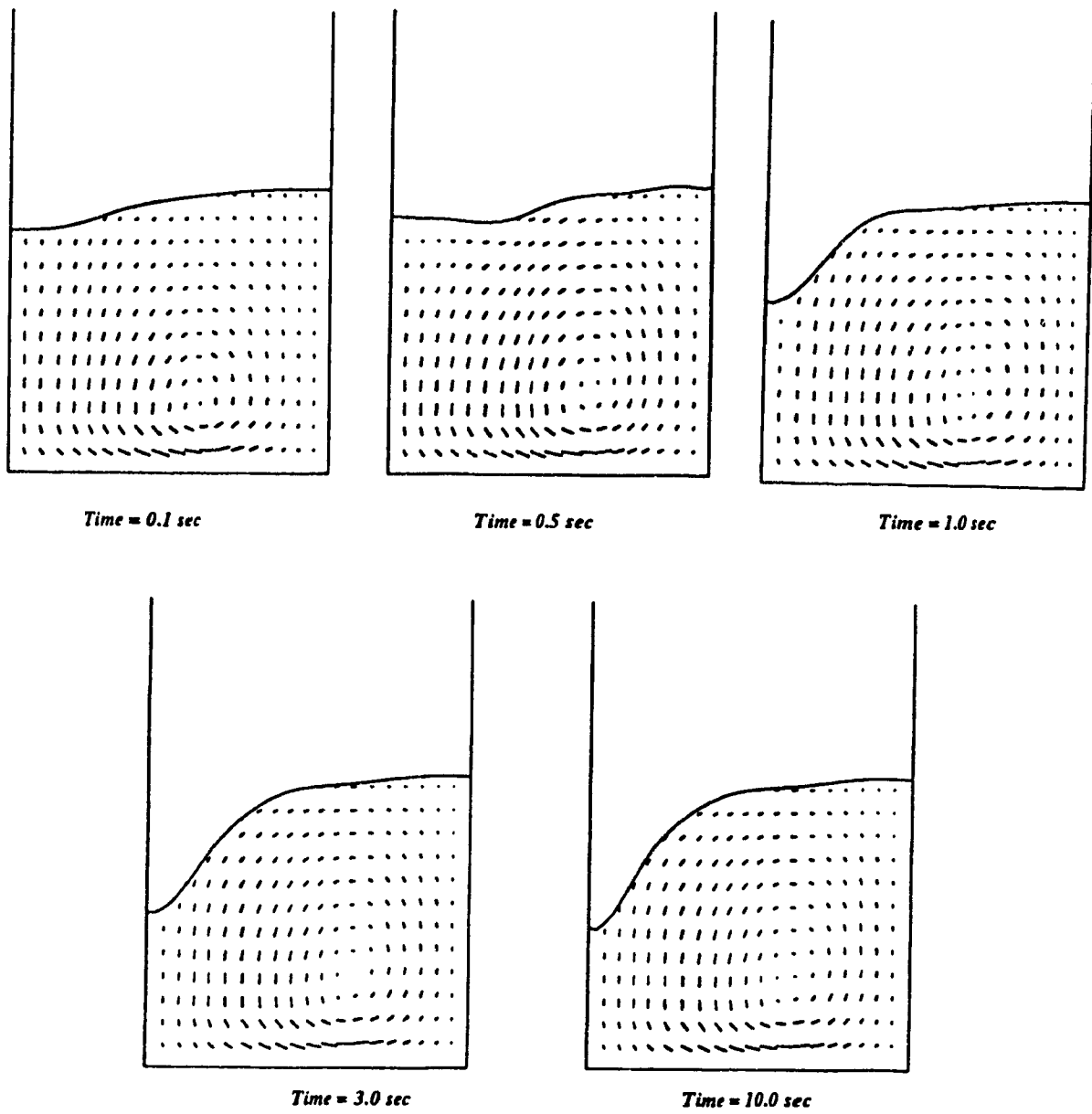
$$\begin{aligned}
 Re &= 720.0 \\
 \Omega &= 100.0 \text{ rad/sec} \\
 R_{\text{disk}} &= 0.06 \text{ m} \\
 h_o &= 0.07 \text{ m}
 \end{aligned}$$

Fig. 5.7. b. The history of evolution of the secondary flow field.



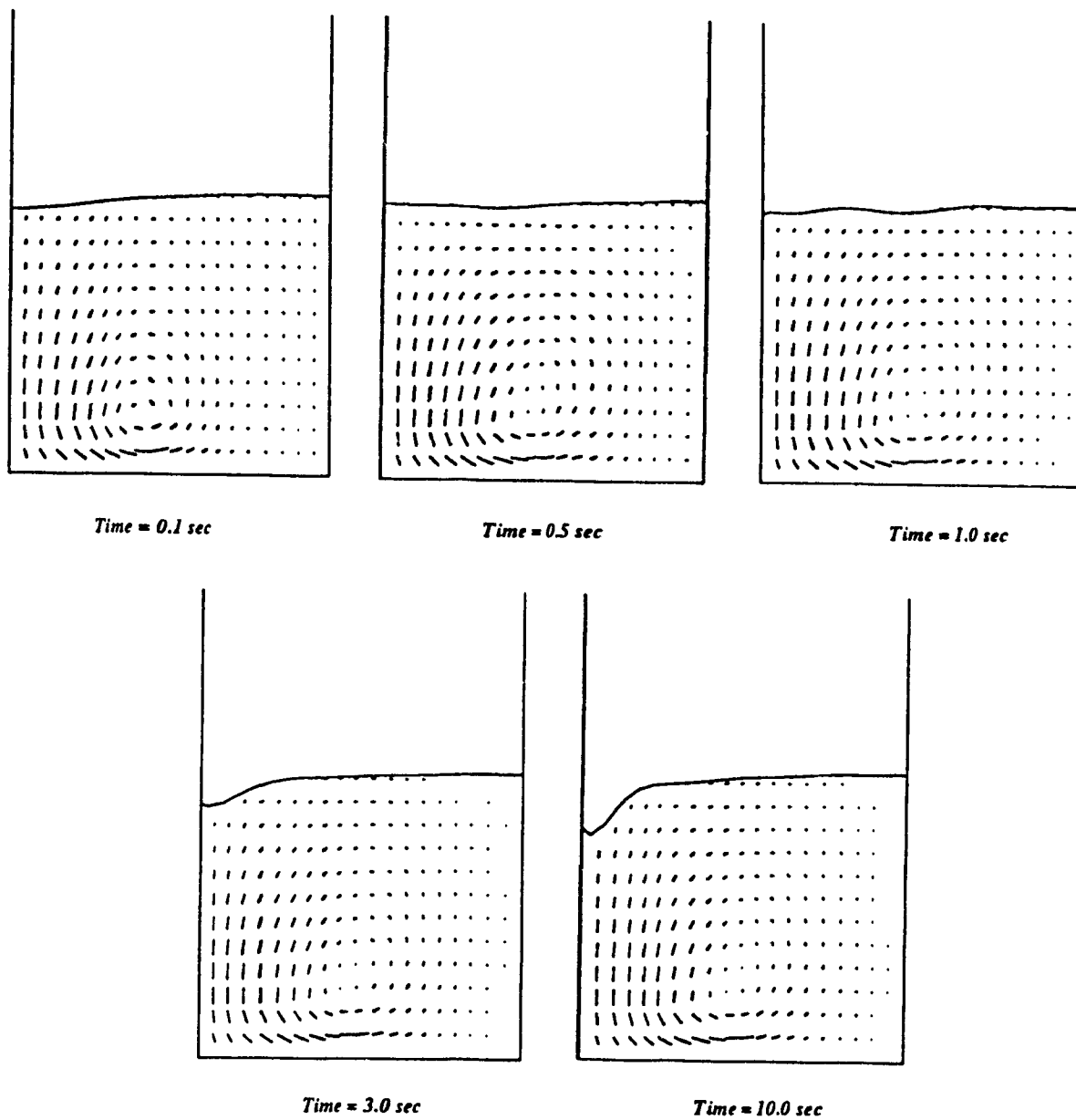
$$\begin{aligned}
 Re &= 575.0 \\
 \Omega &= 80.0 \text{ rad/sec} \\
 R_{disk} &= 0.06 \text{ m} \\
 h_o &= 0.07 \text{ m}
 \end{aligned}$$

Fig. 5.7. c. The history of evolution of the secondary flow field.



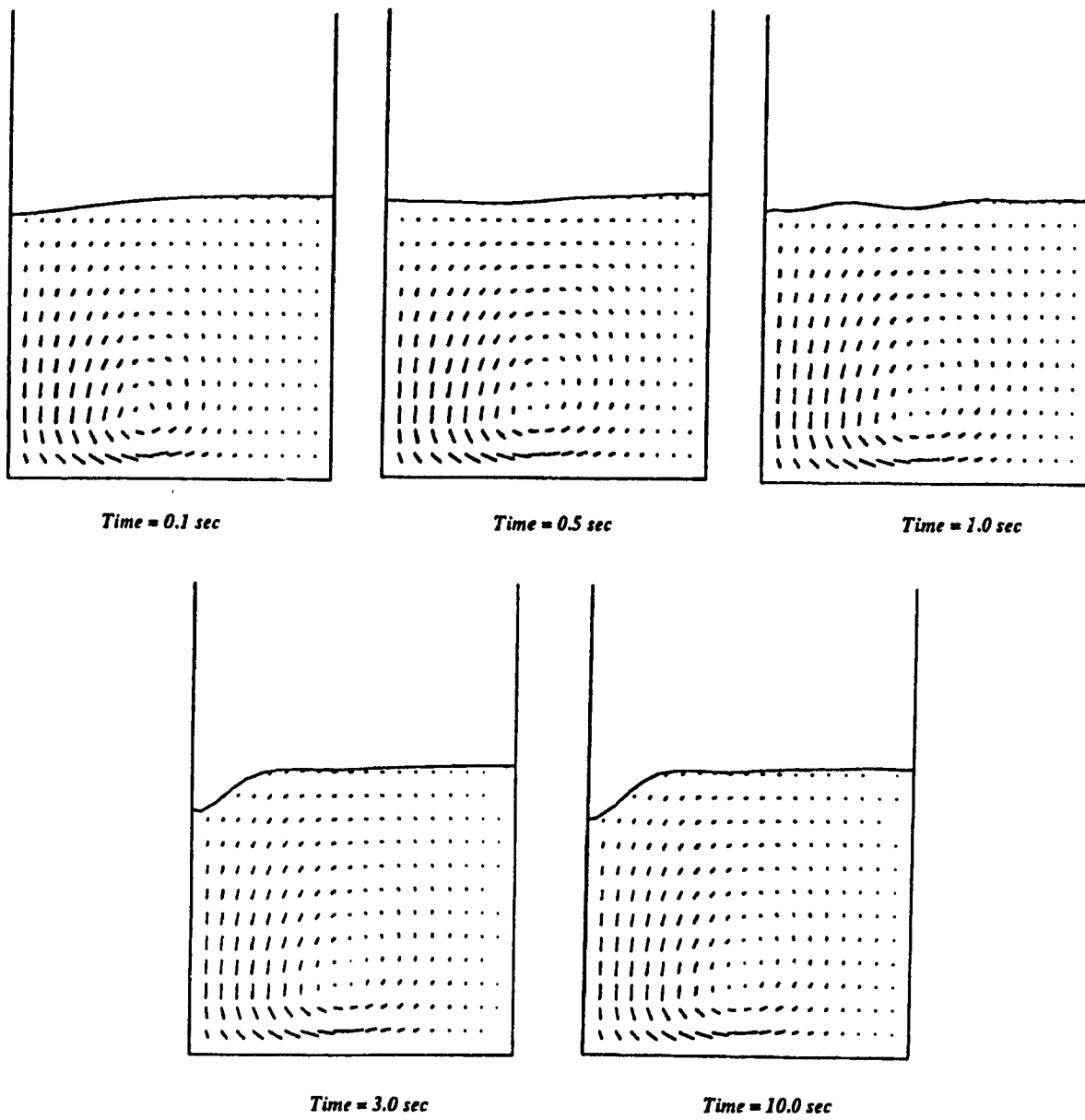
$$\begin{aligned}
 Re &= 863.99 \\
 \Omega &= 120.0 \text{ rad/sec} \\
 R_{\text{disk}} &= 0.06 \text{ m} \\
 h_o &= 0.07 \text{ m}
 \end{aligned}$$

Fig. 5.7. d. The history of evolution of the secondary flow field



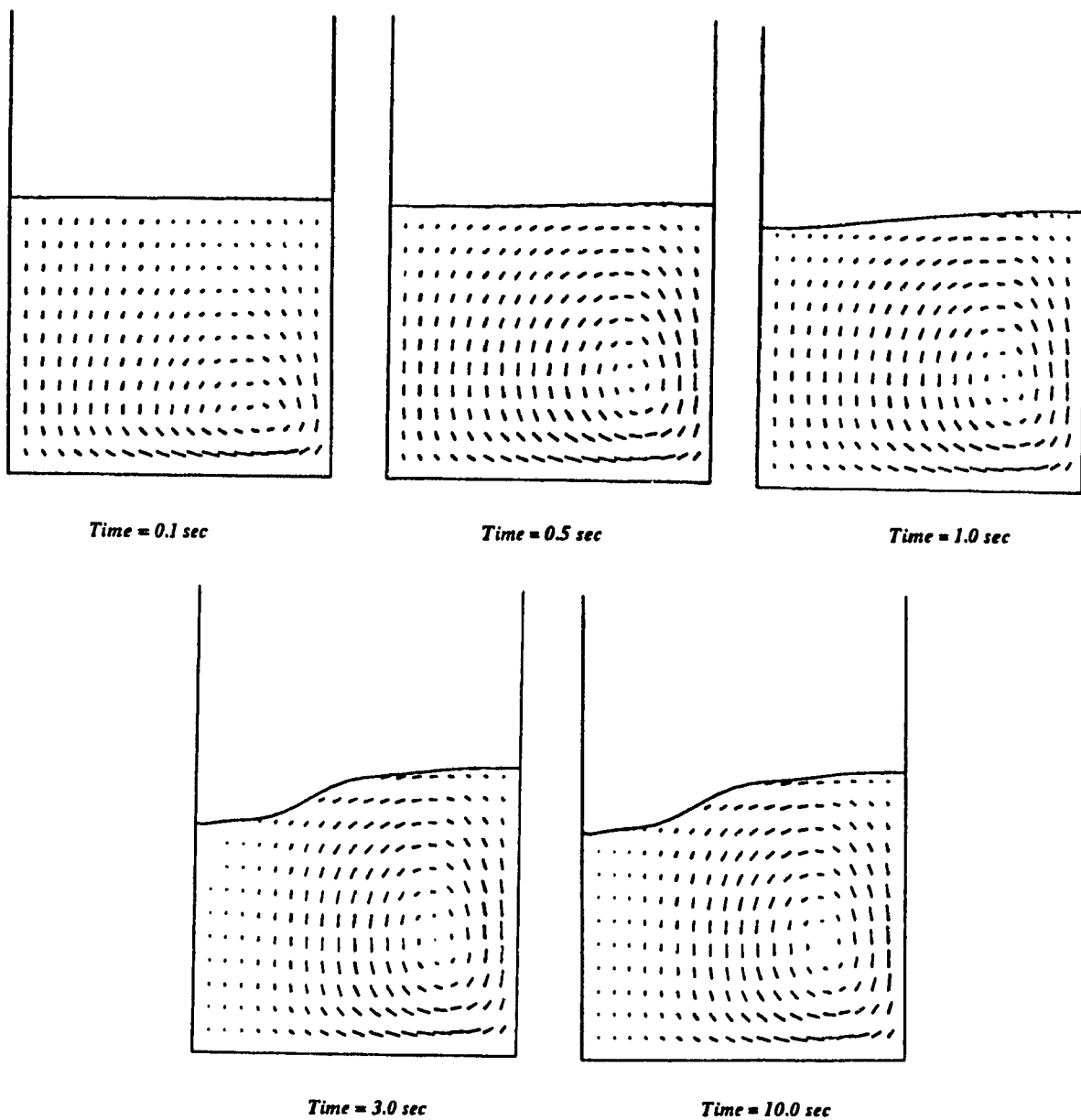
$$\begin{aligned}
 Re &= 560.0 \\
 \Omega &= 175.0 \text{ rad/sec} \\
 R_{\text{disk}} &= 0.04 \text{ m} \\
 h_o &= 0.07 \text{ m}
 \end{aligned}$$

Fig. 5.7. e . The history of evolution of the secondary flow field.



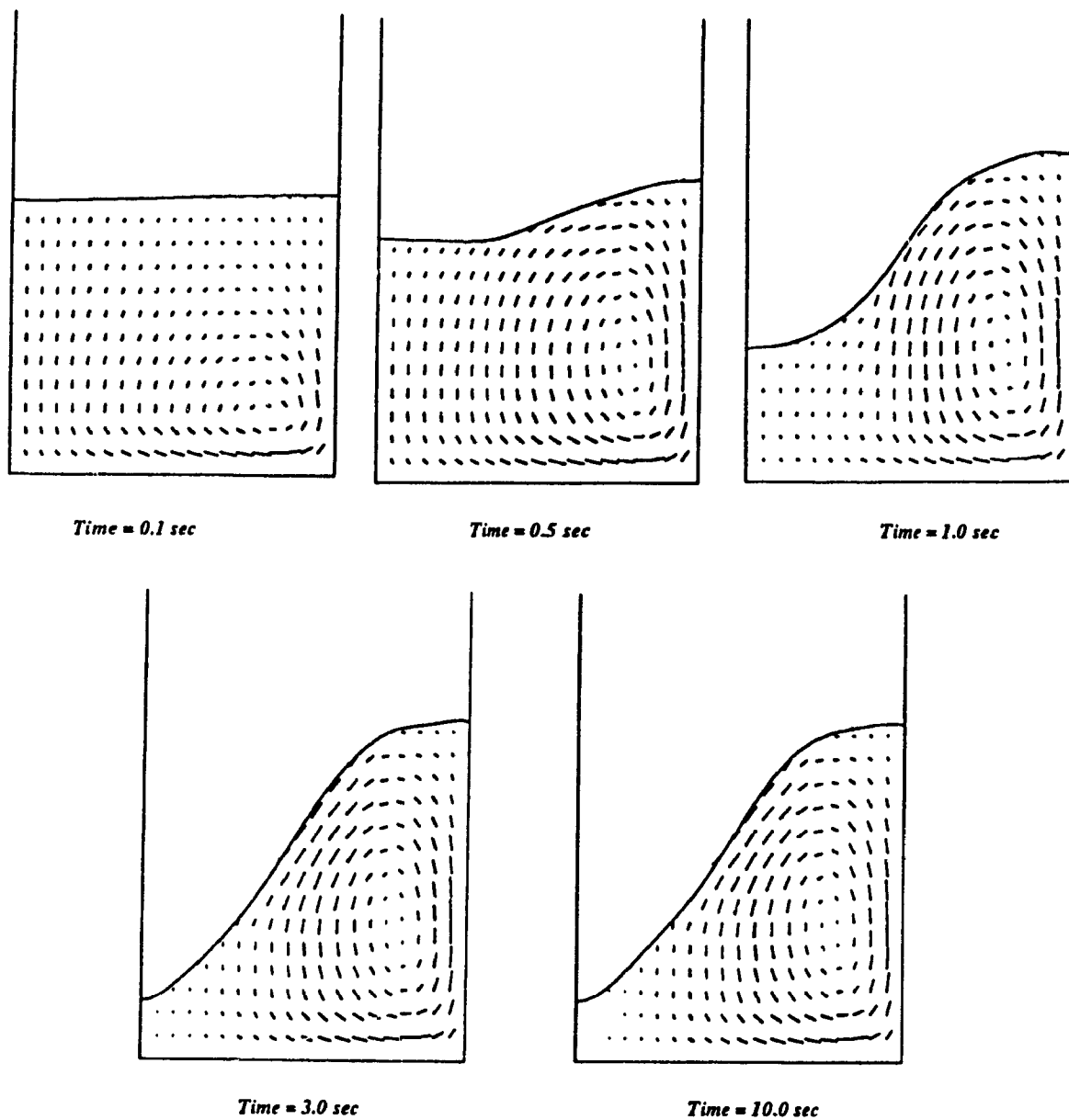
$$\begin{aligned}
 Re &= 639.0 \\
 \Omega &= 200.0 \text{ rad/sec} \\
 R_{disk} &= 0.04 \text{ m} \\
 h_o &= 0.07 \text{ m}
 \end{aligned}$$

Fig. 5.7. f. The history of evolution of the secondary flow field.



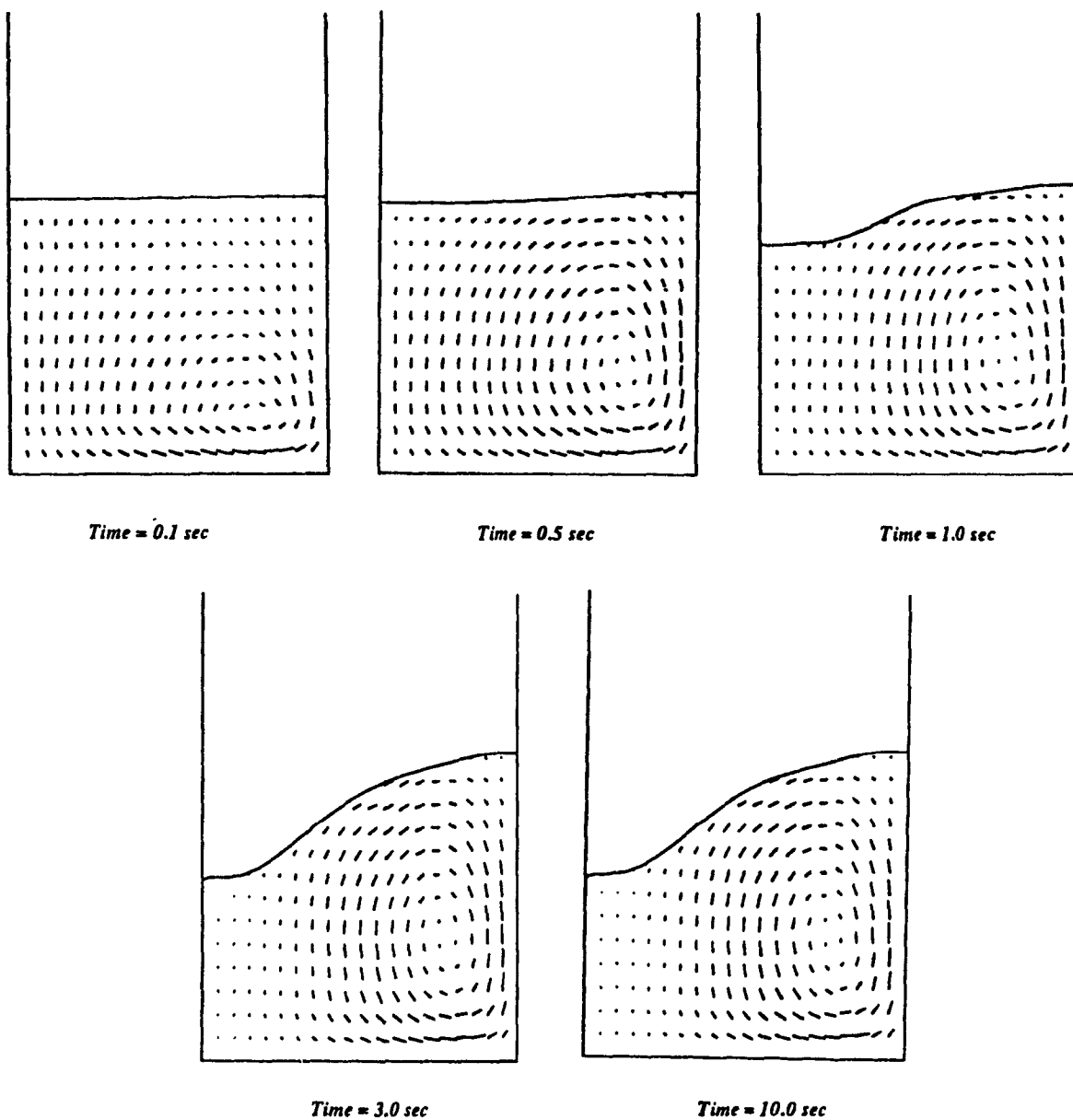
$$\begin{aligned}
 Re &= 300.0 \\
 \Omega &= 15.0 \text{ rad/sec} \\
 R_{\text{disk}} &= 0.10 \text{ m} \\
 h_o &= 0.07 \text{ m}
 \end{aligned}$$

Fig. 5.7. g . The history of evolution of the secondary flow field.



$$\begin{aligned}
 Re &= 600.0 \\
 \Omega &= 30.0 \text{ rad/sec} \\
 R_{\text{disk}} &= 0.10 \text{ m} \\
 h_o &= 0.07 \text{ m}
 \end{aligned}$$

Fig. 5.7. h. The history of evolution of the secondary flow field.



$$\begin{aligned}
 Re &= 400.0 \\
 \Omega &= 20.0 \text{ rad/sec} \\
 R_{disk} &= 0.10 \text{ m} \\
 h_o &= 0.07 \text{ m}
 \end{aligned}$$

Fig. 5.7. i . The history of evolution of the secondary flow field.

According to figure 5.7.a, the free surface interface exhibits a noticeable wavy behavior as the core wanders until it reaches a stationary mode of motion. As the liquid starts to repel towards the circumferential wall, the region in the vicinity of the free surface interface is not entirely influenced by the momentum generated by a rotating disk which makes the interface susceptible to oscillations. For instance, the first row of the vector plots in the same figure, namely, $t = 0.1$ sec, $t = 0.2$ sec, $t = 0.3$ sec shows the completion of a cycle of the wave propagating in radial-azimuthal direction which changes its modes of oscillation as it progresses to a consecutive cycle, $t = 0.4$ sec, $t = 0.5$ sec, etc. As time evolves, the free surface interface approaches the profile of the free surface predicted theoretically and experimentally with minor oscillations propagating upwards along the interface.

The wave propagation on the free surface interface constantly accompanies the computational flow domain which is also evident from other velocity-vector plots on the same figure. Under certain conditions there is a continuous small precession of the vortex core even at the steady-state condition which can be clearly seen from fig. 5.7.(c - e). A similar phenomenon of the core behavior was also observed experimentally. As the angular velocity of the rotating disk increases, the presence of precession is becoming less evident which once again reveals the fact that viscous-dissipation forces attenuate the oscillation. One does not observe a significant qualitative difference among the secondary flow patterns of two different values of viscosity. However, the transient period is quite diverse among these two sets of different viscosities. Considering the set of lower viscosity, the viscous-dissipation forces are not as strong as the other case which gives rise to a substantially profound oscillation especially in a neighborhood of the

free surface interface. In fact, the rate of viscous-diffusion which propagates upwards due to the rotation of a disk as time progresses, is different for the two cases. As a result of the low diffusivity, the numerical code is becoming prone to convective, as well as numerical instabilities.

The velocity-vector plots in the azimuthal-radial plane are quite spectacular (fig. 5.8). The results show intense wave activity taking place in the vortex core similar to that obtained experimentally by Vatistas (1990). The core develops distinct n-polygon shapes apex of which remain unperturbed at the center of rotation as the disk is continuously spinned by the external source. The results were obtained under a single set of prevailing conditions excluding the angular speed of a disk which was set to eight different values according to the figure.

Similar to the velocity-vector plots obtained in the radial-axial planes, the velocity-vector plots in the azimuthal-radial plane were generated by the same numerical settings. As the real time progressed, the free surface interface descended along the line of rotation, reaching the surface of a rotating disk and eventually forming the n-polygon shapes. According to the figure, the evolution of core shapes show similar functional dependence of the angular speed and the equilibrium states with the observations to that obtained experimentally between the angular speed and the equilibrium states which signifies the strong validity of the code. this proves that the waves in the core are indeed present in the solution of the Navier-Stokes equations.

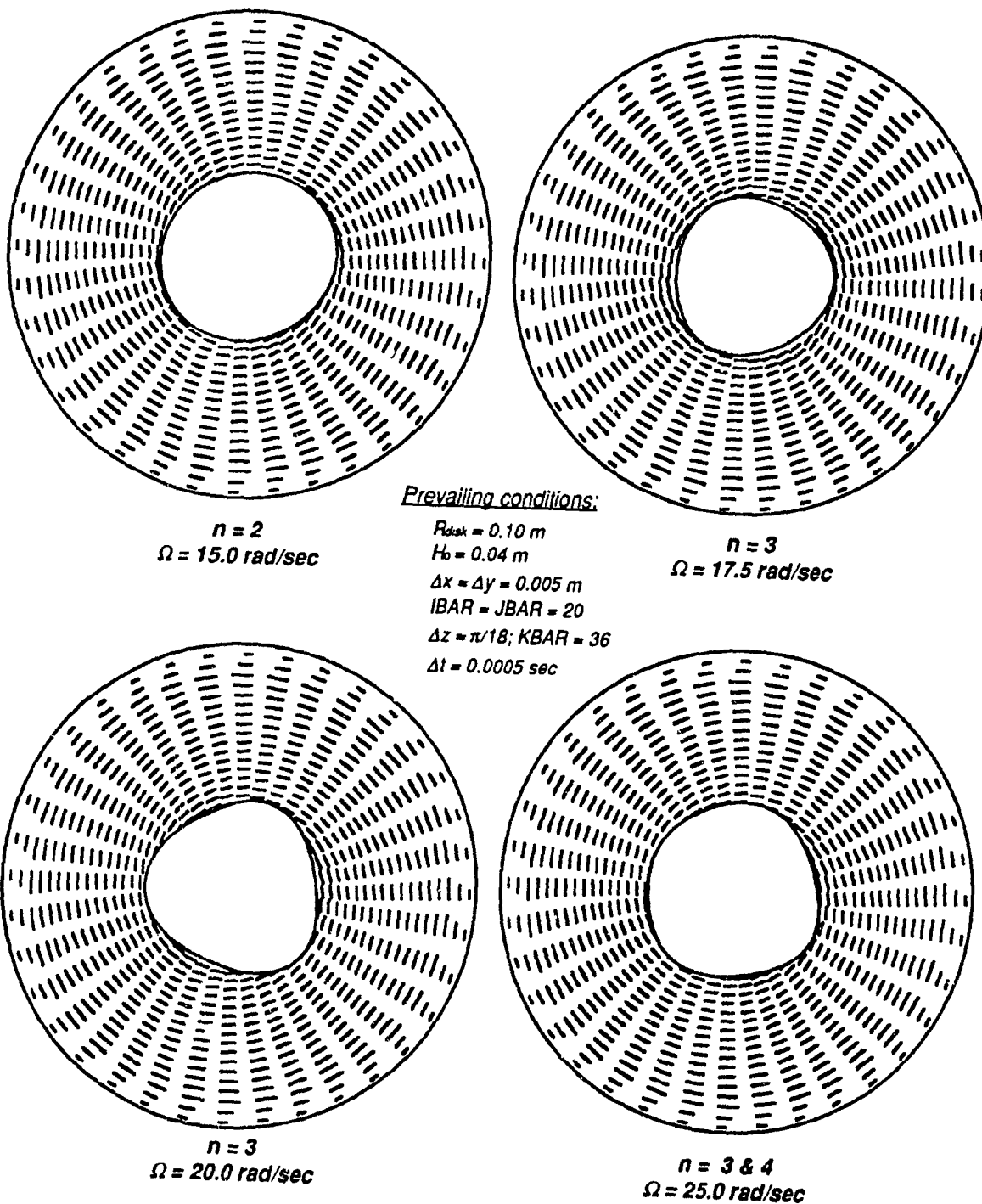
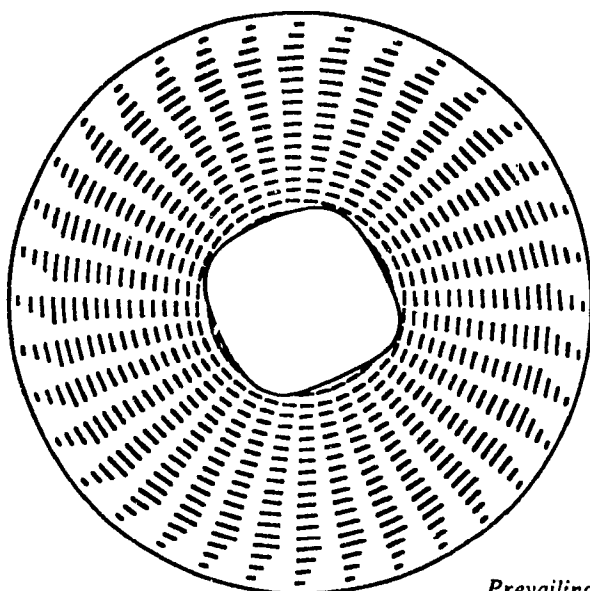
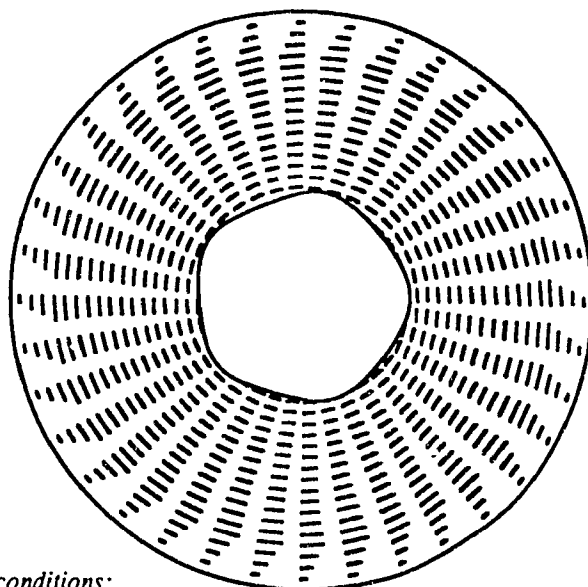


Fig. 5.8. a. The equilibrium states.



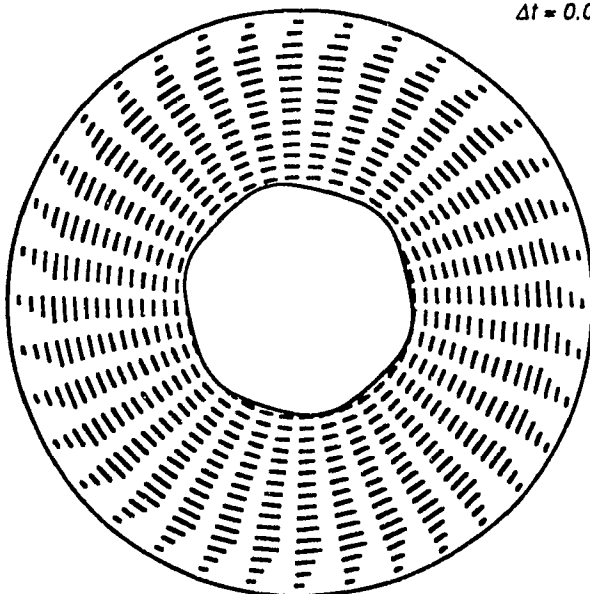
$n = 4$
 $\Omega = 27.5 \text{ rad/sec}$



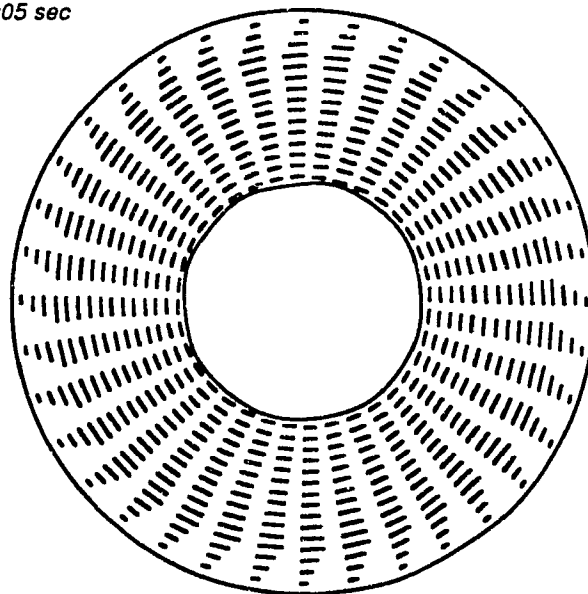
$n = 5$
 $\Omega = 30.0 \text{ rad/sec}$

Prevailing conditions:

$R_{\text{disk}} = 0.10 \text{ m}$
 $H_0 = 0.04 \text{ m}$
 $\Delta x = \Delta y = 0.005 \text{ m}$
 $IBAR = JBAR = 20$
 $\Delta z = \pi/18$; $KBAR = 36$
 $\Delta t = 0.0005 \text{ sec}$



$n = 6$
 $\Omega = 35.0 \text{ rad/sec}$



$n = 8$
 $\Omega = 38.5 \text{ rad/sec}$

Fig. 5.8. b. The equilibrium states.

6. Conclusions

The main objectives of conducting the present work were: (i) to develop a simple model capable of describing the primary parameters in concentrated columnar vortices, (ii) to use the new approach along with experimentation in the study of liquid agitation, (iii) to employ the model in other applications where the vortex is the dominant mechanism, and (iv) to develop a numerical solution technique with the aim to (a) characterize the secondary-like flow, (b) to prove that the observed harmonic disturbances in vortex cores are also present in the solution of Navier-Stokes equations.

The experimental and theoretical studies were successful in numbers of areas. The new empirical formula for a vortex greatly simplifies the derivation of pressure distribution and free surface profile. Dimensionless groups in liquid agitation were established and appropriate relationships between the main physical and geometrical parameters were attained. The application of the new realistic formula for the azimuthal velocity component simplifies substantially the main parameter characterization of vortex chamber flows and particle concentrations in liquid vortices.

The Los Alamos numerical algorithm SOLA-VOF (2-dimensional scheme) was extended to 3-dimensional flow field with the presence of a free surface, in cylindrical coordinates, and the obtained numerical results confirmed the experimental observations. The latter made possible the

depiction of the flow structure in the axial-radial plane. The presence of waves in the vortex core under prevailing conditions, found experimentally, were shown to exist in the solution on the equations of motion. Further studies using the code will enable one to construct the solution manifold of the problem under consideration which is vital in the understanding of the early stages of flow evolution towards turbulence.

References

- Abramovitz, M. and Stegun, I. A. *Handbook of Mathematical Functions with Formulas, Graphes, and Mathematical Tables*, (American Elsevier, New York: 1965).
- Abramson, N.H. (Editor), 1966, *The Dynamics Behavior of Liquids in Moving Containers*, NASA SP-106.
- Basina, I. P., Tonkonogii, A. V. and Kukuev, B. N., 1974, *Motion of Burning Particles in Cyclone Chambers*, Thermal Engineering, Vol. 14, No.1, pp. 99-103.
- Batchelor, G. K., *An Introduction to Fluid Dynamics*, (Cambridge University Press, 1967).
- Bennett, T. J., 1988, *Vortex Coalescence and Decay*, Ph.D. Thesis, Washington State University, Department of Civil Engineering.
- Binnie, A.M. and Hookings, G.A., 1948, *Laboratory Experiments on Whirlpools*, Proc. R. Soc. London. Ser. A, Vol. 194, pp. 398-415.
- Blasius, H., 1908, *Grenzschichten in Flüssigkeiten mit kleiner Reibung*, Z. Math. u. Phys. 56, 1-37; Engl. transl. in NASA TM 1256
- Burgers, J. M. 1948, *A Mathematical Model Illustrating the Theory of Turbulence*, Adv. in App. Mech., Vol. 1 pp. 171-199.
- Courant, R., Isaacson, E. and Rees, M., 1952, *On the Solution of Nonlinear Hyperbolic Differential Equations by Finite Differences*, Comm. Pure & Appl. Math., Vol. V, 243-255.

Escudier, M. P., Bornstein, J. and Zehnder, N., 1980, *Observations and LDA Measurements of Confined Turbulent Vortex Flow*, J. Fluid Mech., Vol. 98, part 1, pp. 49-63.

Escudier, M. P., Bornstein, J. and Maxworthy, T., 1982, *The Dynamics of Confined Vortices*, Proc. R. Soc. Lond. A 382, pp. 335-360.

Faler, J. H. and Leibovich, S., 1977, *Disrupted States of Vortex Flow and Vortex Breakdown*, The Physics of Fluids, Vol. 20, No. 9, pp.1385-1400.

Falvey, H.T., 1971, *Draft Tube Surges. A Review of Present Knowledge and an Annotated Bibliography*. US Bur. Reclam. Rep. REC-ERC-71-42.

Green, H. G. and Desselberger, M., *Turbulent Mixing in Nonlinear Vortex Flows*, Proc. of 5th Intern. Symp. on Flow Vis. Aug. 21- 25, 1989, Prague, Czechoslovakia, pp. 969-975.

Greenspan, H. P., 1968, *The Theory of Rotating Fluids*, Cambridge University Press.

Gupta, A. K., Lilley, D. G. and Syred, N., *Swirl Flows*, (Abacus Press: Tunbridge Wells, 1984).

Hamel, G., 1916, *Spiralformige Bewegung Zäher Flüssigkeiten*, Jahresber d. Dt. Mathematiker-Vereinigung, 25, pp. 34-60.

Hiemenz, K., 1911, *Die Grenzschicht an einem in den gleichförmigen Flüssigkeitsstrom eingetauchten geraden Kreiszylinder*, Thesis Göttingen 1911; Dingl. Polytechn. J. 326, 321.

Hilsch, R., 1947, *Die Expansion von Gasen in Zentrifugalfeld als Kälteprozess*, Z. Naturforsch, Vol. 1, 1946, pp. 208-214, Transl., in Rev. Sci. Instrum., Vol. 18, pp. 108-113.

Hirt, C. W., 1968, *Heuristic Stability for Finite-Difference Equations*, J. Comp. Phys., Vol. 2, No.4, pp. 13-20.

- Hirt, C. W., Nichols, B. D. and Romero, N. C., 1975, *Sola - A Numerical Algorithm for Transient Fluid Flows*, Los Alamos Scientific Laboratory, Los Alamos, N. Mexico, Report LA-5852.
- Howarth, L., 1935, *On the Calculation of the Steady Flow in the Boundary Layer near the Surface of a Cylinder in a Stream*, ARC RM, p. 1632.
- Julien, P. Y., 1986, *Concentration very fine silts in steady vortex*, J. Hydr. Rec., Vol. 24, No. 4, pp. 255-264.
- Julien, P. Y., 1985, *Motion of Sediment Particles in a Rankine Combined Vortex*, Report CER84-85PYJ6, Colorado State University, Fort Collins, May 1985, p. 37.
- Kelvin, Lord 1880 Phil. Mag. (5), 10, 155; Papers 4, 152. (Reproduced by Gray, A., Matthews, G. B. & MacRobert, T. M., 1922, *Bessel functions*, p. 123 London: Macmillan).
- Kerrebrock, J.L. and Meghreblian, R.V., 1958, *An Analysis of Vortex Tubes for Combined Gas-Phase Fission Heating and Separation of the Fissionable Material*, Report CF-57-11-3, Oak Ridge National Laboratory.
- Knauss, J., (Editor), 1966, *Swirling Flow Problems at Intakes*, A.A. Balkema, Rotterdam, Netherlands.
- Lamb, H., 1945, *Hydrodynamics*, (Dover Publications: New-York, 1945) p. 472.
- Leibovich, S., 1984, *Vortex Stability and Breakdown: Survey and Extension*, AIAA Journal, Vol. 22, No. 9, pp. 1192-1206.
- Lewellen, W. S., 1971, *A Review of Confined Vortex Flows*, NASA Contractor Report (NASA CR-1772), pp. 144-147.
- Lugt, H. J., 1983, *Vortex Flow in Nature and Technology*, John Wiley & Sons, New York, pp. 3-28.

- Maxworthy, T., Hopfinger, E. J. and Redekopp, L. G., 1985, *Wave motion in Vortex Core*, J. Fluid Mech., Vol. 151, pp. 141-165.
- Maxworthy, T., 1988, *Wave on Vortex Core*, Fluid Dynamics. Res. 3, pp. 52-62
- Morton, B.R., 1966, *Geophysical Vortices*, Progress in Aeronautical Sciences, Pergamon Press, Vol. 7, pp. 145-194.
- Newman, B. G. 1959, *Flow in a Viscous Trailing Vortex*, Aeronautical Quarterly, 10, pp.149-162.
- Nichols, B. D. and Hirt, C. W., 1971, *Improved Free Surface Boundary Conditions for Numerical Incompressible-Flow Calculations*, J. Comp. Phys., Vol. 8, No.3, pp. 434-448.
- Nichols, B. D., Hirt, C. W. and Hotchkiss, R. S. 1985, *A Solution Algorithm for Transient Fluid Flow with Multiple Free Boundaries*, Los Alamos Scientific Laboratory, Los Alamos, N. Mexico, Report LA-8455. pp.16-19.
- Oseen, C. W., 1911, *Hydromechanic*, Ark. f. Math. Astron. och. Fys., 7, p. 82.
- Pritchard, W. G., 1970, *Solitary Waves in Rotating Fluids*, J. Fluid Mech., Vol. 42, Part 1, pp. 61 - 83.
- Ragsdale, R.G., 1988, *NASA Research on the Hydrodynamics of the Gaseous Vortex Reactor*, NASA TN D-288.
- Ranque, G., 1933, *Expériences sur la Détente Giratoire avec Productions Simultanées d'un Echappement d'Air Chaud et d'un Echappement d'Air Froid*, J. Phys. Radium, Vol. 4, pp. 1123-1158.
- Reydon, R. F. and Gauvin, W. H., 1981, *Theoretical and Experimental Studies of Confined Vortex Flows*, The Canadian Journal Chemical Engineering, Vol. 59, pp.14-23.

Robertson, J. M., *Hydrodynamics in Theory and Application*, (Prentice-Hall Inc.: Englewood Cliffs, N. J., 1965).

Roschke, E. J., 1966, *Experimental Investigation of a Confined, Jet-Driven Water Vortex*, JPL Rep. 32-982, NASA CR-78550.

Ross, D. H., 1964, *An Experimental Investigation of Turbulent Shear in Jet-Driven Vortex Chambers*, Aerospace Corp. atn-64(9227)-5.

Rott, N., 1958, *On the Viscous Core of a Line Vortex*, ZAMP, Vol. 9, Fasc. 1, pp. 73-81.

Rouse, H. and Ince, S., *History of Hydraulics*, (Dover Publications, Inc.: New York, 1957).

Schlichting, H., *Boundary Layer Theory*, (McGraw-Hill Book Company: New York, 1979).

Shakespeare, W. J. and Levy, E. K., 1980, *Pressure Drop in a Confined Vortex in High Flow Rate*, Annual Meeting of ASME, Chicago, Illinois.

Sullivan, R. D., 1959, *A Two-Celled Vortex Solution of the Navier-Stokes Equations*, J. Aero/Space Sci. Read Forum 26, No. 11, pp. 34-42.

Tanasawa, Y. and Nakamura, K., 1971, *On the Vortex Combustor as Applied to the Gas Turbine*, Paper JSME-15, presented at the Joint JSME/ASME Tokyo International Gas Turbine Conference and Products Show.

Ter Linden, A.J., 1953, *Cyclone Dust Collectors for Boilers*, Trans. ASME, Vol. 75, pp. 433-440.

Troyansky, Y. U. and Baluev, E. D., 1969, *The Aerodynamic Resistance and Efficiency of Cyclone Chamber*, Thermal Engineering vol. 16, pp. 45-50

Vatistas, G. H. 1984. *Theoretical and Experimental Studies on Confined Vortex Flows*, Ph.D. Thesis, Mechanical Engineering Department, Concordia University, Montreal, Canada.

Vatistas, G. H., Lin, S., and Kwok, C. K., 1986, *Theoretical and Experimental Studies on Vortex Chamber Flows*, AIAA J., Vol. 24, No.4, pp. 635-642.

Vatistas, G. H., Lam, C. and Lin, S., 1989, *A Similarity Relationship for Pressure Drop in Vortex Chambers*, AIAA vol. 67, pp. 540-544.

Vatistas, G. H., 1989, *Analysis of Fine Particle Concentrations in a Confined Vortex*, J. Hydr. Res., Vol. 27, No. 3, 1989, pp. 417 - 427.

Vatistas, G. H., Kozel, V. I. and Mih, W. C. 1991, *A Simpler Model for Concentrated Vortices*, J. Exp. Fluids., vol 11, pp. 73-76.

Vatistas, G. H., 1990, *A Note on Liquid Vortex Sloshing and Kelvin's Equilibria*, Vol. 217, J. Fluid Mech. pp. 241-248.

Vatistas, G. H., Wang, J. and Lin, S., 1991, *The Liquid Motion Produced by a Rotating Disk in a Cylindrical Container*, private communication.

Yuan, S. W., *Foundations of Fluid Mechanics*, (Prentice-Hall International, Inc.: London, 1967).

Appendices

Appendix A

Pressure and free surface profile derivations, (chapter 2)

$$\bar{P}(\bar{r}, \bar{z}) = \int \frac{\bar{V}_\theta^2}{\bar{r}} d\bar{r} - \eta \bar{z} + \text{constant} \quad (\text{A.1})$$

Rankine's model

For the forced-vortex region,

$$\bar{P}(\bar{r}, \bar{z}) = \frac{\bar{r}^2}{2} - \eta \bar{z} + C_1 \quad (\text{A.2})$$

At $\bar{r} = 0$, $\bar{P} = 0$ which leads to $C_1 = \eta \bar{z}_h$

Therefore,

$$\bar{P}(\bar{r}, \bar{z}) = \frac{\bar{r}^2}{2} - \eta(\bar{z} - \bar{z}_h) \quad (\text{A.3})$$

For the free-vortex region,

$$\bar{P}(\bar{r}, \bar{z}) = -\frac{1}{2\bar{r}^2} - \eta \bar{z} + C_2 \quad (\text{A.4})$$

At $\bar{r} = 1$, both pressures, eq. (A.3) and eq. (A.4) must be equal, or

$$-\frac{1}{2} - \eta \bar{z}_c + C_2 = \frac{1}{2} - \eta(\bar{z}_h - \bar{z}_c)$$

or

$$C_2 = 1 + \eta \bar{z}_h$$

Then eq. (A.4) becomes,

$$\bar{P}(\bar{r}, \bar{z}) = \left[1 - \frac{1}{2\bar{r}^2} \right] \cdot \eta(\bar{z} + \bar{z}_h) \quad (\text{A.5})$$

For a gaseous Rankine's vortex, $\eta \approx 0$, eq. (A.3) and eq. (A.5) become respectively,

$$\bar{P}(\bar{r}, \bar{z}) = \frac{\bar{r}^2}{2} \quad (\text{A.6})$$

and

$$\bar{P}(\bar{r}, \bar{z}) = \left[1 - \frac{1}{2\bar{r}^2} \right] \quad (\text{A.7})$$

From eq. (A.7),

$$\bar{P}(\bar{r} \rightarrow \infty, \bar{z}) = 1 \quad (\text{A.8})$$

Dividing both eq. (A.6) and eq. (A.7) by eq. (A.8), one obtains:

$$\overline{\Delta P} = \frac{P - P_h}{P_\infty - P_h} = \frac{\bar{r}^2}{2} \quad (\text{A.9})$$

and

$$\overline{\Delta P} = \frac{P - P_h}{P_\infty - P_h} = 1 - \frac{1}{2\bar{r}^2} \quad (\text{A.10})$$

respectively.

To obtain the profile of free liquid surface we set $\bar{P}(\bar{r}, \bar{z}) = 0$. Then, eq. (A.3) and eq. (A.4) can be expressed as

$$\bar{z} - \bar{z}_h = \eta \frac{\bar{r}^2}{2} \quad (\text{A.11})$$

and

$$\bar{z} - \bar{z}_h = \frac{1}{\eta} \left[1 - \frac{1}{2\bar{r}^2} \right] \quad (\text{A.12})$$

respectively. From eq. (A.12)

$$\bar{z}_\infty - \bar{z}_h = \frac{1}{\eta} \quad (\text{A.13})$$

Dividing both eq (A.11) and eq. (A.12) by eq. (A.13)

$$\overline{\Delta P} = \frac{z - z_h}{z_\infty - z_h} = \frac{\bar{r}^2}{2} \quad (\text{A.14})$$

and

$$\overline{\Delta P} = \frac{z - z_h}{z_\infty - z_h} = \left[1 - \frac{1}{2\bar{r}^2} \right] \quad (\text{A.15})$$

for the forced and free vortices respectively.

Burgers' model

Using Burgers' vortex, eq. (A.1) yields,

$$\bar{P}(\bar{r}, \bar{z}) = \beta - \eta \bar{z} + \text{constant}$$

where β is given in the main text. In the case of a gaseous vortex,

$$\bar{P}(\bar{r}, \bar{z}) = \beta + \text{constant}$$

The limiting case gives $\bar{P}(\bar{r} \rightarrow 0) = \lim_{\bar{r} \rightarrow 0} \beta + \text{const.} = 0$

Then $\text{const.} = - \lim_{\bar{r} \rightarrow 0} \beta$

Also,

$$\frac{P - P_h}{P_\infty - P_h} = 1 - \frac{\beta}{\lim_{\bar{r} \rightarrow 0} \beta}$$

But

$$\lim_{\bar{r} \rightarrow 0} \beta = \alpha \lim_{\bar{r} \rightarrow 0} [\text{Ei}(-\alpha \bar{r}^2) - \text{Ei}(-2\alpha \bar{r}^2)]$$

By definition, Abramowitch et al (1970)

$$\text{Ei}(-u) = \gamma + \ln(u) - \sum_{n=1}^{\infty} \frac{(-1)^{n+1}}{n n!} u^n$$

where γ is Euler's constant ($\gamma \approx 0.5772157$)

Then,

$$\lim_{\bar{r} \rightarrow 0} \beta = \alpha \ln(2) \sum_{n=1}^{\infty} \frac{(-1)^{n+1}}{n n!} n \bar{r}^{2n} (2^n - 1) = \alpha \ln(2)$$

Therefore,

$$\frac{P - P_h}{P_\infty - P_h} = 1 - \frac{\beta}{\alpha \ln(2)} \quad (\text{A.16})$$

For the liquid free surface

$$\bar{z} = \frac{\beta}{\eta} + \text{constant}$$

and

$$\bar{z}_o @ \bar{r} \rightarrow 0 = \frac{\alpha \ln(2)}{\eta} + \text{constant}$$

$$\text{constant} = \bar{z}_h - \frac{\alpha \ln(2)}{\eta}$$

then

$$\bar{z} - \bar{z}_h = \frac{\beta}{\eta} - \frac{\alpha \ln(2)}{\eta}$$

$$\bar{z}_\infty - \bar{z}_h = -\alpha \ln(2)$$

Therefore,

$$\overline{\Delta P} = \frac{z - z_h}{z_\infty - z_h} = 1 - \frac{\beta}{\alpha \ln(2)} \quad (\text{A.17})$$

New model

Using velocity for the new vortex, eq. (A.1) yields,

$$\bar{P}(\bar{r}, \bar{z}) = \frac{1}{2} \arctan(\bar{r}^2) - \eta \bar{z} + \text{constant}$$

At $\bar{r} = 0$, $\bar{P} = 0$, which leads to $C_1 = \eta \bar{z}_h$.

Then the pressure equation becomes,

$$\bar{P}(\bar{r}, \bar{z}) = \frac{1}{2} \arctan(\bar{r}^2) - \eta(\bar{z} - \bar{z}_h) \quad (\text{A.18})$$

For a gaseous vortex, $\eta \approx 0$, eq. (A.18) becomes,

$$\bar{P}(\bar{r}) = \frac{1}{2} \arctan(\bar{r}^2) \quad (\text{A.19})$$

Division of eq. (A.19) by $\bar{P}(\bar{r} \rightarrow \infty)$ yields,

$$\overline{\Delta P} = \frac{P - P_h}{P_\infty - P_h} = \frac{\frac{1}{2} \arctan(\bar{r}^2)}{\left(\frac{2\pi R_0^2}{\Gamma_\infty}\right)^2 \frac{P_\infty - P_h}{\rho}}$$

However,

$$\lim_{\bar{r} \rightarrow \infty} \overline{\Delta P} = 1$$

Then

$$\left(\frac{2\pi R_0^2}{\Gamma_\infty}\right)^2 \frac{P_\infty - P_h}{\rho} \rightarrow \frac{\pi}{4} \quad (\text{A.20})$$

Then,

$$\overline{\Delta P} = \frac{2}{\pi} \arctan(\bar{r}^2) \quad (\text{A.21})$$

To obtain the profile of free liquid surface we set $\bar{P}(\bar{r}, \bar{z}) = 0$. Then, eq. (A.18) gives,

$$\bar{z} - \bar{z}_h = \frac{1}{2\eta} \arctan(\bar{r}^2) \quad (\text{A.22})$$

From eq. (A.22)

$$\bar{z}_\infty - \bar{z}_h = \frac{\pi}{4\eta} \quad (\text{A.23})$$

Division of both eq (A.22) by eq. (A.23) yields,

$$\overline{\Delta P} = \frac{2}{\pi} \arctan(\bar{r}^2) \quad (\text{A.14})$$

and

$$\overline{\Delta P} = \frac{z - z_h}{z_\infty - z_h} = \left[1 - \frac{1}{2\bar{r}^2} \right] \quad (\text{A.15})$$

Appendix B

Derivation of Equations (4.4) and (4.5)

The energy balance across the vortex chamber

$$\int_{A_{out}} \left(P + \frac{1}{2} \rho q^2 \right) V_z dA = \int_{A_{in}} \left(P + \frac{1}{2} \rho q^2 \right) \vec{q} \cdot \vec{n} dA \quad (B.1)$$

Let

$$V_z = \frac{Q}{\pi (R_e^2 - R_o^2)} \quad (B.2)$$

then,

$$P_{in} - P_a = \frac{1}{Q} \int_{R_o}^{R_e} \rho \pi q^2 V_z r dr - \frac{1}{2} \rho q_{in}^2 \quad (B.3)$$

substituting eq. (B.2) into eq. (B.3) yields

$$P_{in} - P_a = \frac{\rho}{(R_e^2 - R_o^2)} \int_{R_o}^{R_e} (V_\theta^2 - V_z^2) r dr - \frac{1}{2} \rho q_{in}^2 \quad (B.4)$$

Also, from eq. (2.23)

$$V_\theta^2 = \left(\frac{\Gamma_\infty}{2\pi} \right)^2 \frac{r^2}{R_o^4 + r^4} \quad (B.5)$$

Substituting eq. (B.5) into eq. (B.4) results

$$P_{in} - P_{out} = P_{in} - P_a = \frac{\rho}{R_e^2 - R_o^2} \int_{R_o}^{R_e} \left(\frac{\Gamma_\infty}{2\pi} \right)^2 \frac{r^3}{R_o^4 + r^4} dr + \frac{\rho V_z^2}{R_e^2 - R_o^2} \int_{R_o}^{R_e} r dr - \frac{\rho}{2} q_{in}^2 \quad (B.6)$$

$$\int_{R_o}^{R_e} \frac{r^3}{R_o^4 - r^4} dr = \frac{1}{4} \ln \left(\frac{1}{2} \left(1 + \frac{1}{x_c^4} \right) \right) \quad (B.7)$$

then,

$$\Delta P = P_{in} - P_{out} = \frac{\rho}{(R_e^2 - R_o^2)} \left(\frac{\Gamma_\infty}{2\pi} \right)^2 \frac{1}{4} \ln \left(\frac{1}{2} \left(1 + \frac{1}{x_c^4} \right) \right) + \frac{\rho V_z^2}{2} - \frac{\rho}{2} q_{in}^2 \quad (B.8)$$

Rearranging the terms

$$\frac{2\Delta P}{\rho q_{in}^2} + 1 = \frac{1}{2(R_e^2 - R_o^2)} \left(\frac{\Gamma_\infty}{2\pi} \right)^2 \frac{1}{q_{in}^2} \ln \left(\frac{1}{2} \left(1 + \frac{1}{x_c^4} \right) \right) + \frac{V_z^2}{q_{in}^2} \quad (B.9)$$

Also,

$$\left(\frac{\Gamma_\infty}{2\pi R_t^2} \right)^2 \frac{R_t^2}{q_{in}^2} = \frac{V_z^2}{q_{in}^2} R_t^2 = R_t^2 \cos^2 \theta \quad (B.10)$$

with an addition of the eq. (B.10), eq. (B.9) retains the form:

$$\frac{2\Delta P}{\rho q_{in}^2} + 1 = \frac{R_t^2 \cos^2 \theta}{2(R_e^2 - R_o^2)} \ln \left(\frac{1}{2} \left(1 + \frac{1}{x_c^4} \right) \right) + \frac{Q^2}{\pi^2 (R_e^2 - R_o^2)^2 q_{in}^2} \quad (B.11)$$

or

$$\frac{2\Delta P}{\rho q_{in}^2} + 1 = \left(\frac{R_t^2}{R_o^2} \right)^2 \frac{\cos^2 \theta}{2(1 - x_c^2)} \ln \left(\frac{1}{2} \left(1 + \frac{1}{x_c^4} \right) \right) + \frac{(A_{in} q_{in})^2}{\pi^2 R_e^4 (1 - x_c^2)^2 q_{in}^2} \quad (B.12)$$

and

$$\Delta \tilde{P} = \frac{\beta}{(1 - x_c^2)^2} + \frac{\ln \left(\frac{1}{2} (x_c^4 + 1) / x_c^4 \right)}{2(1 - x_c^2)} \quad (B.13)$$

where,

$$\Delta \tilde{P} = \left(\frac{2(P_{in} - P_a)}{\rho q_{in}^2} + 1 \right) \left(\frac{R_e/R_t}{\cos \theta} \right)^2$$

$$\beta = \left(\frac{A_{in}/A_t}{R_e/R_t \cos \theta} \right)^2$$

Introducing

$$\frac{\partial \Delta \tilde{P}}{\partial x_c} = 0;$$

which yields,

$$\frac{2x_c}{(1-x_c^2)^2} \left\{ \ln \sqrt{\frac{1}{2} \left(1 + \frac{1}{x_c^4} \right)} + \frac{\beta}{1-x_c^2} \right\} + \frac{1}{(1-x_c^2)} \left\{ \frac{1}{2} \frac{(-x_c^5)}{\left(1 + \frac{1}{x_c^4} \right)} + \frac{2\beta x_c}{(1-x_c^2)^2} \right\} = 0 \quad (B.14)$$

or

$$\frac{2x_c}{(1-x_c^2)^2} \left\{ \ln \sqrt{\frac{1}{2} \left(1 + \frac{1}{x_c^4} \right)} + \frac{2\beta}{1-x_c^2} - \frac{(1-x_c^2)}{x_c^2(1+x_c^4)} \right\} = 0 \quad (B.15)$$

and, finally,

$$2\beta - \frac{(1-x_c^2)^2}{2x_c^2(1+x_c^4)} - (1-x_c^2) \ln \sqrt{\frac{1}{2} \left(1 + \frac{1}{x_c^4} \right)} = 0 \quad (B.16)$$

Appendix C

Discretized Equations.

x - momentum

$$U \frac{\partial U}{\partial x} \sim FUX = \frac{1}{2\Delta x} U_{i,j,k} \left((U_{i+1,j,k} - U_{i-1,j,k}) + \alpha |U_{i,j,k}| (2U_{i,j,k} - U_{i+1,j,k} - U_{i-1,j,k}) \right)$$

$$V \frac{\partial U}{\partial y} \sim FUY = \frac{1}{2\Delta y} \left(\frac{V_{i+1,j,k} + V_{i,j,k} + V_{i+1,j-1,k} + V_{i,j-1,k}}{4} \right) \left((U_{i,j+1,k} - U_{i,j-1,k}) + \right. \\ \left. + \alpha |V^*| (2U_{i,j,k} - U_{i,j+1,k} - U_{i,j-1,k}) \right)$$

$$\frac{W}{x} \frac{\partial U}{\partial z} \sim FUZ = \frac{1}{2x\Delta z} \left(\frac{W_{i+1,j,k} + W_{i,j,k} + W_{i+1,j,k-1} + W_{i,j,k-1}}{4} \right) \left((U_{i,j,k+1} - U_{i,j,k-1}) + \right. \\ \left. + \alpha |W^*| (2U_{i,j,k} - U_{i,j,k+1} - U_{i,j,k-1}) \right)$$

$$\frac{W^2}{x} \sim FUC = \frac{1}{4x} U_{i,j,k} \left\{ (U_{i+1,j,k} + U_{i-1,j,k} + 2U_{i,j,k}) - \alpha |U_{i,j,k}| (U_{i+1,j,k} - U_{i-1,j,k}) \right\}$$

$$VISCX = \frac{1}{\Delta x^2} (U_{i+1,j,k} + U_{i-1,j,k} - 2U_{i,j,k}) + \frac{1}{2x\Delta x} (U_{i+1,j,k} - U_{i-1,j,k}) + \\ + \frac{1}{\Delta y^2} (U_{i,j+1,k} + U_{i,j-1,k} - 2U_{i,j,k}) + \frac{1}{(x\Delta z)^2} (U_{i,j,k+1} + U_{i,j,k-1} - 2U_{i,j,k}) - \\ - \frac{U_{i,j,k}}{x^2} - \frac{1}{x^2\Delta z} (W_{i,j,k} + W_{i+1,j,k} - W_{i,j,k-1} - W_{i+1,j,k-1})$$

$$U_{i,j,k}^{n+1} = U_{i,j,k}^n + \Delta t \left(\frac{1}{\Delta x} (P_{i-1,j,k} - P_{i,j,k}) - FUX - FUY - FUZ + FUC + v^* VISCX \right)^n$$

where

$$V^* = (V_{i+1,j,k} + V_{i,j,k} + V_{i+1,j-1,k} + V_{i,j-1,k}) / 4$$

$$W^* = W_{i+1,j,k} + W_{i,j,k} (+ W_{i+1,j,k-1} + W_{i,j,k-1}) / 4$$

y - momentum

$$U \frac{\partial V}{\partial x} \sim FVX = \frac{1}{2\Delta x} \left(\frac{U_{i,j,k} + U_{i,j+1,k} + U_{i-1,j,k} + U_{i-1,j+1,k}}{4} \right) \{ (V_{i+1,j,k} - V_{i-1,j,k}) + \\ + \alpha |U^*| (2V_{i,j,k} - V_{i+1,j,k} - V_{i-1,j,k}) \}$$

$$V \frac{\partial V}{\partial y} \sim FVY = \frac{1}{2\Delta y} V_{i,j,k} \{ (V_{i,j+1,k} - V_{i,j-1,k}) + \alpha |V_{i,j,k}| (2V_{i,j,k} - V_{i,j+1,k} - V_{i,j-1,k}) \}$$

$$\frac{W}{x} \frac{\partial V}{\partial z} \sim FUZ = \frac{1}{2x\Delta z} \left(\frac{W_{i+1,j,k} + W_{i,j,k} + W_{i+1,j,k-1} + W_{i,j,k-1}}{4} \right) \{ (V_{i,j,k+1} - V_{i,j,k-1}) + \\ + \alpha |W^*| (2V_{i,j,k} - V_{i,j,k+1} - V_{i,j,k-1}) \}$$

$$VISCX = \frac{1}{\Delta x^2} (V_{i+1,j,k} + V_{i-1,j,k} - 2V_{i,j,k}) + \frac{1}{2x\Delta x} (V_{i+1,j,k} - V_{i-1,j,k}) + \\ + \frac{1}{\Delta y^2} (V_{i,j+1,k} + V_{i,j-1,k} - 2V_{i,j,k}) + \frac{1}{(x\Delta z)^2} (V_{i,j,k+1} + V_{i,j,k-1} - 2V_{i,j,k}) -$$

$$V_{i,j,k}^{n+1} = V_{i,j,k}^n + \Delta t \left(\frac{1}{\Delta y} (P_{i,j-1,k} - P_{i,j,k}) - FVX - FVY - FVZ + v^* VISCY \right)^n$$

where

$$U^* = (U_{i,j,k} + U_{i,j+1,k} + U_{i-1,j,k} + U_{i-1,j+1,k}) / 4$$

$$W^* = (W_{i+1,j,k} + W_{i,j,k} + W_{i+1,j,k-1} + W_{i,j,k-1}) / 4$$

z - momentum

$$U \frac{\partial W}{\partial x} \sim FVX = \frac{1}{2\Delta x} \left(\frac{U_{i,j,k} + U_{i,j,k+1} + U_{i-1,j,k} + U_{i-1,j,k+1}}{4} \right) \{ (W_{i+1,j,k} - W_{i-1,j,k}) + \\ + \alpha |U^*| (2W_{i,j,k} - W_{i+1,j,k} - W_{i-1,j,k}) \}$$

$$V \frac{\partial W}{\partial y} \sim FUY = \frac{1}{2\Delta y} \left(\frac{V_{i,j,k+1} + V_{i,j,k} + V_{i,j-1,k+1} + V_{i,j-1,k}}{4} \right) \{ (W_{i,j+1,k} - W_{i,j-1,k}) + \\ + \alpha |V^*| (2W_{i,j,k} - W_{i,j+1,k} - W_{i,j-1,k}) \}$$

$$\frac{W}{x} \frac{\partial W}{\partial y} \sim FVY = \frac{1}{2x\Delta z} W_{i,j,k} \{ (W_{i,j,k+1} - W_{i,j,k-1}) + \\ + \alpha |W_{i,j,k}| (2W_{i,j,k} - W_{i,j,k+1} - W_{i,j,k-1}) \}$$

$$\frac{UW}{x} \sim FVX = \frac{1}{x} \left(\frac{U_{i,j,k} + U_{i,j,k+1} + U_{i-1,j,k} + U_{i-1,j,k+1}}{4} \right) \{ (W_{i+1,j,k} - W_{i-1,j,k}) + \\ + \alpha |U^*| (W_{i+1,j,k} - W_{i-1,j,k}) \}$$

$$VISCZ = \frac{1}{\Delta x^2} (W_{i+1,j,k} + W_{i-1,j,k} - 2W_{i,j,k}) + \frac{1}{2x\Delta x} (W_{i+1,j,k} - W_{i-1,j,k}) +$$

$$+ \frac{1}{\Delta y^2} (W_{i,j+1,k} + W_{i,j-1,k} - 2W_{i,j,k}) + \frac{1}{(x\Delta z)^2} (W_{i,j,k+1} + W_{i,j,k-1} - 2W_{i,j,k}) -$$

$$\frac{W_{i,j,k}}{x^2} + \frac{U_{i-1,j,k+1} + U_{i,j,k+1} - U_{i-1,j,k} - U_{i,j,k}}{x^2\Delta z}$$

$$W_{i,j,k}^{n+1} = W_{i,j,k}^n + \Delta t \left(\frac{1}{x\Delta z} (P_{i,j,k-1} - P_{i,j,k}) - FWX - FWY - FWZ - FWC + v^* VISCZ \right)^n$$

where

$$U^* = (U_{i,j,k} + U_{i,j,k+1} + U_{i-1,j,k} + U_{i-1,j,k+1}) / 4$$

$$V^* = (V_{i,j,k+1} + V_{i,j,k} + V_{i,j-1,k+1} + V_{i,j-1,k}) / 4$$